Modeling R8 Specification in the *Drosophila* Eye, from Genes to Tissue

by

Matthew W. Pennington

A dissertation submitted in partial fulfillment
of the requirements for the degree of
Doctor of Philosophy
(Biophysics)
in The University of Michigan
2009

Doctoral Committee:

Assistant Professor David K. Lubensky, Chair
Associate Professor Jorge A. Iñiguez-Lluhí
Associate Professor Nils G. Walter
Associate Professor Michal R. Zochowski

“Even if I set out to make a film about fillet of sole, it would be about me.”
–Frederico Fellini

To Katy

Acknowledgements

This is lengthy, but these things need to be said.

I would like to thank my family, my advisor, and my committee.

My mom, dad, Keith, and Katy, have been more supportive than anyone really should be called upon to be. I'll just leave that be. They know.

David Lubensky, my advisor, found me as a second-hand grad student with two years banked and lost, and a background most people don't think exists. He took a risk on me within weeks of arriving at the university, and for that I am incredibly grateful. That he turned out to be a fantastic scientist working on the sort of problem (developmental systems biology) I'd always wanted to study, but could never find place for, before? That's like frosting, and not the Kroger sugar-and-shortening kind, but the Cake Nouveau butter-cream kind. Things have a way of working out. In this same category, I should thank our collaborator, Nick Baker, and his entire lab for providing ideas, perspective, reality checks, and cold, hard data. Truly, we would be nothing without them.

My committee has been with me since the beginning, and they have been incredibly supportive. They know this, I think, so I will just say, again, that I appreciate it. Thank you.

I would like to thank my department, my school, and my program.

The biophysics department has been very accommodating of my, umm, special needs, and that has made things possible.

The medical school… honestly, how do they do it? If you ever want to feel well-treated by an administrative entity, go to medical school.

The University of Michigan Medical Scientist Training Program is, of course, wrapped up with my life in a very big way. I would especially like to thank Penny Morris, who set the tone for at least seven years of my life, helped my wife find a doctor, made me think I could do this in the first place, and on and on. Of course, Ron Koenig, Ellen Elkin, Hilkka Ketola, and Laurie Koivupalo: All would be chaos without you, thanks.

I would like to thank some programs.

Anyone who knows me knows that I have, in general, been at my best right after attending particularly good workshops. The first of these was the Boulder Condensed Matter Summer School, which broadened my horizons immensely.

The I2CAM workshop in Cargese, in 2006 was my first (tantalizing) taste of real, modern systems biology, and it was taught by the best. Special thanks to Uri Alon and Robyn Bruinsma for being two of the best teachers I've ever had.

The Center for Theoretical Biophysics at UCSD hosted a concise and helpful workshop on applied methods in cellular modeling, and I learned many good lessons.

Most significantly (honestly, chapters III and IV of this thesis would never have occurred, otherwise), I would like to thank the Santa Fe Institute for accepting me to their Beijing Complex Systems Summer School in 2008. Dave Feldman, Will Tracy, Henry

Wright, Chris Wiggins, Lee Altenberg, Jon Wilkins, Hao Bai-Lin, Eric Smith, Dan Hruschka, and Miguel Fuentes: The only word is “inspiring.”

I would like to thank a lot of other people.

Starting from the beginning.

Seth Blumberg, Ari Gajraj, Raj Nambiar, Hao Chen, Kat Jordan, Gerhard Blab, and Chaim Schramm: You guys are awesome. Dave Wilson, in particular, thanks for showing me that I, too, could be a theorist.

Alice Lam, Ziba Scott, Andrea Baines, Brandon McKinney, Ben Singer, and Durga Singer: Thanks for being there, beginning to end. Not many people understand our scene, and complaining can be healthy, right?

Sorin Tanase-Nicola and Guillaume Salbreux: Thanks for doubling the population of the Lubensky “Lab.”

Mike Murrell, Lolo Jawerth, Aidan Craig, Jeetain Mittal, Lisa Manning, Aphrodite and Mohammed Ahmadi, Jacy Bird, Rupert Nash, Mark Elsesser, Liz Janus and, especially, Karen Kasza: Wow, finding you guys was an incredible piece of luck.

Gillian Ryan, Natsuki Tanaka, and Sarah Nowak, Tak Sing, and “Alex” Sen Xu: You’d have gotten along well with the previous bunch.

Eva-Maria (who must have a last name!), thanks for pretending my APS talk went well.

Casey Scheider-Mizell, Sarah Feldt, Jack Waddell, Ross O’Connell, Andrew Eppig, Brooks Thomas, Kate Anderson, Matt Largo, Sarah Nuss-Warren, Chris Nakamura, Elizabeth Leicht, Gourab Ghoshal, Matt Zimmerman, Olivia Wooley, and

Alana Kirby: This is so much better with other people in roughly the same boat. You have all gotten me unstuck at least once, and that doesn't count all the fun and good taste.

Adam Brown, Arun Gopal, Steve Soldan, Trevor Peterson, Julia Snyder, Neil Frakes, and Deepak Kulkarni: We will probably do this forever.

Linda Doan: Thank you for a thousand little things.

Mien Chyi: You come and go, but are always very convincing.

Matt Scott: The hobby you convinced me to start has kept me sane.

Lily Young, and Michelle Eng: You have impeccable senses of timing.

Jason DeVita and Soo Lee: Team Becchetti still owns this place.

Table of Contents

Dedication ii

Acknowledgements iii

List of Figures ix

List of Appendices xii

Abstract xiii

Chapter

I. Introduction 1

Organization and Multiscale Approach 1

The Drosophila Eye 4

Modeling Biological Pattern Formation 15

II. Propagating-Patterning Fronts in 1D Discrete Media 33

The Model 36

Cell Autonomous Behavior 38

Propagating Solutions 44

Parameter Scan 57

Analyzing Patterns 61

Results 62

Discussion 75

III. The Activation of Nearly Equivalent Cells, and the Resolution of Proneural Clusters 79

Eye Context 79

Approach....83
Individual Cells....84
Two-Cell System....90
Multiple Cells....101
Parameter Dependence....105
Results....107
Specific Predictions....118
IV. Long Range Patterning....129
Order in the Eye Disc....130
Concept and Method....140
Examples....158
Specific Applications....163
V. Conclusion....169
Appendices....172
Bibliography....194

List of Figures

Figure 1: Adult *Drosophila* eye, scanning electron micrograph..... 5

Figure 2: A third-instar eye disc with Senseless stained..... 7

Figure 3: Simulation compared to eye disc patterning. 10

Figure 4: Stripes in simulation and eye disc. 11

Figure 5: Regulation Network Diagram. 14

Figure 6: Turing instability in a 2-component reaction diffusion system..... 20

Figure 7: Fourier transform of the linear nearest neighbor diffusion operator. 23

Figure 8: Clock-and-wavefront patterning..... 29

Figure 9: Examples of computed results..... 35

Figure 10: Single cell stability and dynamics. 41

Figure 11: 1D map relating *u* at a newly patterned point immediately after its activation to the amount of *u* at the previous activated point. 52

Figure 12: A detail of a higher-period solution to the pattern template solution..... 53

Figure 13: Observed versus predicted periodicity for parameter sets showing regular 1-up-integer-down patterns. 66

Figure 14: Null model for period prediction. 67

Figure 15: Timescale separation and patterning v. non-patterning behavior..... 70

Figure 16: Timescale separation and complicated patterning behavior..... 71

Figure 17: Quantitative comparison of observed versus predicted front velocity. 74

Figure 18: A theoretical bifurcation diagram for propagation and pattern formation with a parameter controlling the relative timescales of cell-autonomous dynamics and front propagation as bifurcation parameter..... 78

Figure 19: Schematic and image of wildtype MF stained for Atonal (green) and Dachshund (magenta). 82

Figure 20: Nullclines and trajectories for different values of *h* and *u*. 87

Figure 21: Nullclines, trajectory, and separatrix for an isolated cell. 88

Figure 22: Nullclines and steady states for a two-cell system. 92

Figure 23: Bifurcation diagrams for two cells. 93

Figure 24: Schematic of the two-cell system. 96

Figure 25: Trajectories over time of two identical cells activated at very small delay. .. 99

Figure 26: Trajectories over time of two identical cells activated at larger delay. 100

Figure 27: A small grid showing naturally arising proneural clusters. 104

Figure 28: Correlation of empirical 2-cell critical Δt and those deduced from 1-cell simulations. 111

Figure 29: Predictions and observations of outcomes for a seven-cell cluster. 112

Figure 30: The results of a parameter scan of simulations done on 192-cell randomized epithelia at low front velocity. 115

Figure 31: The results of a parameter scan of simulations done on 192-cell randomized epithelia at higher front velocity. 116

Figure 32: The results of a parameter scan of simulations done on 192-cell randomized epithelia for a very fast front. 117

Figure 33: Summary of pattern v. stripe template analysis. 121

Figure 34: Nullclines for unstable symmetric high steady state in the 2-inhibitor model of equation (10). 125

Figure 35: Trajectories of a in seven cells incorporating a neurogenic clone. 128

Figure 36: A *hs-*N_{intra}*, sca-* eye disc with Notch intracellular domain driven by a heatshock promoter. 135

Figure 37: Ordering and null-model comparison for the eye disc in Figure 36. 137

Figure 38: A *sca-* eye-disc with temperature sensitive Notch that shows a clear pattern of stripes. 138

Figure 39: Ordering analysis of the eye disc in the Figure 38. 139

Figure 40: Coalescing a 1D patterning finite state machine. 143

Figure 41: Coalescence of the 2D patterning system, schematic. 146

Figure 42: Basic stripe errors. 148

Figure 43: Schematic of stripe classification. 149

Figure 44: Simulation and eye disc showing stripes capable of significant self-healing. 150

Figure 45: Small error states for hexagonal patterning. 154

Figure 46: The result of a state. 155

Figure 47: The state-state transition process. 156

Figure 48: Examples of templates used to explore transition space. 157

Figure 49: Rates of leaving the perfect stripe condition for simultaneously decreasing τ_u and increasing U_a.. 160

Figure 50: Intermediate error states generated by a sample pattering process. 162

Figure 51: Eye disc stained for Senseless with attention drawn to pattern errors near the edge. 166

Figure 52: Studying edge effects and MF asymmetry. 168

Figure 53: Average propagating *h* for reference parameters in the continuum with deviations produced by a periodic template 178

Figure 54: Illustration of the steps involved in making a simulated epithelium. 184

Figure 55: Different behaviors of the intermediate-*a* state. 190

Figure 56: Trajectories of stable-spiral and limit-cycle proneural states in the a-u plane. 191

List of Appendices

Appendix A: 1D Parameter Scan Details.....172

Appendix B: 1D Limit Cycle Amplitude.....176

Appendix C: Generality of the *h*-*u* Interaction 179

Appendix D: Artificial Cellular Epithelia.....182

Appendix E: Empirically Characterizing the One- and 2-Cell Systems.....186

Appendix F: Range of Behavior for a Single Cell.....189

Appendix G: Representative Data for Finite State Model.....192

Abstract

Drosophila melanogaster, the fruit fly, has compound eyes consisting of around 750 facets called ommatidia, arranged in a regular hexagonal grid. Each facet is centered on a suite of 8 photoreceptor neurons (R1-R8), of which R8 is the first retinal cell to attain a specific fate. In this dissertation I present a multiscale model of R8 photoreceptor specification in the developing eye imaginal disc. This pattern-forming system is characterized by an expanding field of R8 cells arranged in a regular hexagonal pattern formed behind a wave of distortion and differentiation known as the morphogenetic furrow. The basic model consists of ordinary differential equations defined on a lattice representing a cellular epithelium, and is based on observed genetic interactions centered on the proneural transcription factor-encoding gene *atonal*. It includes cell-autonomous autoactivation, long-range diffusible activation, and shorter-range inhibition. Patterning very similar to that observed in the eye can be observed given appropriate choice of parameters and initial conditions.

First, I examine a simplified version of the model analytically, explaining its basic behavior and exposing the multiscale nature of the process. If the propagation of the pattern is slow compared to the more local activity of cell differentiation, regular patterns with single R8 cells are generated reliably, and the system is very robust to parameter changes.

Next, I investigate the system in restricted 2D cases. I find that the behavior of the system is well-explained for regimes of interest by starting with a simple case, and applying the results to successively more complex systems. Specifically, I characterize the model's behavior at the levels of a single cell, two cells, several cells, and small patches of epithelium. I use these results to make specific predictions and to explain the patterning behavior of eye-discs.

Lastly, I examine the application of modeling small groups of cells to long-range patterning. I accomplish this by approximating the overall system as a finite-state machine. This represents a new theory of neural fate specification in the eye disc, and provides an ample basis for future experimental and theoretical work.

Chapter I:

Introduction

In this thesis I present a model of R8 specification in the *Drosophila* eye. This is a basic and compelling system for the study of pattern formation in biological systems (1-4). The simplicity and regularity of the pattern produced (a steadily expanding hexagonal grid of cells producing a particular transcription factor) gives hope that the system might be understood in something approaching its entirety, and the large body of knowledge on the underlying genetics provides a solid starting point for bottom-up modeling (1-3, 5). Indeed, starting with known genetic interactions, one can build a mathematical model that produces a patterning system very similar to that observed in real fly eyes (6).

Organization and Multiscale Approach

What happened when we set out to analyze the mechanism of this formal, mathematical system was surprising. Despite the simplicity of the interactions that form the basis of the model, and despite the simplicity of the end results (the hexagonal pattern), the pattern seemed to propagate by no known mechanism. This was interesting, and observations quickly piled up. The model made unexpected predictions, which were subsequently, empirically, proven correct by experiment. At some point we realized that whatever was going on to produce these behaviors, it was very difficult to reduce to a

single process, and progress became possible when we started treating the system as multiscale.

The first task in analyzing the pattern formation system as a multiscale model involved casting it in its simplest possible form: 1D instead of 2D, and with a minimal set of fields and parameters. The (empirically observed) genetic interactions put into the model turned out to function in very distinct, modular ways, in this context. One of these modules involved the stabilization of local transcriptional states, and the other extended the patterned field by destabilizing the transcriptionally inactive state. We were able to separately analyze these two processes and recombine the results to get complete solutions to the patterning system. This produced a wealth of knowledge about the existence and stability of pattern-forming solutions, and confirmed our suspicion that for patterning to occur reliably, the two processes had to have very different intrinsic rates. The problem was, indeed, very naturally multiscale. A few interesting findings came from this work, namely the fact that the patterning mechanism was entirely new, and that it exhibited breathtaking robustness to parameter variations within a few simple constraints. I will discuss this work in Chapter II.

The initial discovery of a new patterning mechanism was exciting, and the implications interesting, but the work was very formal, and likely too simplified to apply directly to biological observations. We set out to generalize the results to 2 dimensions (appropriate for a cellular epithelium) and a more complex genetic model. Forewarned, this time, we broke this system into the same functional modules as the simpler model. We expected, given that the system was more complex in several ways, that each of the sub-problems would be more difficult. We treated the small, fast, local subsystem first.

It was surprising how well it yielded to further sub-division. Due to the discrete nature of the system, there were three distinct levels meriting their own analysis: A point-like system consisting of one cell, a high-symmetry system of several equivalent cells, and systems that are large enough that their embedding in 2D is important. Interestingly, analysis of these subsystems yielded a wealth of explanations and experimental predictions for biological systems. It also reopened the issue of proneural cluster resolution (the process by which a single cell from amongst several precursors is selected to become a neuron), and suggested that, in the eye disc, at least, this does not proceed by the textbook mechanism (3,7-14). This work is discussed in Chapter III.

The largest scale we address, here, is also the one that captured our attention in the beginning: The formation of a particular, long-range, regular pattern. This, again, is much more complicated than the slow, long-range 1D system of Chapter II, and it has turned out to be very interesting, indeed. Over the course of Chapters II and III, we repeatedly reduced continuously variable systems of ODEs to binary or other simple systems. This pays dividends in Chapter IV, in which discretized time, and discrete pattern states lead us to treat the whole system from the perspective of finite state machines and symbolic dynamics. It should become clear, at this point, why the original attempts at explaining this patterning system in terms of continuous ODEs or, even worse, PDEs didn't work. The continuous equations exist, but set up fundamentally different systems in certain (easily achieved) limits, and it is these systems that are more easily understood as pattern-forming. This largest level presents an almost impossibly rich area of study, but I will discuss several results and applications that have to do with large-scale patterning.

Now that you know where we're going, in fairly vague terms, I will spend the remainder of the introduction relating enough of the pertinent background information for the details presented in chapters II through IV to make sense, and for the implications to be clear.

The *Drosophila* Eye

The fruit fly *Drosophila melanogaster*, being an insect, has a compound eye composed of about 750 facets, called ommatidia (15). Each ommatidium in the adult eye is centered on a suite of 8 photoreceptor neurons (R1-8), and has a total membership of 20 cells (16). The ommatidia are remarkable for their identical appearance and the fact that they are packed into a perfect hexagonal, crystalline array in the adult eye (1-4,17). These clusters of cells are not clonally derived, but begin differentiating from the unpatterned retinal epithelium of the eye-antenna imaginal disc during the third instar period of larval development (2,18). Each ommatidium is founded by a single cell expressing the proneural basic helix-loop-helix (bHLH) gene *atonal* (*ato*), which will eventually become the R8 photoreceptor (19,20). These cells are specified and begin differentiating as a front of physical distortion (the morphogenetic furrow, MF) moves across the epithelium from posterior to anterior (2,18). In front of the MF the cells are unpatterned, while behind the MF one finds a characteristic hexagonal pattern of single cells expressing *atonal* against a background of undifferentiated cells. This process has been reviewed extensively, and used as a modeling target (1-4,21-23). In subsequent steps, each R8 cell interacts with the surrounding epithelium, inducing adjacent cells to differentiate into the other neurons and supporting cells observed in the adult eye (2,20-24).

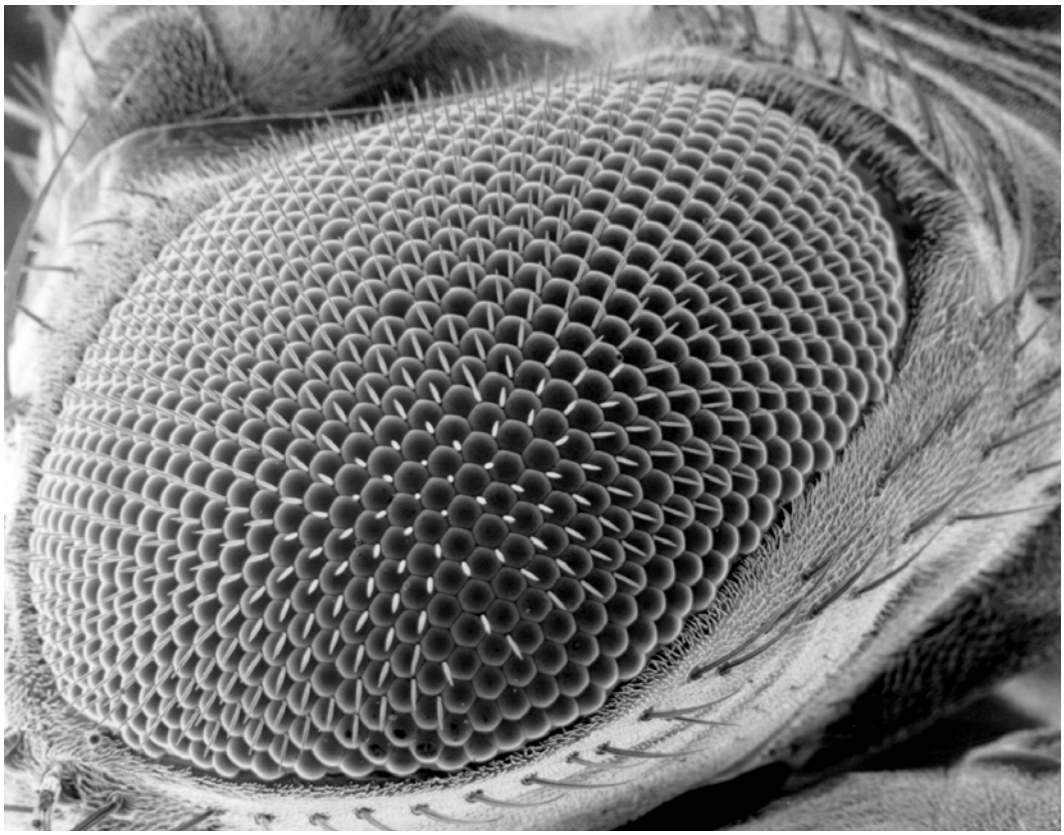

Figure 1: Adult *Drosophila* eye, scanning electron micrograph. In this image the overall structure of the adult eye is clearly visible. Each facet corresponds to an ommatidium, and sits in front of eight photoreceptors, R1-8, as well as supporting cells. There are roughly 750 ommatidia in each eye, and they form a regular hexagonal array. Photo Courtesy of the Dartmouth Electron Microscope Facility. (15,25)

After retinal specification, and furrow initiation, progress of the MF is driven by chemical morphogens secreted by the differentiating neurons behind it, specifically Hedgehog (1-3,26-30). The secreted factor Decapentaplegic is expressed near the boundary of activation of Hedgehog signaling (26). In addition to driving the MF itself, Hedgehog is considered to be a key factor in promoting the differentiation of cells as the MF traverses them (1-3). The proneural gene *atonal* encodes a bHLH transcription factor that becomes active upon dimerization with the product of the gene *daughterless*, and is the characteristic proneural gene for R8 specification (19,20,33). The expression of *atonal* is initially diffuse, but is refined to single (future R8) cells as the MF passes, and the R8 fate becomes irreversible (1-3,17,32,33,46,47).

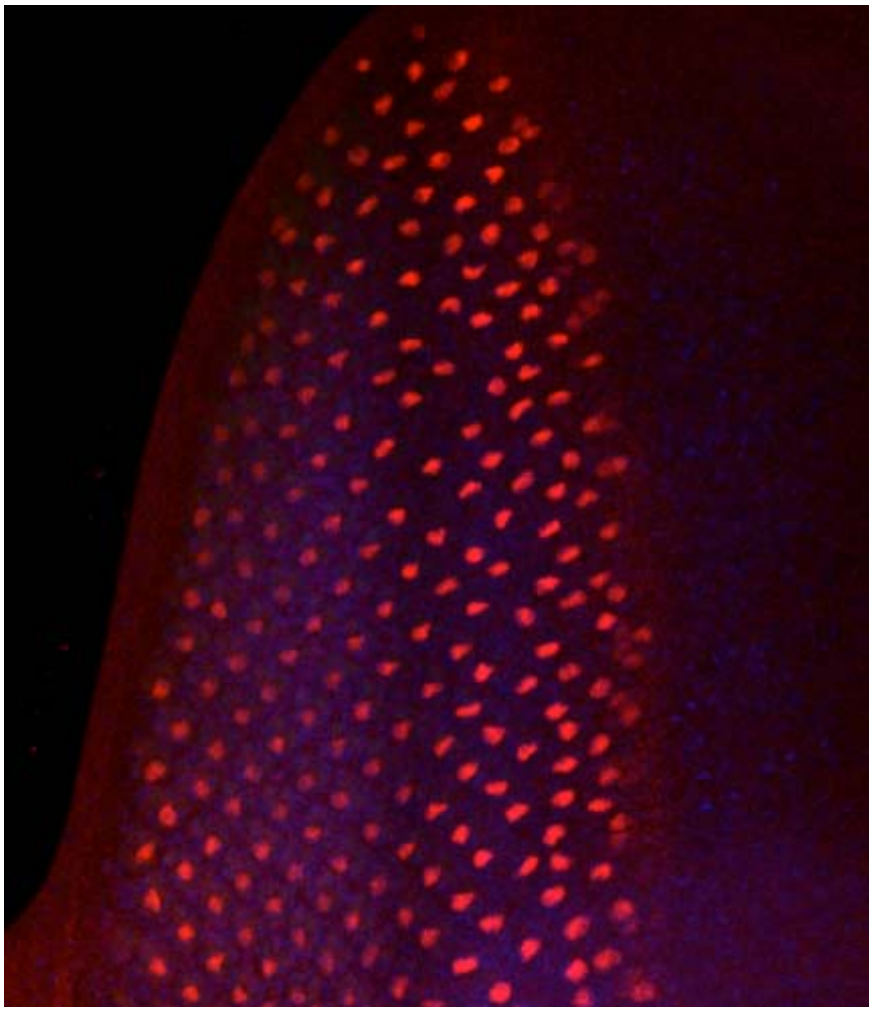

Figure 2: A third-instar eye disc with Senseless stained. This is the origin of the hexagonal pattern observed in the adult eye. The retinal field (of which this image is roughly the posterior-dorsal quadrant) is unpatterned until a wave of distortion and differentiating activity, the morphogenetic furrow (MF), proceeds across it from posterior to anterior (left to right, in this image. The MF is slightly further to the right than the right-most stained cells). Behind the MF, R8 cells have been specified in a regular hexagonal array, and can be identified by their expression of *atonal* (or other genes, like *senseless*). These R8 cells then go on to initiate a cascade of recruitment that results in local cells becoming the other photoreceptors and support cells of the ommatidium. Photo courtesy of Nick Baker. (1-3,31)

Because the columns (columns are parallel to the MF, rows are perpendicular) of R8 cells are specified sequentially, and the positions of R8 cells in sequential columns are so strongly correlated (each column is staggered along its long axis by one-half a row spacing, producing a hexagonal packing of R8s), it seems likely that each column is specified using the previous one as a template (1-3). The idea that each *ato*-expressing cell is able to inhibit its neighbors and prevent or suppress their *ato*-production is termed lateral inhibition (34). The detailed molecular mechanism of this inhibition is not known, though *Notch* is certainly integral to it, as is the Notch-ligand Delta (34,36,37,40-42,46). Loss of function (LOF) phenotypes for either of these genes result in an overpopulation of R8 photoreceptors (45-47). There are other genes involved in the patterning process with more subtle phenotypes, however, including *Epidermal growth factor receptor* (*Egfr*), *echinoid* (*ed*), and *scabrous* (*sca*) (48-58). The translated product of *scabrous* is secreted and has been shown to associate directly with Notch, though the scope of its physiologic role is uncertain (54). In eye development, *scabrous* LOF results in a phenotype with too many R8 cells, which are arranged in a much less perfect array than observed in WT flies (50). Additionally, in *sca*- flies there are many more of the specific patterning defect known as twinned R8s, in which two adjacent cells both attain R8 fate, an extremely rare occurrence in WT (49).

To understand the process by which a secreted activator, secreted inhibitors, and cells with multistable internal networks of transcription factors could lead to this behavior, Lubensky and colleagues decided to produce a minimal, bottom-up mathematical model of the system incorporating the interactions known from genetic studies (6). The cellular regulation network and the simplification used to study

patterning are shown in Figure 5. The minimal effects that seemed most important to address in a model included a long-range, diffusible activator that would promote differentiation, and, through other factors, its own production, as is observed with the *Hedgehog* gene; at least one transcription factor capable of sustaining its own production locally through autoactivation, as evidenced by *ato;* and some inhibitory mechanism by which a cell with high *ato* would tend to repress *ato* in nearby cells. The model consisted of coupled differential equations on a lattice representing auto-activation, long-range diffusible activation, and short-range diffusible inhibition, and was able to produce, for appropriate choice of parameters, solutions to the equations that represented propagating waves of activation leading to the specification of a hexagonal array of single cells expressing the transcription factor. More significantly, they were also able to produce a stable pattern of stripes of R8 cells behind the MF if the hexagonal template was destroyed. This predicted an interesting phenotype observed when a *sca*- eye disc has lateral inhibition through Notch temporarily knocked out by a temperature-sensitive allele, and is illustrated in Figure 4 (6,31).

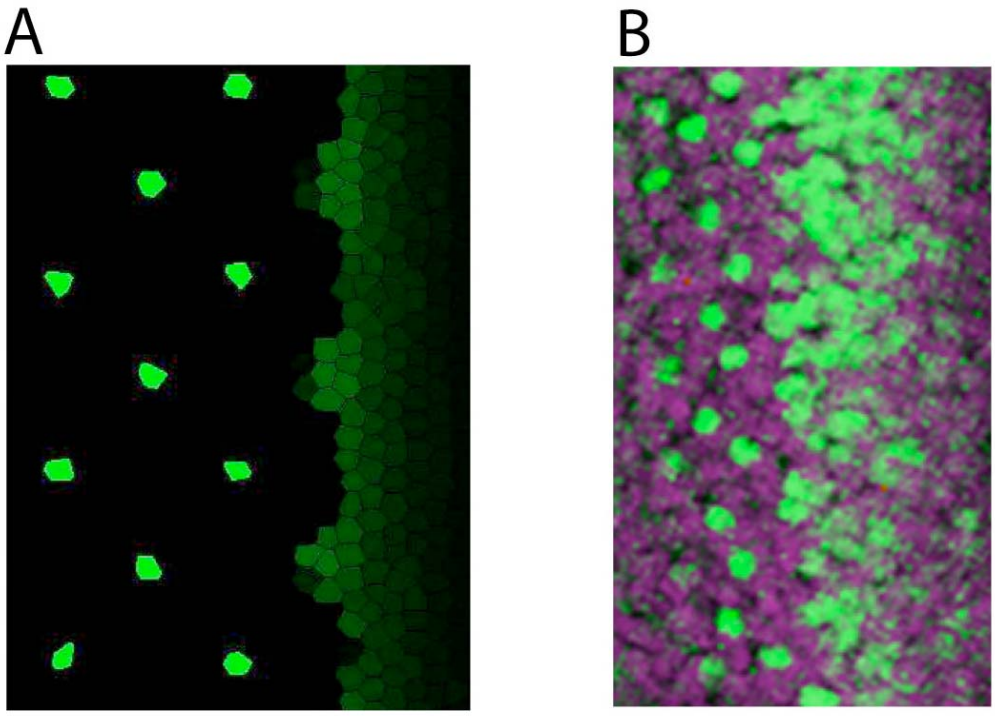

Figure 3: Simulation compared to eye disc patterning. A) Shows a simulation by Lubensky, et al. of their pattern-forming model on a random grid of cells. The green color is the variable, *a*, which represents (roughly) the proneural bHLH transcription factor Atonal. B) Shows an eye disc image stained for Atonal (green) and another nuclear gene product, Dac (magenta), shown for contrast. The resemblance between simulation and real world is striking. Simulation courtesy of David Lubensky, photograph courtesy of Nick Baker.

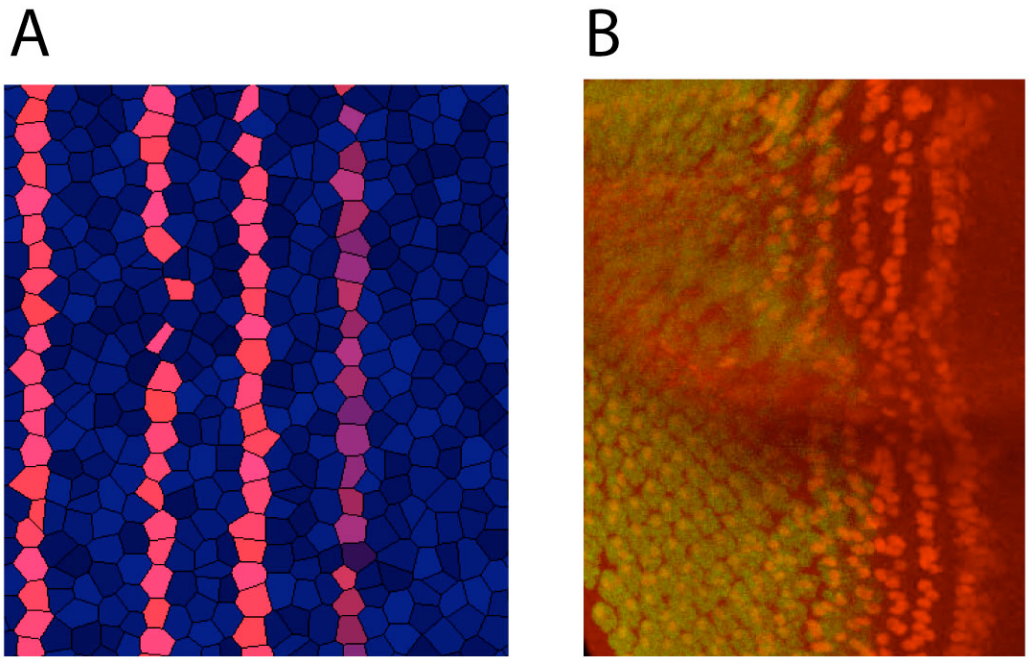

Figure 4: Stripes in simulation and eye disc. A) Shows a simulation with defective inhibition (compared to a hexagonal patterning, as in Figure 3) given a stripe initial condition. In this case the color red is related to the model variable, *s*, which (roughly) represents Senseless. A pattern of stripes of R8s is propagating down the field behind the MF. B) an eye disc stained for Senseless (red), and Elav (green, a marker of neuronal differentiation). This eye disc has a loss-of-function mutation in the gene *scabrous*, which encodes a secreted protein involved in inhibition, and a conditional (temperature sensitive) allele of *Notch*, which transduces inhibition. When the MF was near the middle of the region shown, the temperature of the larvae was reduced, and Notch ceased to function until the permissive temperature was restored. This resulted in a destruction of the template pattern produced by the hexagonal array of cells, and led to a pattern of stripes being formed behind the MF, henceforth. Photograph courtesy of Nick Baker.

This finding motivates the further study of their main conclusion: that patterning in the *Drosophila* eye proceeds by a novel, non-Turing, non-competitive, non-oscillator mechanism, by a process resembling crystal growth through epitaxy. In this thesis, I will examine this model more closely and try to gain an analytic understanding of how it works and what conditions it requires. This is a problem in multiscale modeling, in which I break down the genetic interactions in a single cell to their fundamental properties, and use this simplified understanding as a functional module to assist in understanding the next larger system (two cells, in this case), which I will use to understand 7 cells, etc., up to the tissue patterning level.

The model itself consists of three or four fields defined on a spatial lattice where each node is taken to represent a single cell. It is important to note that, in the interest of making a model that illuminates the mechanism of patterning, we do not model individual genes, *per se*, but observed genetic interactions (59). Thus, each field, and each arrow may represent the collective action of one or two different molecular species, or the overall activation of an entire pathway. The version with three fields, which I consider in Chapter II, includes a non-diffusing, auto-activating, transcription factor a (analogous to *ato*, and representing the overall neurogenic status of the cell), a diffusible inhibitor, u (representing the observed action of the Notch-Delta pathway, though not in mechanistic detail, which remains somewhat obscure in this case, and involves many genes, including *scabrous*), and a diffusible activator h (representing Hedgehog signaling, and the overall differentiating signal that progresses with the MF). A nearest-neighbor hopping term represents diffusive transport of the mobile factors. An expanded version of the model with a second transcription factor, *s*, in a mutually positive feedback

loop with *a* is needed to recapitulate the proneural clusters observed in eye discs. I use this model in the generalization to small 2D systems contained in Chapter III. I also use this model when a specific model is called for in the long-range patterning studies of Chapter IV, though much of the discussion of that work is model-independent.

The motivation behind this model was to couple the genetic subsystems known to exist in the developing eye disc, which are critical to its basic behavior, and observe their function. The regulatory network that results has the appearance of one that was made by coupling *functional* subsystems (a opposed to the *structural* subsystems they are): one that supports a propagating front, namely an auto-activator with cooperative nearest-neighbor effects, and another that can support stable patterns of activation, namely a short-range activator and a longer-range inhibitor (4,60,61). Evidence puts *ato*, the non-diffusing activator, in the master role, promoting the generation of both the positive and negative diffusible signals (2,32,34). The effects of these signals are then "felt" as they feed back on *ato*. Pursuing this functional separation of subsystems aids our understanding of the system.

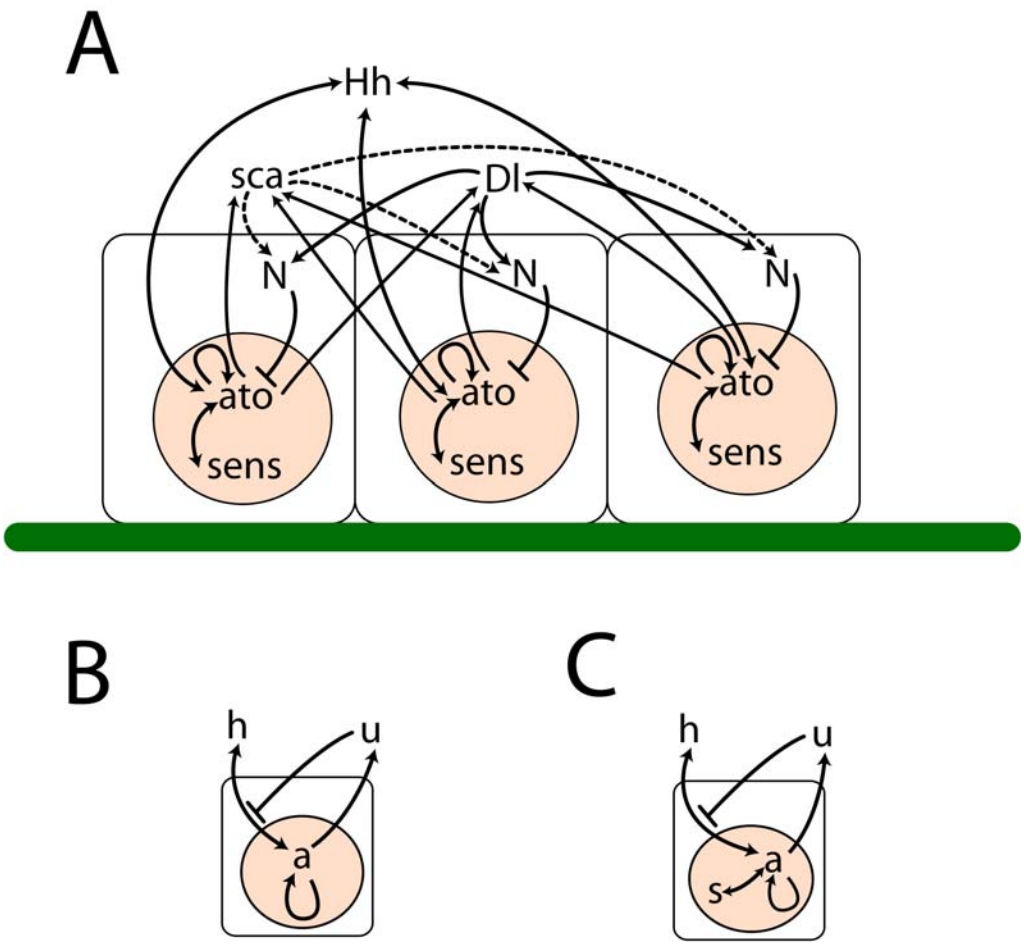

Figure 5: Regulation Network Diagram. A) a simplified regulation network showing some interactions involved in patterning. Dotted lines represent genetically-defined interactions which are not understood in mechanistic detail. In some situations, Notch activity can stimulate proneural activity. Delta is generally membrane-bound, but is able to act at considerable apparent distances by the extension of filipodia. There is considerable evidence in this, and related systems, that *Egfr* activity interacts considerably with Notch signaling. Notch signaling, in general, proceeds when ligand binding to the Notch receptor allows the Notch intracellular domain to be cleaved off. This is then transported to the nucleus where it interacts with the inhibitor *Suppressor of Hairless* to remove inhibition on the *Enhancer of split* (*E(spl)*)complex of transcription factors. In turn, *E(spl)* inhibits *ato* expression. It should be clear that even the "complicated" network shown here is a major simplification of the gene-by-gene signaling network. B) A further simplification of the regulatory network, as studied in Chapter II. Diffusible activating activity is lumped onto *h*, with inhibitory activity lumped onto *u*. The variable *a* represents the state of internal proneural signaling. C) The regulatory network studied in Chapters III-IV, where a second transcription factor, *s*, allows staged activation of proneural activity. (62-66)

Modeling Biological Pattern Formation

The next section introduces a few systems that form patterns that have been studied in a biological context. I will be brief, since their main role in the rest of this work is as a counterpoint: Things that we can clearly demonstrate are not happening in the R8 model.

Morphogen gradients

Most fundamental to the field of biological pattern formation, which studies the introduction of reliable and complex order to an initially homogeneous system (the ovum), is the concept of the morphogen. This is usually defined as a diffusible chemical capable of inducing cells to attain different fates as a function of its concentration (2). The canonical morphogen is Bicoid, a maternal factor that induces anterior-posterior (AP) polarity to the *Drosophila* embryo (67-68,70). The *bicoid* mRNA is fixed in one pole of the embryonic syncytium (which defines "anterior"), and protein is translated locally (69). The protein (a transcription factor) is diffusible, and produces a gradient that decreases in concentration towards the posterior pole of the embryo (67). The Wolpert "French Flag" model of patterning is a conceptual touchstone relating to this morphogen gradient, and gets its name from the determination of three different cell types (*bleu*, *blanc*, *rouge*…) arrayed along the anterior-posterior (AP) axis (71). In the simplest formulation this pattern is the result of fate-determining transcription factors that are activated at different concentrations of Bicoid protein. There is truth in this model, but it is more a starting point than a complete understanding. The observed robustness of patterning along the AP axis to variations in embryo size, for instance, is poorly predicted by a static threshold model unless all protein degradation occurs at the embryo's posterior

pole, and is a current focus of theoretical efforts (72-84). The French flag (and many other morphogen-based models of patterning) is a steady-state model of pattern formation. There are certain analogies to be drawn with the R8 patterning system, but no static morphogen picture can hold true for very long in this process, as it is highly dynamic and iterative. The concept of an activation threshold will be very important, though.

Distinct models have been proposed to explain the observed robustness of morphogen gradients and their interpretation in the Drosophila embryo. Bicoid, as well as Decapentaplegic (*dpp*) signaling, which plays a role in Dorsal-Ventral (DV) patterning, are focuses of these studies (72-84). A system with a Bicoid-like inducer gradient, with an inhibitory gradient oriented in the opposite direction, which is interpreted by cells in such a way that a boundary is fixed where activation and inhibition are equal in magnitude can divide a patterning field (embryo) into fields of constant relative size, regardless of fluctuations in the overall size of the embryo (72). This can also be effected by having a counterpropagating activator and inhibitor that interact stoichiometrically to diminish each others effect (83). A different robustness mechanism, validated for the DV system in flies as well as *Xenopus*, involves the active shuttling of Dpp (or its frog homologue, Admp) toward the dorsal portion of the embryo, where the inhibitor-morphogen complex is proteolytically degraded, releasing the active morphogen (75,82,84).

It has been noted that robustness of a morphogen gradient to gene dosage (taken to mean the source-strength of a diffusible morphogen), can be effected by nonlinear breakdown of that morphogen (60). Likely related to this finding is the fact that, at least

in the Hedgehog and BMP pathways, morphogens tend to be consumed by receptor-mediated endocytosis, and also tend to stimulate the production of their receptors (2, 75, 82, 84).

Turing-unstable and related systems

Alan Turing, famous primarily for his epochal work on computation and cryptographic theory, has, it could be argued, dominated the field of biological pattern formation for more than 50 years. He realized that diffusion coupled with appropriate chemical reactions could act to increase the spatial gradients of chemical species, not just to dissipate them (85). Thus, the Turing instability entered the scene. A Turing instability is a particular type of stability associated with a homogeneous steady state and characterized by a balance between competing but coupled processes. In a spatial system a large-amplitude pattern can arise from small fluctuations if the activating component is much more local than the stabilizing inhibitory feedback. In linear stability analysis, this is represented by instability of the steady state to certain, finite-wavelength perturbations, but stability to others, specifically spatially homogeneous ones, and its presence (or absence) is easily confirmed.

The nature of the Turing instability is worth reviewing here. Take a two-component reaction diffusion system defined in 1D:

$$\begin{aligned} \partial_t a(t,x) &= f(a,u) + D_a \partial_{xx} a \\ \partial_t u(t,x) &= g(a,u) + D_u \partial_{xx} u \end{aligned} \qquad \textbf{(1)}$$

We will eventually take a to be an activator, and u an inhibitor. Setting all the derivatives equal to zero, we solve for a homogeneous steady state, and define new variables η_1 and η_2, as below.

$$
\begin{aligned}
&a = a_0, u = u_0 \Leftrightarrow \partial_{xx} a = \partial_{xx} u = \partial_t a = \partial_t u = 0 \\
&\eta_1(t,x) = a(t,x) - a_0 \\
&\eta_2(t,x) = u(t,x) - u_0
\end{aligned}
\tag{2}
$$

Linearizing the equations about the steady state then gives the following, with the local Jacobian replacing the nonlinear reaction terms.

$$
\begin{aligned}
\partial_t \eta_1(t,x) &\approx \left.\tfrac{\partial f}{\partial a}\right|_{a=a_0,u=u_0} \eta_1 + \left.\tfrac{\partial f}{\partial u}\right|_{a=a_0,u=u_0} \eta_2 + D_a \partial_{xx} \eta_1 \\
\partial_t \eta_2(t,x) &\approx \left.\tfrac{\partial g}{\partial a}\right|_{a=a_0,u=u_0} \eta_1 + \left.\tfrac{\partial g}{\partial u}\right|_{a=a_0,u=u_0} \eta_2 + D_u \partial_{xx} \eta_2
\end{aligned}
\tag{3}
$$

The key to finding a Turing instability is to look for stability as a function of perturbation spatial-scale by taking the spatial Fourier transform of the linearized equations:

$$
\mathrm{H}(q) = \frac{1}{\sqrt{2\pi}} \int_{-\infty}^{\infty} \eta(x) e^{iqx}
\tag{4}
$$

This gives the following system of linear ordinary differential equations (ODEs).

$$
\begin{aligned}
\partial_t \mathrm{H}_1(t,q) &= \left.\tfrac{\partial f}{\partial a}\right|_{a=a_0,u=u_0} \mathrm{H}_1 + \left.\tfrac{\partial f}{\partial u}\right|_{a=a_0,u=u_0} \mathrm{H}_2 - q^2 D_a \mathrm{H}_1 \\
\partial_t \mathrm{H}_2(t,q) &= \left.\tfrac{\partial g}{\partial a}\right|_{a=a_0,u=u_0} \mathrm{H}_1 + \left.\tfrac{\partial g}{\partial u}\right|_{a=a_0,u=u_0} \mathrm{H}_2 - q^2 D_u \mathrm{H}_2
\end{aligned}
\tag{5}
$$

Or, equivalently, where we have collected terms and simplified notation:

$$
\bar{\mathrm{H}}' = \begin{pmatrix} \partial_a f - q^2 D_a & \partial_u f \\ \partial_a g & \partial_u g - q^2 D_u \end{pmatrix} \bar{\mathrm{H}}
\tag{6}
$$

The solutions to linear, homogeneous ODEs are summarized by the eigenvalues of the Jacobian, which satisfy the following relationship, where we have further simplified notation, and introduced the eigenvalue, λ.

$$\begin{vmatrix} f_a - q^2 D_a - \lambda & f_u \\ g_a & g_u - q^2 D_u - \lambda \end{vmatrix} = 0 \qquad \textbf{(7)}$$

Since we already defined their roles, we can set f_a and g_a to positive values and f_u and g_u to negative ones. Under these conditions (as well as others less relevant to the current discussion), it is possible for the largest eigenvalue to be a positive real number for a finite range of q. This is illustrated in Figure 6, where it is also clear that the stability to perturbations is decreased as D_u is increased relative to D_a.

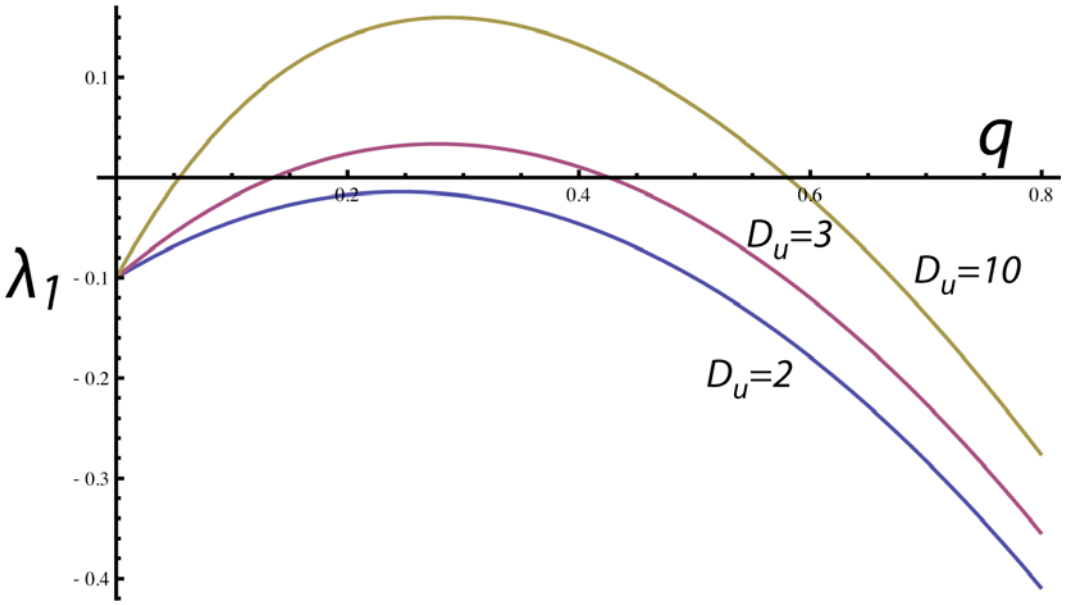

Figure 6: Turing instability in a 2-component reaction diffusion system. This figure illustrates the larger of the two eigenvalues (representing symmetric perturbations to *a* and *u*) for the activator-inhibitor system defined by equation (1) as a function of wave-number, *q*. In this case, f_a=.4, f_u=-.5, g_a=.5, g_u=-.6, and D_a=1; D_u is varied as shown. For low enough D_u, the system is stable to linearly-small perturbations of all wavelengths. At higher D_u a finite range of wave-numbers becomes unstable, and an initially small-amplitude perturbation will grow.

One difficulty involved in applying the classic Turing pattern paradigm to biological systems is the fact that on a developmental scale, chemical morphogens primarily act on, and are the end result of, cellular transduction pathways. These pathways can involve numerous genes, feedbacks both positive and negative, and are likely to be incompletely characterized. In addition to functional complexity, this also suggests that these pathways do not exist in the continuous (for most purposes) medium of diffusing morphogens, but have components confined to discrete cells. The Turing instability generalizes to these conditions, with some important caveats. Here, we take the activator to be maximally local, i.e. confined to cells, as it is in R8 specification, which are represented as nodes on a 1D lattice, the inhibitor sub-system is tridiagonal, and the entire system is composed of *2N* ODEs, where *N* is the number of cells.

$$\begin{aligned} \partial_t a_x(t) &= f(a_x, u_x) \\ \partial_t u_x(t) &= g(a_x, u_x) + D_u\left(u_{(x+1)} - 2u_x + u_{(x-1)}\right) \end{aligned} \qquad \textbf{(8)}$$

The linearization of this system has a block-form Jacobian, where $\hat{I}$ is the identity matrix:

$$\begin{pmatrix} \vec{\eta}_a \\ \vec{\eta}_u \end{pmatrix}' = \begin{pmatrix} f_a\hat{I} & f_u\hat{I} \\ g_a\hat{I} & g_u + D_u\hat{t} \end{pmatrix}\begin{pmatrix} \vec{\eta}_a \\ \vec{\eta}_u \end{pmatrix} \qquad \textbf{(9)}$$

$$\hat{t} = \begin{matrix} -2 & 1 & 0 & 0 & \ldots & 1 \\ 1 & -2 & 1 & 0 & \ldots & 0 \\ 0 & 1 & -2 & 1 & \ldots & 0 \\ 0 & 0 & 1 & -2 & \ldots & 0 \\ \ldots & \ldots & \ldots & \ldots & \ldots & \ldots \\ 1 & 0 & 0 & 0 & \ldots & -2 \end{matrix} \qquad \textbf{(10)}$$

If the boundary conditions are made periodic, as in equation (10), or if we say the system is infinite, then the matrix is diagonalized by a block Fourier transform (the discrete analog of the spatial Fourier transform from the continuum case), and the eigenvalues are the solutions to the following 2x2 system, where *T(q)* is the q^{th} component of the discrete Fourier transform of the nearest neighbor diffusion operator, $\hat{t}$.

$$\begin{vmatrix} f_a - \lambda & f_u \\ g_a & g_u + D_u T(q) - \lambda \end{vmatrix} = 0 \qquad \textbf{(11)}$$

T(q) is zero at *q=0*, and decreases monotonically to minima at *q=±N/2*, which represent the smallest spatial scale of the system (alternate cells), as shown in Figure 7.

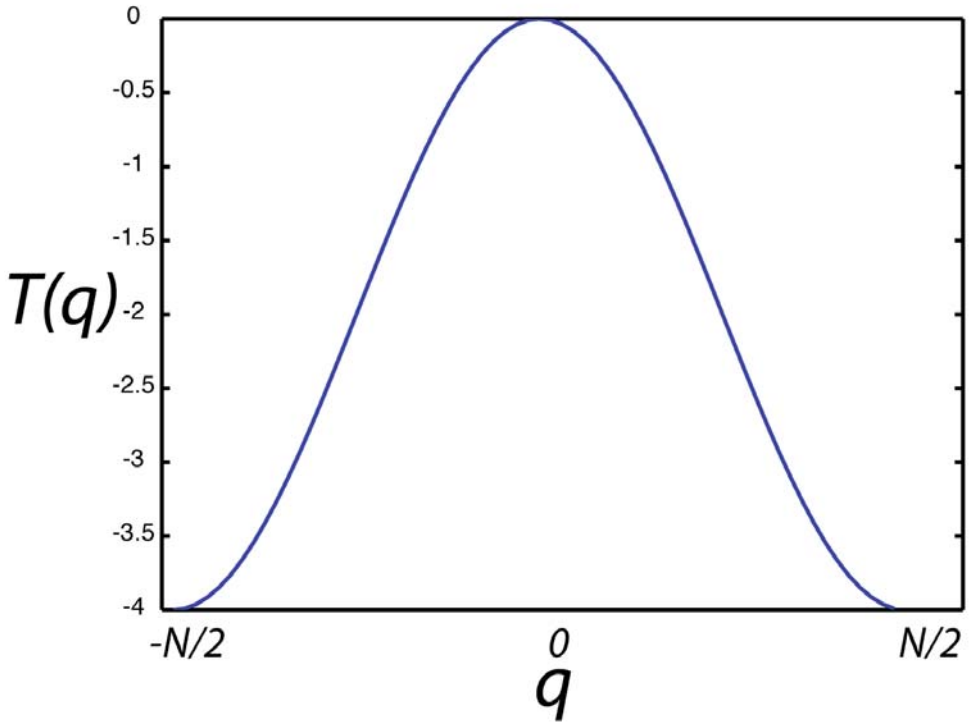

Figure 7: Fourier transform of the linear nearest neighbor diffusion operator. Extrema for the Fourier transform of nearest-neighbor diffusion exist for homogeneity (*q=0*), which is maximally stable, and the wave-numbers representing the smallest wavelength possible in the system, alternating cells (*q=±N/2*), which are maximally unstable. If any wavelengths of perturbation are unstable, these are, as well, and they are the most unstable.

In equation (11), it is clear that $T(q)$ shows up only once, multiplying D_u. Since D_u drives the instability, and is always effectively at its most powerful for $q=\pm N/2$, the most unstable mode of this system is always going to be the shortest wavelength one.

The Turing instability, then, is a linear property of a steady state that leads to the spontaneous creation of patterns from small, spatially-inhomogeneous perturbations over a finite range of spatial scales. The importance of this instability, and how it arises at bifurcations of steady states, is very great, and it is the fundamental concept behind the formation of dissipative structures in highly-driven systems (61). The patterns it produces, are, indeed, very compelling, and similarities to those observed in the animal kingdom have been catalogued at great length, by, for instance, Murray (86). Relating a spontaneous pattern formation event in development to a demonstrably Turing-unstable molecular system has proven very difficult, and it is not clear if this mechanism is used at all routinely by biology, though putative Turing systems have been characterized (87,88). The specification of barb ridges in embryonic chick feathers, dependent on Sonic Hedgehog (activator) and BMP-2 (inhibitor), appears to occur by a Turing mechanism, which illuminates the way in which these ridges form and bifurcate as the feather grows (87). Similarly, but in an intrinsically 2D geometry, WNT and DKK (activator and inhibitor) signaling have been argued to produce the hair-follicle spacing in the skin of mice by formation of a Turing pattern, and the clumping of hair follicles in mutants with increased inhibition was successfully predicted by modeling (88). The continuum Turing system is important conceptually as reaction-diffusion-type systems are a very natural fit for modeling developmental patterning.

Chemotactic eukaryotic cells, such as the *Dictyostelium* amoeba or neutrophils are able to polarize their bodies in relation to an external chemical gradient in order to move in a specific direction. They exhibit this behavior in a largely invariant way over a very large range of gradient strengths and baseline chemoattractant concentrations. They are also able to change the orientation of their polarization as the gradient changes direction (89,90). Through a simple model, in which a chemoattractant induces production of a "readout substance" at the cell membrane, as well as a fast-diffusing cytosolic inhibitor (a system that, on the face of it, could exhibit a Turing instability), the behavior in which a formed pattern does not persist if the original symmetry-breaking input is changed can be replicated (89). The system, in this case, is not unstable, *per se*, but merely very, very sensitive over a large dynamic range (89, 91). Termed "balanced inactivation," this illustrates the fact that not all patterns produced by activator inhibitor systems are Turing patterns. Each model must be examined in detail to determine the mechanism at work.

If an activator is confined to a cell (as a self-activating transcription factor would be), and a related inhibitor diffuses normally, the first wavelength to become unstable at a Turing bifurcation will always be on the order of two cell diameters. This case is realized in the classic understanding of Delta-Notch lateral inhibition, and is thought to lead to the consistent selection of isolated cells expressing Delta. The mathematical system has been studied quite extensively (92-101). In accordance with the analysis of the discrete Turing system, above, it is found that stable patterns with wavelengths on the order of a single cell are formed very naturally in systems where cells directly inhibit their neighbors, an interaction known as juxtacrine signaling, and obviously pertinent to classic lateral inhibition (93). In order to get patterns with longer wavelengths from this kind of model,

however, it has been necessary to replace the lateral inhibition interaction with a positive lateral interaction, which allows the generation of a 1D pattern of stripes in a 2D grid of cells (98). This is a significant contortion of Delta-Notch signaling as we know it, and the wavelength of the pattern generated in this case is strongly dependent on the strength of the positive lateral interaction.

An instability-driven mechanism for patterning isolated trichoblasts around the growing *Arabidopsis* root tip has been proposed and explored by experiment and simulation (102,103). This system is thought to act by a mechanism very similar, on a mathematical level, to classical Delta-Notch lateral inhibition, but involves entirely different molecular components, and the direct exchange of the transcription factor GLABRA3 and its inhibitor CAPRICE. Arranged about the circumference of a root tip, 8 trichoblasts, separated by single non-trichoblast cells are specified consistently as the root grows (102). With evidence of lateral inhibition in this system, as well as the impressive robustness with which such a system gives the observed pattern, this may be considered a particular triumph of a discrete Turing-like system.

Other patterning modalities

A particularly interesting patterning system that has received much attention, lately, is the one that initially patterns somites in vertebrate embryos. In this system, which specifies the fate of the mesoderm along the cranial-caudal axis, synchronized oscillations in signaling activity interact with a propagating wave of differentiating activity to produce a spatially periodic pattern (104-109). In an extremely stripped-down, mathematical way we can summarize this type of model as follows, where *h* represents a

traveling wave of activity with finite spatial extent (more like a traveling pulse of activity), and *a* a cellular process that is periodic and synchronized across many cells.

$$h(t,x) = h(vt - x)$$
$$a(t,x) = a\left(e^{i\omega t}\right) \quad \textbf{(12)}$$

The local interaction of these processes could be "read" by many possible mechanisms, but if the domain is taken to be infinite, along with time, the output, *s*, will be periodic in space. This can be called clock-and-wavefront patterning.

$$s(x) = \int_{-\infty}^{\infty} f(h \cdot a)\,dt = s\left(e^{i\frac{\omega}{v}x}\right) \quad \textbf{(13)}$$

This is illustrated in Figure 8.

French-flag type systems, and systems where thresholds are applied to Turing patterns of morphogens, are sometimes referred to as systems involving prepatterns (2, 104). In this class of model, a cell "reads" information about its intended fate from its environment, in this case morphogen concentration, and differentiates accordingly. The pattern eventually expressed preexisted the observed outcome, and some aspect of that original prepattern has been preserved and propagated. A second class of models refers most typically to the selection of single neurons from amongst groups of proneural cells (proneural clusters) through Delta-Notch lateral inhibition through a discrete Turing-type instability (2). In this case, the system is structured such that a large-amplitude pattern is guaranteed to arise from the structure of the system, regardless of input. This involves the instability of symmetric states, and symmetry breaking by small fluctuations. This type of process is variation-generating, in that no prepattern is needed, and, in the case of

true equivalence of potential precursor cells, results in random fate assignments. A pattern-formation process need not strictly belong to either of these classifications, but they provide useful points of reference for understanding the problem.

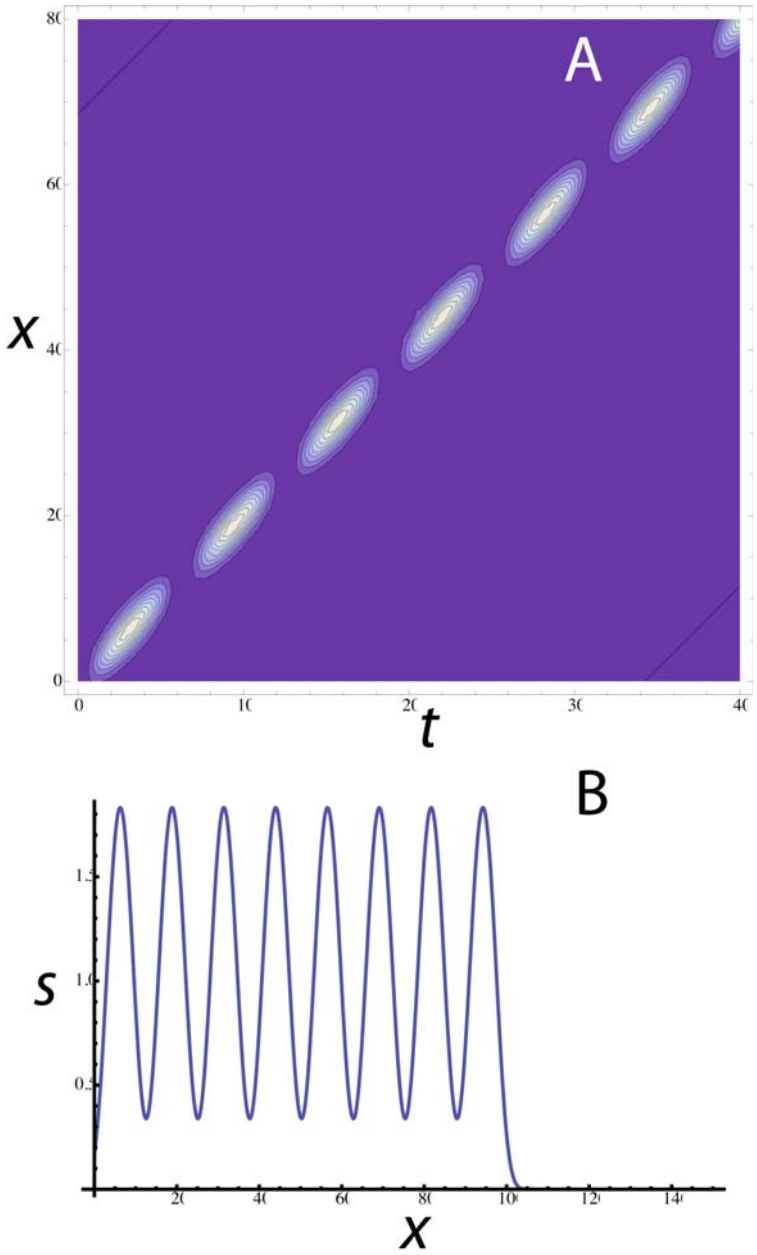

Figure 8: Clock-and-wavefront patterning. In this very formal example of clock and wave patterning, a substrate field has an oscillating property (*a*) that we can call "activatability," and a Gaussian-shaped pulse of "activation" (*h*) proceeds across it. A) shows the patterning activity as a function of time and space. It is clear that in sequential periods of the "clock" a new group of cells is signaled. B) shows a simple spatial pattern specified by this system as it works. The output, *s*, is read in this case by simply integrating the total, time-integrated product of the two signals, and shows a clearly periodic pattern.

How is one to classify a clock-and-wavefront system as a prepattern or instability-driven patterning system? And, for that matter, where does our R8 system fit in? In both these cases, neither class is wholly satisfying. If we are to look at the specification of a single somite, it becomes clear that clock-and-wave is an iterated prepattern system. In this case, the prepattern is the location of the differentiation-provoking wave examined at a time when the oscillator permits differentiation. The prepattern for the next somite is thus different, as the differentiating wave has moved significantly by the time the oscillator has cycled once. This system is iterative and can extend a pattern to a seemingly arbitrary size (500 somites in snakes, for instance) (108). In that way it looks very much like the system we are examining in the *Drosophila* eye, and, in fact, the genes involved, and the genetic interactions show significant overlap.

We find, however, that patterning in our system proceeds by none of these mechanisms, including clock-and-wavefront. The static morphogen picture has been discounted, already, since the system is clearly producing the pattern by a cyclic process. A Turing instability is not observed in the model, nor is any other behavior dominated by the instability of a homogeneous steady state. Furthermore, a small-wavelength pattern is not a pattern seen in the model or in the experimental system at any stage, unless we tune parameters specifically toward that goal. The initial pattern formed can be of any wavelength, despite the non-diffusing activator and nearest-neighbor-diffusing inhibitor. The clock-and-wavefront model and ours have a certain relationship, but are not the same. In our system there is no need for an oscillator. Also, the pattern's spatial scale is not determined by the specifics of any time-dependence, as it is in clock-and-wavefront, but occurs stably in an entire limit of time-scale separation. The scale of the pattern in

our model is derived from spatial scale of the inhibitor, and the fact that it is iteratively regenerated every time the MF encounters its boundary, as defined by a finite activation threshold.

Indeed, it is possible to find that a developmental system, carefully analyzed, does not fit easily into one of the classical paradigms of pattern formation, which are extremely idealized mathematical constructs. Using modeling as a descriptive scientific tool requires that we use a bottom-up approach, attempting to tease the physics of a system from what is known about both its behavior and its components. According to the well-thought-out review of Reeves *et al*, the underlying geometry and known properties of a patterning system should be built into a developmental model explicitly (110). A major part of this is adequately separating the intracellular compartment (occupied by transcription factors, among other signaling molecules), and the extracellular space where a true chemical morphogen can diffuse. Except in the case of the juxtacrine models presented above, the cellular compartmentalization of various signaling molecules is frequently a casualty of modeling analyses. In the fly eye system this would be a mistake, since the pattern is very strikingly one of isolated cells: The size and nature of a cell is clearly important. Given the nature of the experimental evidence, genetic interactions and observable gene activities are often the appropriate starting place for building a model, though models based on, for instance, the biophysics of protein-DNA interactions between specific promoters and transcription factors have also met with considerable success. It is for this reason that at least some aspect of the internal cell transcriptional network should be included in a model. It is this network that is the end effector of cell fate decisions, and to ignore it, as is often done in stories about pattern

formation by lateral inhibition, for instance, is to ignore a cellular subsystem that is likely absolutely critical in determining observable behavior. Indeed, the multistability of the cell-autonomous transcription network in the fly eye becomes the defining feature of our patterning model, and could not have been approximated in the continuum, nor without cell-autonomous factors distinct from the diffusible activator and inhibitor.

Other models that follow the prescriptions laid out above have been proposed, and have met with success. A model of Shvartsman et al. that describes the EGFR-mediated specification of the bilateral respiratory organs of the Drosophila oocyte makes explicit reference to the cellular production of diffusible factors, and their subsequent diffusion in free space, but stops short of a fully cellularized model, instead retaining a PDE model with one field that is independent of any spatial derivative (111). Using this model, they correctly predict the formation of paired respiratory structures, as well as the possibility of single or multiple respiratory structures in different contexts. This occurs by a mechanism that is not governed by the behavior near a linear instability, but by the bifurcations of stable steady states as an input parameter (prepattern) strength is varied. This has important parallels with our work, as it is the bifurcations of stable steady states (multistability), and attraction to these steady states that define the end pattern. Our system also incorporates cellular structure and the intracellular confinement of signaling pathways, and is processive instead of static.

Chapter II:

Propagating-Patterning Fronts in 1D Discrete Media

In this chapter, we use sets of equations related to the basic model equations that are designed to probe certain limits and elucidate the pattern-forming mechanism. We concern ourselves with finding model features that more directly characterize its action than do the numerical constants in the equations. Experience led us to believe that the timescales involved in pattern determination and front propagation play a central role in determining the pattern formation mechanism. Considering these timescales separately allowed us to make considerable analytic progress on the system. That the assumptions involved in our analysis are the same as those required to observe patterning suggest that our analysis has gotten to the heart of the matter. Models of this kind recapitulate experimental observations so well that our understanding of the process may be directly applicable to the natural system. Indeed, the impressive robustness of patterning to variation of model parameters is perhaps the first piece of information about the fly system that modeling has yielded.

In this Chapter, we will first discuss the detailed form of the model used for this study, including the parameters involved and how they relate to reality. We will then discuss the behavior of an isolated cell in the terms of standard nonlinear dynamics; this behavior is quite simple. We will then examine the two functional subsystems identified

previously, namely the support for propagating solutions contained in the *a*-*h* subsystem, and the support for stable patterned solutions contained in the *a*-*u* system, separately, in the 1D case. Identifying solutions to the whole model in 1D that both propagate and form patterns is the heart of the study, and we will discuss how self-consistent solutions to the sub-problems may be found, joined, and interpreted. Figure 9 illustrates the most important solution types in 1D, which depend on both parameter values and initial conditions, and which we seek to explain in this chapter. Lastly, we will discuss a random scan of far-flung parameters conducted to test the analytic understanding of the model, and the range of behaviors it supports.

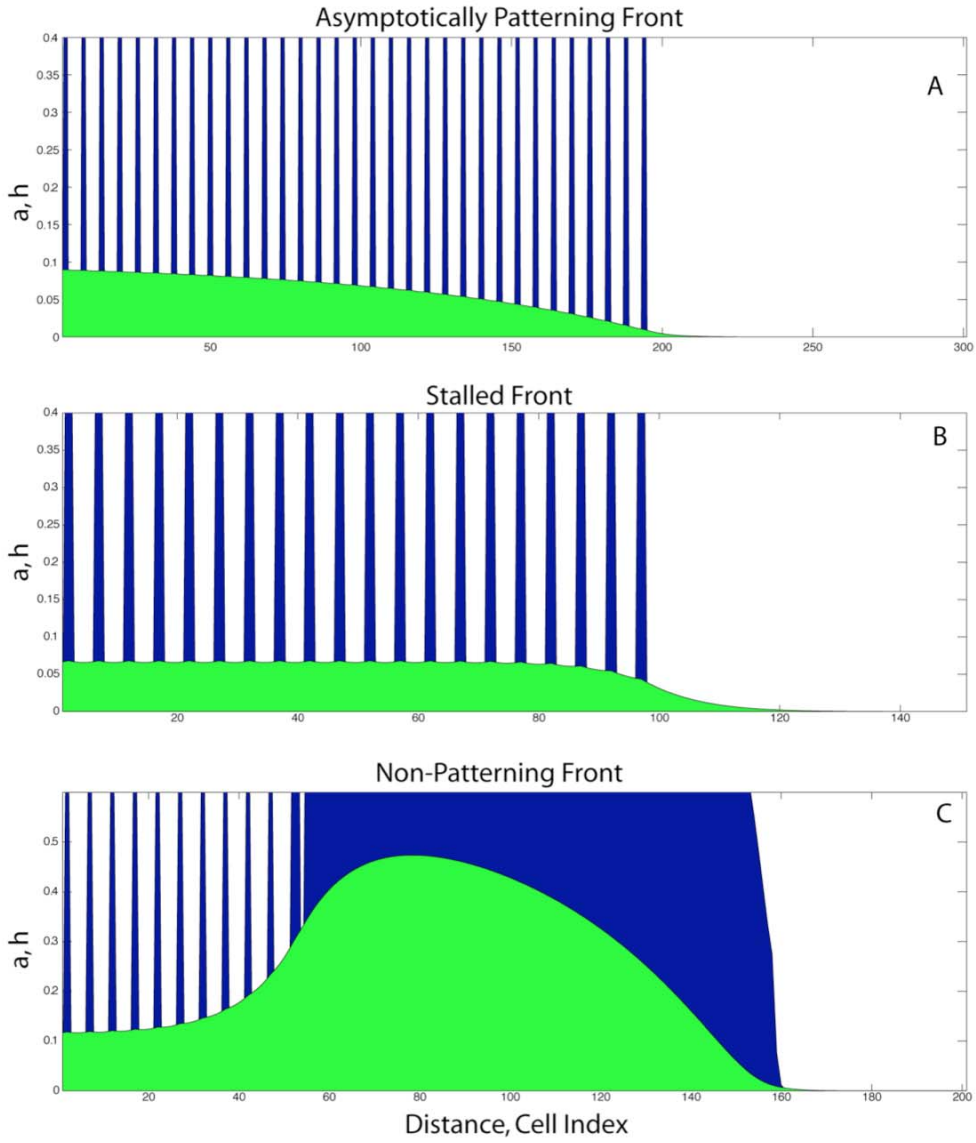

Figure 9: Examples of computed results. A) shows an asymptotically propagating front of *h* (light, green), and the stable pattern of activated *a* it produces (dark, blue). B) This situation can collapse, and propagation can fail, if the steady state *h* (shown here with a stalled front) produced by the preceding pattern does not produce adequate *h* to trigger the activation of another cell. This situation always exists for a sparse-enough prepattern. C) If the evolution of *a* and *u* is too slow for a recently activated cell to inhibit its neighbors before the *h* front gets to them, an unpatterned front of activation may exist. This solution can exist for parameter sets that otherwise have only stalled solutions, as well as ones that have patterning solutions. This simulation was derived from an identical parameter set to A, but with the characteristic timescale of *h* reduced by a factor of 8 to speed up the progress of *h*.

The Model

The three-variable model used by Lubensky *et al.* has the following non-dimensional form (6):

$$\begin{aligned}
\frac{\partial a}{\partial t} &= f_{n_a}\left(\tfrac{a}{A_a}\right) - a + G \cdot g_{m_h, m_u}\left(\tfrac{h}{H}, \tfrac{u}{U}\right) \\
\tau_h \frac{\partial h}{\partial t} &= f_{n_h}\left(\tfrac{a}{A_h}\right) - h + D_h \Delta h \\
\tau_u \frac{\partial u}{\partial t} &= f_{n_u}\left(\tfrac{a}{A_u}\right) - u + D_u \Delta u
\end{aligned} \qquad \textbf{(1)}$$

Δ is the lattice Laplace operator, and the variables a, h, and u are fields representing, respectively, a local activator (Atonal), a diffusible activator (Hedgehog, Decapentaplegic), and a diffusible inhibitor (Delta, Scabrous, acting through Notch). Each variable has been rescaled so that its natural scale is of order unity. We have chosen to non-dimensionalize time by the decay rate of a. τ_h and τ_u give the dimensionless decay times of h and u. The source term f_{n_α} in each equation is a dimensionless function with $0 \le f_{n_\alpha} \le 1$ for $0 \le a < \infty$. This restriction reflects the fundamental limits to the rate of production of any biomolecule. For simplicity, f_{n_α} has the sigmoidal form:

$$f_{n_\alpha}(a) = \frac{a^{n_\alpha}}{A_\alpha^{n_a} + a^{n_\alpha}} \qquad \textbf{(2)}$$

This adds the three dimensionless parameters A_a, A_h, and A_u that characterize the scale at which a activates production of itself, h and u, and the three Hill

coefficients n_a, n_h, and n_u. D_h and D_u are diffusion coefficients. The lattice spacing is of order 1.

There are two terms in the equation for $\frac{\partial a}{\partial t}$, beyond its (standard) linear decay. They reflect the presence of two enhancers at the *ato* gene that respond under different conditions. The first term, representing the so-called 5' enhancer, is solely responsible for autoactivation, whereas the second term, representing the so-called 3' enhancer, is responsible for transducing signals from h and u. This latter term has a maximum strength (relative to the 5' enhancer) G; the function g varies between 0 and 1. A Hill-like functional form for this interaction offers, once more, the desired behavior in a simple package. The fact that negative signaling through a pathway involving Delta, Notch, and Scabrous seems able to dominate any quantity of hedgehog-mediated positive signaling justifies a non-competitive model for the interaction of these signals (1,3). Thus:

$$g_{m_h,m_u}\left(\tfrac{h}{H},\tfrac{u}{U}\right)=\frac{\left(h/H\right)^{m_h}}{1+\left(h/H\right)^{m_h}}\left(\frac{1}{1+\left(u/U\right)^{m_u}}\right) \qquad \textbf{(3)}$$

The remaining model parameters (H, U, m_h, and m_u) are thus defined as the scales of (respectively) activation and repression, and the associated Hill coefficients.

In a regular 1D grid with nearest-neighbor interactions, the system reduces to a tridiagonal system of ODEs where the spatial variable x indexes cells by their location in the grid. Writing down the full model gives the following test system, which we use for the remainder of the studies in this chapter.

$$\frac{\partial a_x}{\partial t} = \left(\frac{a_x^{n_a}}{a_x^{n_a} + A_a^{n_a}} \right) - a_x + G \left(\frac{\left(\frac{h_x}{H}\right)^{m_h}}{\left(\frac{h_x}{H}\right)^{m_h} + 1} \right) \left(\frac{1}{\left(\frac{u_x}{U}\right)^{m_u} + 1} \right)$$

$$\tau_h \frac{\partial h_x}{\partial t} = \left(\frac{a_x^{n_h}}{a_x^{n_h} + A_h^{n_h}} \right) - h_x + D_h \left(h_{x+1} - 2h_x + h_{x-1} \right) \quad \textbf{(4)}$$

$$\tau_u \frac{\partial u_x}{\partial t} = \left(\frac{a_x^{n_u}}{a_x^{n_u} + A_u^{n_u}} \right) - u_x + D_u \left(u_{x+1} - 2u_x + u_{x-1} \right)$$

The main goal of this work was examining the relationship between a propagating front of activity and a patterning subsystem subject to its influence, and much less the specific dynamics of a local inhibitor, which are quite simple. For this reason, and to simplify computation and analysis, we consider here only the limit $\tau_u \to 0$. This reduces the order of the dynamical system from *3N* to $2N$ and introduces N algebraic constraints. That the equations for *u* are linear and non-singular makes this a trivial change. What it does is enforce the rapidity of *u* production and diffusion relative to *a*, so *a* can be regarded as having a local effect which may be activating or inhibitory, and a non-local effect that is always inhibitory. It further prohibits cell-autonomous oscillations that could be spawned from the relaxation-oscillator-like structure of the activator-inhibitor system. Since another model system of periodic pattern formation is defined by the action of an oscillator, this is pertinent (108).

Cell-Autonomous Behavior

Since the model consists of coupled ODEs on a lattice, we can ask about the behavior of a single, isolated cell or lattice site, and separate the influences of cell-autonomous and non-autonomous interactions. Towards this end, the amount of u at any

cell in an infinite 1D grid with zero boundary conditions at $x = \pm\infty$ due to a single cell with activity f at $x=0$, satisfies the relation:

$$\begin{aligned} 0 &= f\delta_x - u_x + D_u\left(u_{x-1} - 2u_x + u_{x+1}\right) \\ u_{\pm\infty} &= 0 \end{aligned} \qquad \textbf{(5)}$$

The steady state solution is elementary and is given by:

$$\begin{aligned} u_x &= c_0\lambda^{|x|} \\ \lambda &= \frac{1+2D_u - \sqrt{1+4D_u}}{2D_u} \\ c_0 &= f\cdot\frac{-1+\sqrt{1+4D_u}}{1+4D_u - \sqrt{1+4D_u}} \end{aligned} \qquad \textbf{(6)}$$

The quantity c_0 is the contribution of a cell producing u to the local amount of that substance at the same cell. Clearly, if D_u approaches zero, nothing diffuses, all of the u remains local, and $c_0 \to f$. Conversely, if D_u is large, most of the substance diffuses away, and its local influence tends to zero. Regarding the two model diffusion constants, it is clear that we are mainly interested in D_u near the first extreme, and D_h near the second. Examining a single cell, then, we must separately consider local and exogenous u, whereas h is mainly exogenous.

Figure 10: Single cell stability and dynamics. A) the *a* dynamics of an isolated cell with $h=0$ *or* $u=\infty$. At low A_a bistability exists with no external activation. At high A_a there is no bistability. At intermediate values bistability can exist for some amount of external activation. B) the steady states of *a* versus the (constant) activity of *h* and *u*. C) the nullclines representing *a*'s relationship to *h* absent any externally generated *u*. The inhibition present is from the local *u* production due to finite *a*. This distinction has no analogue in continuous systems, but is important in determining the stalling of certain cases in the discrete case, illustrated as the nullclines for decreasing A_u eventually make the high steady state completely inaccessible to nodes starting from $a=0$ and subject to finite *h*. D-E) show how the dynamics of *a* and *h* change with their relative timescales. The most long-dashed line in each image represents the case in which *a* is characteristically much faster than *h*, while the other lines represent increasing departures from this limit. F) The difference between the slowest and the fastest trajectories for *a* to reach its high steady state. In the case where $g(h,u)$ changes slowly, the time to high steady state can be dominated by the time for *h* to change. In the case where g(h,u) is fast, the intrinsic dynamics of *a*, as well as the dynamics of its response to the other two elements becomes the determining factor. G) shows the response of the nullclines for $\partial_t a=0$ with well behaved (i.e. not early) local *u* production to increasing amounts of externally generated *u* (u_{ns}). The bifurcation value which represents loss of the low (stable) and middle (unstable) steady states proceeds from an unperturbed value, through higher values, to values that are unattainable with finite *h*. H) shows the dynamics for *a* with no external inhibition and various fixed activations. The effect of autoinhibition means that there is a minimum amount of time between activation and the production of enough *u* to inhibit adjacent cells that is independent of *h*.

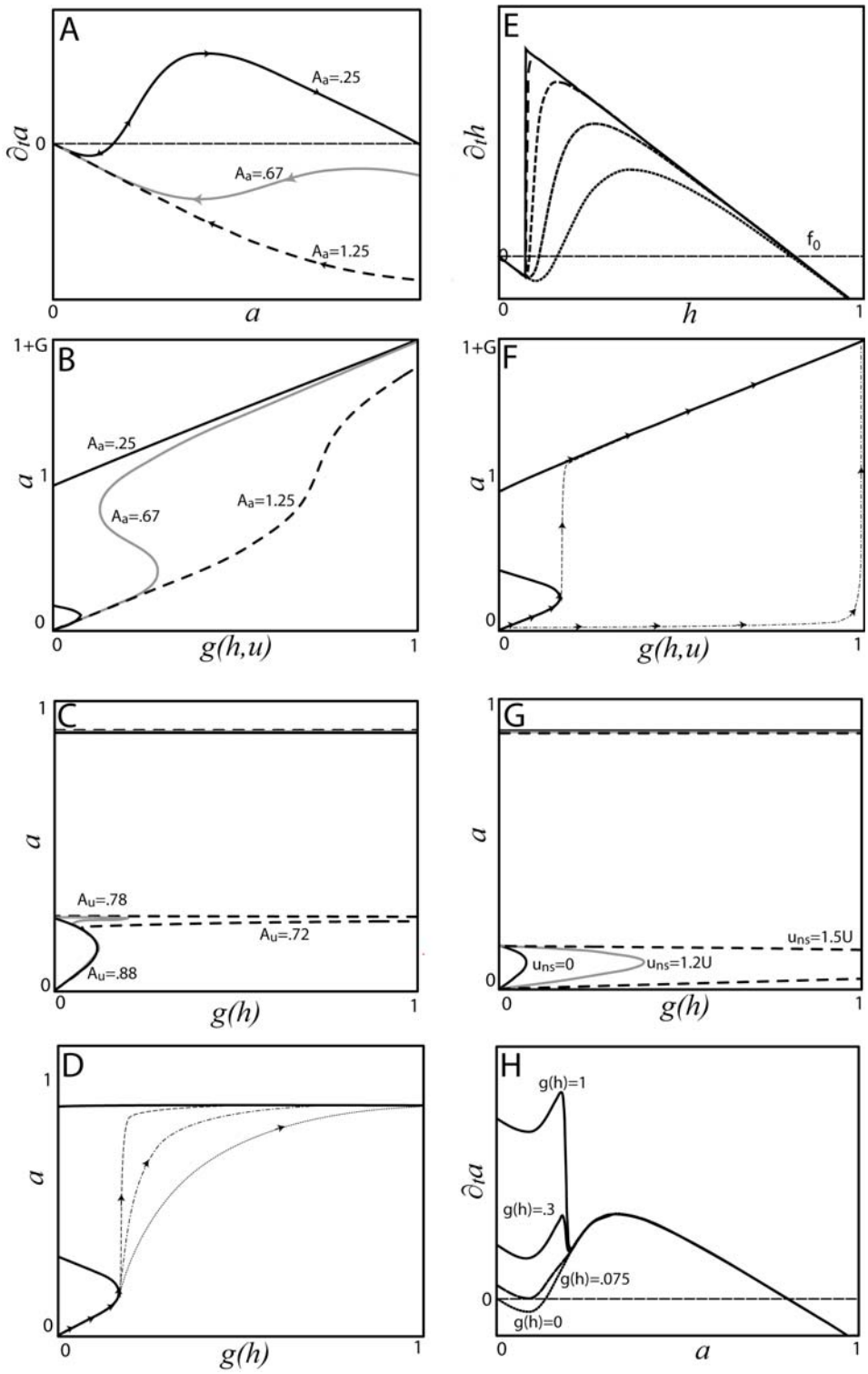
A
A_a=.25
A_a=.67
A_a=1.25
$\partial_t a$
0
a
E
$\partial_t h$
f_0
h
1+G
B
A_a=.25
A_a=.67
A_a=1.25
g(h,u)
F
C
A_u=.78
A_u=.72
A_u=.88
g(h)
G
u_{ns}=1.5U
u_{ns}=0
u_{ns}=1.2U
D
H
g(h)=1
g(h)=.3
g(h)=.075
g(h)=0

Neglecting autoinhibition, the amount of a at a node can be bistable through autoactivation (112). Here, we focus primarily on the case where cells starting at low a can switch to high a or not, but a cell with high a cannot go back down. Increased h can flip a cell to high *a* as long as abundant u does not inhibit this action; The low steady state collides with the unstable saddle in a saddle-node bifurcation. For this change to be irreversible, the complementary bifurcation (the one which would lead to the disappearance of the high steady state with decreasing h) must not be accessible, even at maximal inhibition or zero activation ($u \gg U$, or $h = 0$). These cases are illustrated in Figure 10(A-C). Restricting the bistable switch in this way prevents the transient formation of a high-amplitude pattern. Restrictions on A_a sufficient for the existence of bistability for some non-negative value of $g(h,u)$, and bistability at $g(h,u) = 0$ are, respectively,

$$A_a < \frac{1}{4}\left(\frac{n_a^2 - 1}{n_a}\right)\left(\frac{n_a + 1}{n_a - 1}\right)^{1/n_a} \qquad \textbf{(7)}$$
$$n_a > 1$$

and

$$A_a < \frac{(n_a - 1)^{\frac{n_a - 1}{n_a}}}{n_a} \qquad \textbf{(8)}$$
$$n_a > 1$$

Evaluated for $n_a = 4$, these require A_a<1.065 for bistability and A_a<.569 for irreversible bistability. As mentioned, the more stringent requirement is of primary interest for this study.

The next step in treating a single cell is to include the u that was produced locally, which we call the self-*u*. With $\tau_u=0$, a cell with activator concentration a creates a u concentration c_0 locally, as given by equation (6). Below, we have introduced the variable u_{ns} (meaning *u*-non-self) to represent inhibitor produced elsewhere that has diffused to the current location:

$$\partial_t a = \frac{a^{n_a}}{A_a^{n_a} + a^{n_a}} - a + G \cdot g(h)\left[1 + \left(\frac{u_{ns} + c_o\left(\frac{a^{n_u}}{A_u^{n_u} + a^{n_u}}\right)}{U}\right)^{m_u}\right]^{-1} \qquad \textbf{(9)}$$

The equation is now far too complicated to solve exactly for a, but it is still easy to understand the qualitative form of bifurcation diagrams. Figure 10(D-G) illustrate the behavior of an isolated cell with autoinhibition. If A_u or U is too small, autoinhibition will be strong enough to completely abolish the lower saddle-node bifurcation, and a cell that is initially in the low state will remain there forever. Similarly, but physically more interesting, since it depends on a non-autonomous quantity, enough u_{ns} can make the high steady state completely inaccessible from the low steady state. For typical parameter values, the high steady state itself is nearly invariant over the range of h because autoinhibition effectively blocks all activation through the 3' enhancer.

The dynamics by which a cell can make the traverse from low to high steady state is also readily understood. The clearest feature of Figure 10(H) is that there is a region of a dynamics where a is high enough to cause significant autoinhibition, and its approach to the high steady state is nearly independent of *g(h)*. In this range it is governed almost exclusively by its intrinsic autoactivation timescale. The region of a dynamics

dependent on h shows the potential for a bottleneck if *g(h)* exceeds the bifurcation value very slowly. If a cell is stuck in this bottleneck, it is still susceptible to repression by u_{ns}. This is rarely realized in a 1D system, in which a front propagating with velocity v produces an effective delay of order $1/v$ between adjacent cells, but is potentially important in 2D, where no delay need exist for cells adjacent in the direction perpendicular to the direction of front propagation.

Figure 10(E) takes the final step that makes sense for an isolated cell, and examines h as a dynamical variable. The overall rate of h production is attenuated by a factor of τ_h, and complicated by its diffusive dynamics, but some qualitative aspects of its isolated-cell behavior are illuminating. The production of h is wholly dependent on a, and its behavior is best understood in relation to the limit where h dynamics is very slow, and a can be regarded as quasi-static. Under these conditions, subject to monotonically increasing h, with a starting at zero, there is a discontinuity in $\frac{\partial h}{\partial t}$, and for appropriate choice of parameters the production of h looks bistable in its own right (much as a does). This apparent bistability is preserved for any monotonically increasing trajectory of externally generated h, as long as it exists for quasi-static a.

Propagating Solutions

Inspired by the behavior observed in fly imaginal discs, we are interested in the properties of asymptotically propagating solutions to equation (4) that produce a regular pattern of isolated active cells separated by an integral number of inactive cells (one-up-integer-down patterning or OUID). In examining potential propagating, patterning solutions to these equations, there are really two distinct processes, which are wrapped up

with each other to some degree. The first is a templating process by which lateral inhibition selects a pattern; the second is the process by which the pattern is pushed forward by the action of h. Given an assumption for the templating, namely the end pattern and the rate at which it is produced, we can calculate h at any point. Similarly, given assumptions about a propagating h field, we can deduce the pattern produced. What remains is finding self-consistent solutions where the h produced by a pattern of activated cells interacts with the template produced by those cells such that the original pattern is extended. A solution of this sort, if stable, may be considered an asymptotic pattern-forming limit of the model, which, given appropriate initial conditions, will make a regular pattern behind a wave of activation as it proceeds across a grid.

The h *field due to a periodic pattern*

Above, we quoted the steady-state distribution due to a point-source of a substance diffusing on a 1D lattice (equation (6)). To deal with the dynamics of the propagating h front, we need more detailed information. We would like to solve the problem:

$$\begin{aligned} &\partial_t h_x = f_x(t) - h_x + D_h\left(h_{x-1} - 2h_x + h_{x+1}\right) \\ &f_n(t) = f\left(vt - x\right)\delta_{x,q\cdot j} \\ &j \in \mathbb{Z} \end{aligned} \qquad \textbf{(10)}$$

Here *f(t)* is the stereotyped dynamics of a cell being activated, and the Kronecker delta is required to enforce a pattern of activation with integer period *q* (*j* runs over all integers). In wildtype flies, it appears that the activation intrinsic to a single cell happens on a considerably faster time scale than the overall propagation of the MF from column to column of activated cells (1-3). In this limit ($\tau_h \gg 1$), $\frac{\partial h}{\partial t}$ sees its source term due to

a/A_h jump from a value nearly zero (for appropriate parameters) to a value determined by the high steady state of a, which I will call f_0. The explicit time dependence of f then becomes:

$$f_x(t) = f_0\Theta(vt - x)\delta_{x,q\cdot j} \quad \textbf{(11)}$$

The impulse-response of the differential equation system is known exactly, and the general solution is the sum over all cells of an integral over time, where the integrand is the product of the source strength and an exponentially modulated associated Bessel function of the 1st kind, I.

$$h_x(t) = \sum_{x'=-\infty}^{\infty} \int_{-\infty}^{t} f_{x'}(t') e^{-(t-t')-2D_h(t-t')} I_{|x-x'|}\left(2D_h(t-t')\right) dt' \quad \textbf{(12)}$$

Applying the idealized form of f from equation (11) leads to the simplified form:

$$h_x(t) = f_0 \sum_{x'<vt, x'=q\cdot j} \int_{0}^{t-x'/v} e^{-(1+2D_h)t'} I_{|x-x'|}\left(2D_h t'\right) dt' \quad \textbf{(13)}$$

To better understand this expression, it helps to look at the analogous continuum problem, where the source term is not patterned, namely:

$$\partial_t h(x,t) = f_0\Theta(vt - x) - h + D_h \partial_{x,x} h \quad \textbf{(14)}$$

This problem can be solved exactly by transforming into a reference frame moving at a velocity, v. Applying appropriate boundary conditions yields the following result:

$$h(x,t) = f_0 \begin{cases} 1 - \left(\frac{v+c_1}{2c_1}\right) e^{\frac{-v+c_1}{2D_h}(x-vt)}, x < vt \\ \left(\frac{-v+c_1}{2c_1}\right) e^{\frac{-v-c_1}{2D_h}(x-vt)}, x \geq vt \end{cases} \quad \textbf{(15)}$$

$$c_1 = \sqrt{v^2 + 4D_h}$$

The amount of h at $x=vt$, the point where h production has just been activated, decreases monotonically as v increases , and knowing the critical value of h for activation and the source strength (f_0, related to the pattern density) uniquely determines the velocity parameter v, which was previously arbitrary. Recall that the value of h that triggers local h production is largely determined by the easily-characterized slow-h limit.

If one attempts to treat a continuum system with a spatially periodic source term, static in the lab frame, by transforming into a moving reference frame, a point at constant $z = x - vt$ does not approach a steady state for any $v \neq 0$, but instead approaches a limit cycle with average h given by equation (15). The amplitude of the deviations of h from the ideal, unpatterned case will be relatively small if the largest spatial scale of the source pattern is small compared to the smallest spatial scale in the propagating front. This spatial scale is equal to $\sqrt{D_h}$ at $v = 0$, which remains a good estimate for most parameter sets as typically $D_h \gg \tau_h^2 v^2$. For the reference parameter value $D_h = 640$, $\sqrt{D_h} \approx 25.3$ and patterns with period 5 (this is the scale that the fly eye discs leads us to be most interested in) are effectively averaged over. See Appendix B for a more detailed discussion of the limit-cycle amplitude problem.

Significant work has been done on the discrete version of this problem, though never with a patterned template (101,113-118). The basic result we rely on, here, is that any deviations from the continuum behavior tend to become inconsequential for $\sqrt{D_h} \gg 1$. This makes sense, since the real difference between the continuous and discrete systems is related to how well the discrete difference operator approximates the continuum point derivative. To the degree that these conditions hold, it makes sense to treat *h* as a uniformly translating front, sampled at intervals, the fundamental form of which can be approximated easily by the related continuum case, as above, giving us a jumping off point for treating the template (and thus the source-density) problem.

Template Formation in 1D

So far we have assumed the existence of a large-amplitude pattern that extends itself in space and time indefinitely. We have reason to believe that the activating influence due to a forming pattern propagates uniformly in space and time, and that the dynamics of individual cells are faster than the overall dynamics of propagation. With u slaved to a, the total u concentration at point x follows directly from equation (6):

$$\begin{aligned} u_x &= \sum_{x'} c_{0,x'} \lambda^{|x-x'|} \\ \lambda &= \frac{1+2D_u - \sqrt{1+4D_u}}{2D_u} \\ c_{0,x'} &= \left(\frac{a_{x'}^{n_u}}{A_u^{n_u} + a_{x'}^{n_u}} \right) \cdot \frac{-1+\sqrt{1+4D_u}}{1+4D_u - \sqrt{1+4D_u}} \end{aligned} \qquad \textbf{(16)}$$

For any point in advance of a regularly patterned half-space of identical activated cells, u_x is a geometric series that converges increasingly rapidly for small D_u. For a simple pattern where isolated active points are arranged with a period q, so that active

points are located at $x' = 0, -q, -2q, -3q...$, and the u production at all of these active points is identical (as predicted by their cell-autonomous behavior) the expression for u at $x \geq 0$ is:

$$u_x = c_0 \frac{\lambda^x}{1-\lambda^q} \qquad \textbf{(17)}$$

In the section on cell-autonomous behavior, we noted that there is, in general, an amount of exogenous u (call it $u_{threshold}$) that can absolutely prevent a from leaving the low steady state, regardless of h. Suppose that the role of the template in this model is simply to put some cells above this threshold, so that when the h front progresses (slowly and uniformly) the next cell to be activated is just the first one it encounters with $u_x < u_{threshold}$. A self-extending pattern in these conditions is subject to two inequalities that ensure the next cell to be activated is spaced a distance q from the previous cell, and that this is the same as the period of the existing pattern:

$$c_0 \frac{\lambda^q}{1-\lambda^q} < u_{threshold} < c_0 \frac{\lambda^{q-1}}{1-\lambda^q} \qquad \textbf{(18)}$$

For given constants c_0, λ, and $u_{threshold}$, there is no more than one integer q that satisfies these conditions. We understand the physical meaning of these two cases (integer solution exists or does not) in terms of a one-dimensional map that gives u in each newly activated cell in terms of the value of u in the previous activated cell.

Let the previously activated cell be located at $x = 0$ with inhibitor concentration $\hat{u}_m$ immediately after activation, and the newly activated cell have inhibitor concentration $\hat{u}_{m+1}$ immediately after its own activation. If this cell is at spatial position $x' > 0$, then

since the u produced at all preceding cells is decaying with the same spatial dependence, the following map of $\hat{u}_m$ onto $\hat{u}_{m+1}$ relates these, where c_0 accounts for the inhibitor produced by the newly activated cell, itself.

$$\hat{u}_{m+1} = \hat{u}_m \lambda^{x'} + c_0 \qquad \textbf{(19)}$$

For the cell at c_0 to indeed be the next one activated, the pre-activation u, $\hat{u}_m \lambda^{x'}$, must satisfy equation (18). The graph of $\hat{u}_{m+1}$ versus $\hat{u}_m$ is the union of the curves for different x' that obey these inequalities, and is thus piecewise linear and discontinuous. All the linear segments have positive slope less than one (since $\lambda < 1$), and the discontinuities are such that all the segments with $x' > 1$ lie within a finite band of allowed $\hat{u}_{m+1}$. Illustrations of these maps are shown in figure 4. This kind of map has been described by Jain and Banerjee (119). Their results discuss what happens if the identity line, important for describing the asymptotic behavior of the map, passes 1) through a line segment, such that there is one point of intersection (one integer solution to equation (18) with $\hat{u}_{m+1} = \hat{u}_m$) or 2) through a discontinuity between two line segments (no integer solutions to equation (18) with $\hat{u}_{m+1} = \hat{u}_m$). The structure encountered in going from a model of the first type to the second is a discontinuous border collision bifurcation. At such a bifurcation, where there was once a single, stable, period-1 solution to the map, one enters a regime with stable high-period solutions. See Figure 12 for an illustration of a case with a period-4 solution. These solutions reach arbitrarily high periods, and are arranged in parameter space in a complex fractal geometry (119). This means that if one varies parameters continuously in such a way as to go from a stable period n to a period *n+1* pattern (both of which exist), one must pass through a

region characterized by high-period asymptotic solutions with each period consisting of several cells separated by n and $n+1$ units in some combination. Notably, in this simplified picture (call it step-function-h) the patterning solution is globally attractive given any initial prepattern, and is unique up to an overall translation.

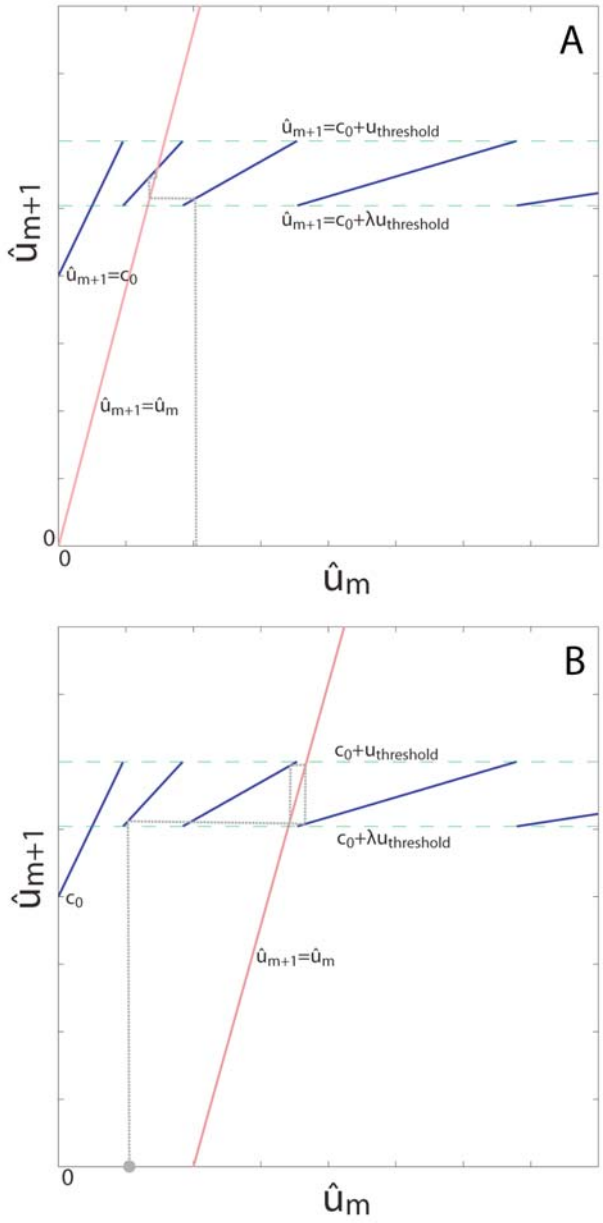

Figure 11: 1D map relating *u* at a newly patterned point immediately after its activation to the amount of *u* at the previous activated point. The blue lines represent the map function, as given by equation (19). The top dashed green line represents the maximum amount of *u* that still permits cell activation. The lower dashed green line represents the minimum amount of *u* at a point that also implies its neighboring point cannot be activated. In A, the identity line (in red) intersects the fourth line segment of the map function, implying the existence a single, stable 1-up-3-down pattern. In B, the identity goes through a discontinuity, so that asymptotically the pattern will alternately have gaps between active points of 2 or 3 cells.

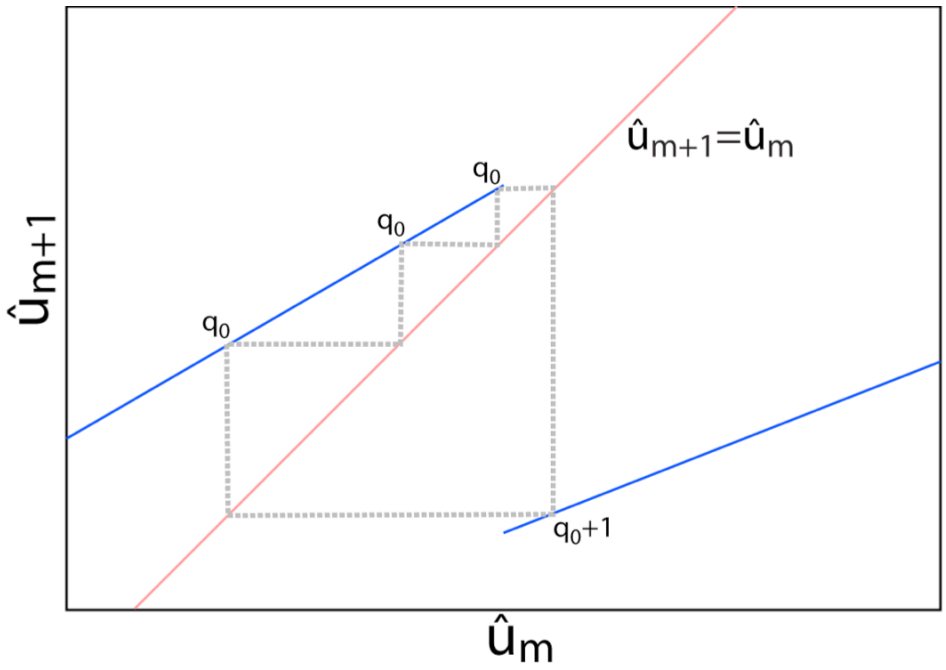

Figure 12: A detail of a higher-period solution to the pattern template solution. In this case, the overall period is $4q_0+1$. The system never becomes chaotic in this limit, because the map function always has slope <1, and is not stretching.

These results can be generalized for significantly relaxed assumptions. In the original model of equations (4), h is smoothly varying (whereas in the preceding paragraphs we have taken it to be a step function in space); also the effect of u is not necessarily negligible for $u < u_{threshold}$. To address the second concern first, in general, there is a critical value of h, $h_{crit}(u)$, that reflects the bifurcation value where the low steady state of a disappears. We chose $u_{threshold}$ in the previous analysis so that $\lim_{u \to u_{threshold}} h_{crit}(u) = \infty$. More generally, $h_{crit}(u_x)$ decreases monotonically as a function of increasing x toward a finite, positive limiting value. Additionally, its second derivative in space (discretely approximated, of course) is always positive. These are general characteristics of h_{crit} as determined by the functional form of u in the model.

To start dealing with the continuous variability of h, and its spatial structure, let's approximate the advancing front of activation with a linear function of $z = x - vt$ restricted to positive numbers, and with slope $-c_3$.

$$h = \max\left[-c_3 z, 0\right] \qquad \textbf{(20)}$$

As before, assume that there is a semi-infinite regular pattern on $x \le 0$ and ask where the next cell is activated. As t increases, the first cell where h exceeds h_{crit} is, again, governed by two inequalities.

$$h_{crit,x'+1} - h_{crit,x'} < c_3 < h_{crit,x'} - h_{crit,x'-1} \qquad \textbf{(21)}$$

These are exactly analogous to the inequalities for u described above, and they determine the locations of the discontinuities in the map of $\hat{u}_m$ onto $\hat{u}_{m+1}$. The existence

of solutions and their globally attractive nature is preserved. Indeed, the structure of the map and the solutions is nearly guaranteed for uniformly translating fronts and inhibitor decaying exponentially in space. For further development on this theme see Appendix C.

Self-consistent solutions

Armed with these ideas for understanding front propagation and pattern templating, we sought solutions to the full model where the *h* front created by a pattern interacts with the template in such as way as to extend the same pattern indefinitely. We expected that, to the degree the idealizing assumptions were accurate, these predicted solutions would match the solutions observed by integrating the full model (equation (4)) with appropriate initial conditions. In addition to the parameters in the basic model, we must specify two "new" free parameters, front velocity and pattern density, which determine the character of the self-consistent solution.

It makes sense to treat front velocity as a continuous variable. Pattern density, that is, the fraction of cells in a regular pattern with high *a* is more restricted. For OUID patterns, it is the inverse of an integer. For a fixed value of pattern/source density in the continuum limit (f_0 in equation (14)), the value of *h* at the cusp of the front, *z=0*, is a simple, monotonic function of velocity. If we have other information that dictates this h concentration, we can solve for the velocity; in this case we set it equal to the critical value, h_{crit}, needed to flip the bistable switch.

The discreteness of the system and the non-uniform pattern complicate this formulation only slightly. With the spatial pattern enforced arbitrarily, self-consistency demands that the *h* at a certain (pattern-extending) point reach the triggering value at a

certain time, allowing one parameter (the velocity v_n appropriate to a specific pattern density, $1/n$) to be varied to meet this requirement.

$$v_n = \underset{v \geq 0}{\arg}\left[h_0(0) = h_{crit} = h_n(\eta/v) \right] \qquad \textbf{(22)}$$

This is a 1D root-finding problem of a monotonic function in a semi-infinite domain: As long as a solution exists, it is easy to find by standard techniques. In the continuum, h is capable of producing a moving front as long as $h_{crit} < 1/2$. As detailed by Elmer, this is not the case in a discrete system, and propagation can fail at much lower h_{crit} (121). Indeed, this propagation failure is a key prediction of our model. Since the amount of h due to a static pattern increases monotonically with time to its steady state, the sufficient condition for the existence of a self-consistent velocity for a spacing of individual active cells, q, is that the steady state h due to a semi-infinite pattern exceed the critical value of activation at the next-to-be-activated point:

$$\begin{aligned} & v_q \in \mathbb{R} > 0 \\ & \Leftrightarrow \\ & h_q(\infty) > h_{crit} \end{aligned} \qquad \textbf{(23)}$$

Lower pattern densities obviously produce lower equilibrium values of h at all cells. Since h_{crit} decreases to a finite limit as $u \to 0$, there is always a minimum pattern density, $1/q_0$, that can be considered a candidate for a self-consistent period-q solution with single active cells. Self-consistent velocities exist for all $1 \leq q \leq q_0$. We choose among these options by requiring that the next cell to become activated is always the first one triggered by the previous pattern, a formulation of the fast-a assumption. The idea,

here, is that the first cell triggered will quickly become activated and suppress its near neighbors. This requirement is applied quantitatively by asking, for any given pattern expanding at its self-consistent rate, whether, at the moment of activation of the appropriate next cell, h at any other cell is greater than that cell's h_{crit}. This question should be asked for every potential value of q. It is possible to have models where the number of self-consistent patterns is 0, 1, or more than one. Cases with one self-consistent solution and no self-consistent solutions correspond, respectively, to the cases discussed in the section on templating with single period-1 solutions or only high-period solutions. Models with more than a single self-consistent solution correspond to cases where the change in the *shape* of the propagating h front due to a change in the pattern density is enough to substantially change how h interacts with the inhibitor template. We have not been able to generalize about this case very much, except to say that cases with two solutions are rare and require very careful choice of parameters. To get more than two solutions seems to require the careful choice of more complicated functional forms with more free parameters. This mechanism is clearly different than that of a pattern propagating into a linearly unstable field of cells, a case which has been treated (122).

Parameter Scan

In order to test the analytic approach and to gain a fuller understanding of the model, we conducted a random parameter search in a region of parameter space known to contain at least some solutions that yielded behavior of interest. For the purposes of this scan we varied the concentration parameters A_a, A_h, A_u, U and H; the operator-strength parameter, G; the diffusion constant parameters, D_u and D_h; the Hill coefficient m_h; and the time-scale separation constant τ_h. We centered the parameter search on a parameter

set, p_{ref}, we knew to give results in 2D similar in appearance to the patterning observed in actual developing fly eyes.

$$p_{ref} = \begin{cases} A_a = .25 \\ G = 3.475 \\ H = .0193 \\ m_h = 8 \\ U = .00001048 \\ \tau_h = 371.65 \\ A_h = .75 \\ D_h = 640 \\ A_u = .9 \\ D_u = .16 \end{cases} \quad \textbf{(24)}$$

We did not vary the Hill coefficients for the actions of a and u. These are summarized in p_{static}.

$$p_{static} = \begin{cases} n_a = 4 \\ n_u = 8 \\ n_h = 4 \\ m_u = 8 \end{cases} \quad \textbf{(25)}$$

In scanning the parameter space, we sampled the parameters over a large range using pseudo-random numbers, made analytic predictions for the model defined by each parameter set, and examined the results of integrating that model directly. The limits of the sampled interval and the associated distribution used for each parameter are summarized in Table 1. We generated and tested 640,000 independent sets of parameters according to these rules.

Parameter	Min/p_{ref}	Max/p_{ref}	Distribution
A_a	.01	10	Log
G	.01	100	Log
H	.01	100	Log
m_h	.0625	1.25	Uniform
U	.01	100	Log
τ_h	.01	10	Log
A_h	.01	5	Log
D_h	.01	100	Log
A_u	.01	5	Log
D_u	.01	100	Log

Table I: Scanned parameters and ranges. Each model parameter was varied independently over a finite range using random numbers. The minimum and maximum values were set by the indicated ratios with the reference parameter set. For most parameters, the distribution that was sampled was $p\left(\ln\left[\text{parameter}/p_{ref}\right]\right) \propto c$, the distribution identified in the table as "Log." The parameter m_h was sampled uniformly over its range.

The sampling limits for this work are necessarily a bit arbitrary; we took our target to be two orders of magnitude up and down from each reference value. This limit did not make sense for the variables, A_a, A_u, and A_h, as the model does little of interest if they exceed the high steady state of a. We limited the maximum value of τ_h for the practical reason that this plays a very direct role in how long an equation system must be integrated to examine its asymptotic behavior. That asymptotic behavior is expected to become independent of τ_h (up to an overall rescaling of time) for large enough τ_h. The range used is large enough to capture this limit. Varying the Hill coefficient, m_h, is significantly different than varying the other parameters, in that it does not have an obvious ratio-metric interpretation. Values of $m_h > 1$ represent sigmoidal curves for activation by h, whereas values of $m_h \leq 1$ represent the qualitatively different case where activation is most sensitive to changes in h at $h = 0$.

We subjected every parameter set to the analyses described in Appendix A, and, dictated by the analytic understanding we've outlined, predicted whether we expect a patterning solution to exist, and what its speed and period should be if one does. We integrated models defined by each parameter set on a 1D grid using arbitrary, randomized initial conditions, as well as initial conditions specifically meant to mimic the predicted asymptotic pattern-forming attractor. Using an automated pattern detection scheme, we compared the results of each integration both qualitatively and quantitatively to the predictions arrived at analytically.

Analyzing Patterns

The first, qualitative, stage of looking at patterns involved classifying parameter sets amongst 5 basic types of behavior: Patterning (Figure 9(A)), stalled (Figure 9(B)), poorly-patterning, non-patterning (Figure 9(C)), and impermanent fronts. The first two cases, where a solution consisting of a self-extending periodic pattern of isolated active cells exists (or does not) are addressed by our theory, and we expect predictions of behavior, period, and timing to be accurate in the limit that a dynamics are much faster than h. The other cases are categories of behavior we observed in the course of running simulations that are not explained in detail by our theory, and represent the failure of our assumptions. Briefly, a poorly-patterning front consists of a solution in which an initial pattern leads to a propagating front resulting in some active cells and some inactive cells, but without these cells conforming to a periodic solution with isolated active cells. Non-patterning fronts exist when an initial pattern leads to a propagating solution where all the cells become active. Some instances of this behavior can be blamed on trivial inhibition: when a cell is incapable of fully inhibiting its neighbors. In this case it is still subject to our theoretical predictions. For our purposes, we consider non-patterning fronts to be solutions that show this behavior *despite* predictions to the contrary. Impermanent fronts are any solutions in which a cell once determined to be active becomes inactive again at a later time. Such solutions would violate a very fundamental aspect of our theoretical understanding of the system, namely the irreversibility of activation.

It was our hope that the parameter sets showing behavior not predicted analytically would clearly be the result of the failure of one of the assumptions made explicitly in our analysis, namely the separation of timescales between a and h dynamics, and the irreversibility of a activation. In discussing patterns, we refer strictly

to large-amplitude, long-lived patterns of a, as these are the characteristics of the biological system that we are modeling.

Results

Qualitative results

The results of our parameter scan were entirely consistent with the predictions made by techniques based on the analysis of the preceding section; behaviors we did not explore analytically began to appear only when the assumptions behind the analytics no longer held. The most interesting assumption, both because of the behavior observed during its failure and because its failure likely represents real-world conditions of interest, is the large separation of timescales between the advance of the h front and the rise of a at a node.

Of the 640,000 parameter sets scanned, 137,235 had $A_a \geq .569$, where we anticipate that a activation can be transient. Any parameter sets in which a was transiently high, but fell back to a value near the low fixed point (an impermanent front) were in this set. Additionally, persistent activation of any sort was exceedingly rare for these parameter sets, confined to those where A_a was very close to the cutoff of .569 or u was never produced in significant amounts. Most of the parameter sets (≈95%) with the offending values of A_a can be described as stalled solutions, given reasonable initial conditions. The balance show complicated dynamic behavior.

Of the remaining 502,765 parameter sets, we predicted 241,572 (or 48%) would have no propagating solution. Of these, 208,348 (86%) were unequivocally stalled. About three-quarters of the remaining 33,224 displayed some sort of fairly well behaved propagating solution. Most of these parameter sets gave patterns that either had multiple

adjacent active cells, and/or propagated very quickly, in clear violation of the assumptions made for stably patterning solutions, and thus in predicting stalled solutions. The remainder tended to show behavior suggesting pathologies in the integration itself. We examined a subset of these pathological cases individually, pursuing them with tighter error tolerances. Subjected to this treatment, they resolved cleanly into the well-behaved classifications. We should mention that a prediction of a propagating solution does not necessarily imply that other attractors cannot exist. Indeed, there is always an attractor representing propagation failure for a sparse-enough initial pattern. Less universally, there can be an attractor representing a fast-propagating front with no patterning if the maximum source-density is high enough to push the important h dynamics faster than a. What other asymptotic solutions might exist between these two extremes, and what transients are involved in approaching them, are interesting questions, though analyzing them in this 1D system is unlikely to yield much in the way of biologically relevant information: We are mainly concerned with the well-behaved patterning solutions.

The theory predicts the other 261,192 parameters sets have some sort of propagating solution that can be understood within its framework, if the slow-h assumption holds. Of these, 89% had an easily-classified propagating solution, and about 1% appeared to be truly stalled. The remainder seemed to yield easy-to-classify behavior only when given "special treatment," i.e. integrated with tighter tolerances, for longer times, and over larger domains. For 24,213 parameter sets the predicted self-consistent pattern was a front of uniform activation (i.e. trivial inhibition). This behavior, which must be regarded separately from cases where a uniform front was observed in defiance

of expectations, was observed in 19,855 cases (82%), with the remainder showing more exotic behavior. These parameter sets, which tend to produce large amounts of activator and very fast fronts, tend to strain the assumptions of the model, but it is unclear what qualitative distinction can be drawn between slow-h and fast-h behavior. We pursued quantitative pattern analysis on those 236,932 parameter sets where there was a predicted pattern, other than uniformly high a, under the idealizing assumptions.

It should be clear that our predictions about the behavior of parameter sets are, broadly speaking, correct. In the cases of the bad predictions one should keep in mind that the parameter space search cast a very wide net. The reference parameter set is a solid, well-behaved citizen, but the parameter space explored extends past physiologically meaningful parameter regimes, deep into regimes that we now know are almost ridiculous.

Quantitative Results

We now turn our attention to the analysis of the simulation data from parameter sets where we predicted a pattern-forming propagating front. It is important to stratify these parameter sets by the degree to which they meet the assumptions of the analysis. The first assumption, and the easiest to apply, is that up-means-up and down-means-down: The production of h and u by nodes at the low steady state must be negligible, and the production of h and u at the high steady state must be non-trivial. The high steady state assumptions for h and u have already been applied since these values were needed in calculating self-consistent pattern-forming solutions. The low steady state h and u production, however, we simply assumed to be zero in the analysis. This is a good assumption for the fly system, but it was occasionally violated by randomly chosen

parameter sets. A strong low-steady-state criterion for u is that at the "point of no return," i.e. the unstable steady state of a at zero activation, the amount of u produced is less than half what would be required for that cell to completely inhibit itself. A reasonable low-steady-state requirement for h is that the equilibrium amount of h produced by an entire field of cells held at the unstable steady state is less than would be required to activate an uninhibited cell. Of the 236,926 parameter sets remaining after the previous exclusions, 151,450 simultaneously meet the high-low criteria, and thus constitute the parameter sets which test the analytic description of the model equations in detail. The specific analytic predictions we made for these sets break down as follows: 136,620 have a single propagating regularly spaced solution, 537 have multiple propagating regularly spaced solutions, and 14,293 have no period-1 self-consistent propagating solution.

76,118 (56%) of the 136,620 parameter sets predicted to have a single, attractive patterning solution made a propagating pattern with single, isolated activated points. Of these, we predicted the correct spatial period for the solution in 97.1%. This degree of agreement is striking, as shown in Figure 13, and is much better than that achieved using a simpler model in which the h front is given a square profile, which is only 62.1% accurate, and clearly systematically biased as shown in Figure 14. It remained to check whether violation of the slow-h assumption could account for the 44% of parameter sets that did not violate any of the criteria already applied but that nonetheless did not produce patterning fronts.

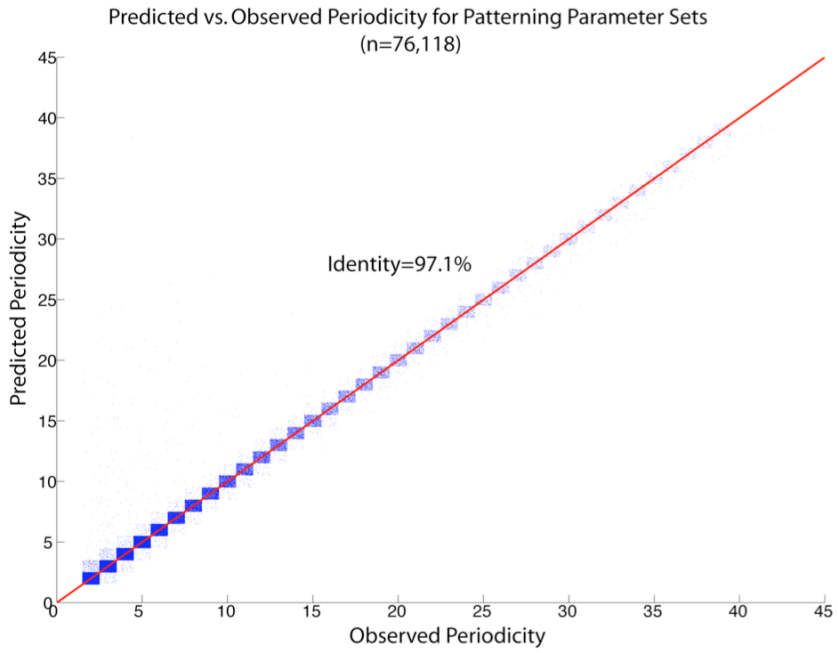

Figure 13: Observed versus predicted periodicity for parameter sets showing regular 1-up-integer-down patterns. Each blue dot represents a parameter set. The points described by a particular ordered pair ([*observed*, *predicted*], for instance [5,3]) are assigned a random location within the box describing their neighborhood to give the idea of density. As you can see, the points are very densely concentrated along the identity line. Indeed, >97% of them show perfect agreement.

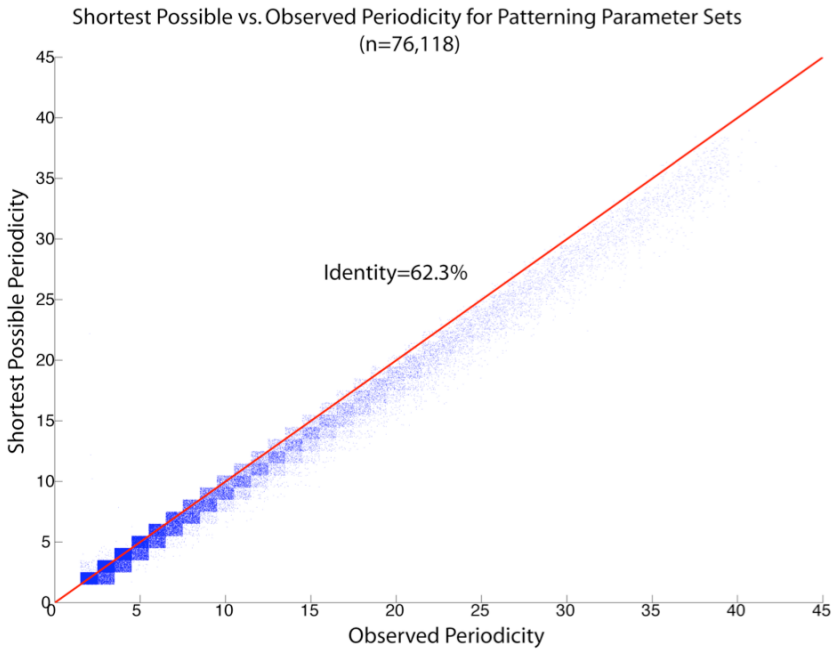

Figure 14: Null model for period prediction. The same kind of plot as in Figure 13, but using a simpler model for the interaction of the propagating activator and template. This situation is analogous to the step-function activator model. The overall correlation of prediction and observation is still clear, but there is obviously a strong bias towards predicting periods that are too short.

In general, these parameter sets yielded behavior in which multiple adjacent cells were activated in the final pattern. The actual behavior in these cases ranged from uniform propagating fronts, in which every cell was activated (recall that some of the parameter sets that were predicted to stall also showed this behavior), to complex patterns of activated cells not obeying any obvious periodicity, to regular-appearing patterns of multiple active cells separated by multiple inactive cells. While measures of the "average" expressed pattern period and spacing (in non-uniform solutions) showed significant correlation with the predictions, the absolute accuracy of the predictions was much lower than for parameters that showed basic OUID patterning. It is unclear what such observations mean given the qualitative diversity of this group.

In the classification based on parameter-space arguments so far, we have not attempted to evaluate quantitatively how well the assumption of slow h dynamics compared to a is met for different parameter sets. The specific time scales requiring comparison are: 1) the time it takes a recently activated node to reach the level of a necessary to inhibit its nearest neighbor, and 2) the time it takes the propagating front of h to progress 1 lattice site. These timescales are not independent, and evaluating them separately, without careful integration of the full model, requires further approximation. We use the self-consistently calculated average front velocity to derive timescale 2. Timescale 1 we approximate as the time it takes an isolated, uninhibited node to progress from the steady state a at bifurcation, to the level where its nearest neighbors are completely inhibited. This time has a non-trivial dependence on h dynamics, but approaches a well-defined lower limit corresponding to constant, maximal activation: $g(h)=1$. The physical assumption at work here is basically that the rise time of a node

is dominated by the time it takes the bistable switch to achieve the high state, once it has escaped outside influence *via* autoinhibition.

Plotting each parameter set on axes reflecting these two time scales shows a clear separation between the singly-activated, uniform-front, and more complicated cases, as shown in Figures 15 and 16. The quality of a binary classification is, of course, summarized in a 2-by-2 table as defined below, and we generated a linear separator in the log-log plane between the two limiting behaviors (patterning and non-patterning).

$$rule1 = \left\{ mx_{1i} + b < x_{2i} \right\}$$

	$class = 1$	$class = 2$
$rule1$	A	B
$\sim rule1$	C	D

(26)

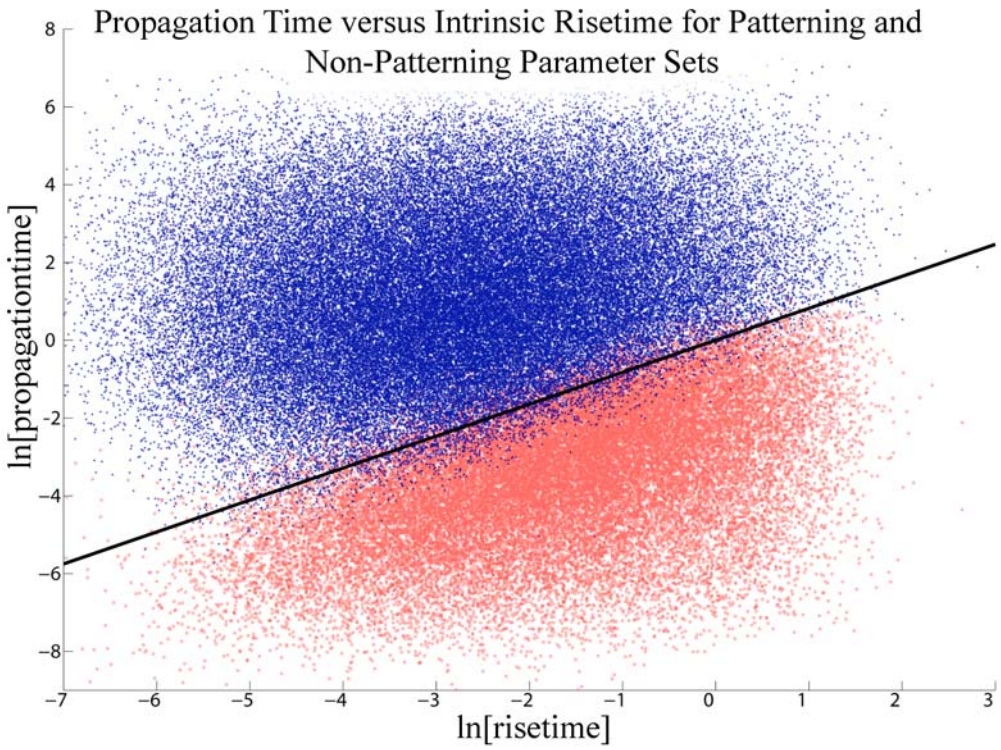

Figure 15: Timescale separation and patterning v. non-patterning behavior. Each point represents a parameter set for which pattern formation was predicted, and was either observed as predicted (dark, blue), or for which an unpatterned propagating front was observed (light, red). They are arranged on log-log axes representing (x) the shortest possible time for a cell experiencing maximum activation to reach high enough a to fully inhibit its nearest neighbor, and (y) t_0/n_0, where t_0 is the amount of time predicted between successive activations, and n_0 is the predicted period of the pattern. This approximates the amount of time it takes the average h-front to advance one lattice site. The black line is a separator generated to maximize a prediction quality statistic. It successfully classifies about 95% of these parameter sets. It is clear that the conditions that allow patterning by the mechanism we describe begin to fail as the internal dynamics of a cell can no longer be considered fast compared to front propagation. It is notable that the degree to which the timescales must be different for the behavior to be dominated by OUID patterning regardless of specific parameters is not very great.

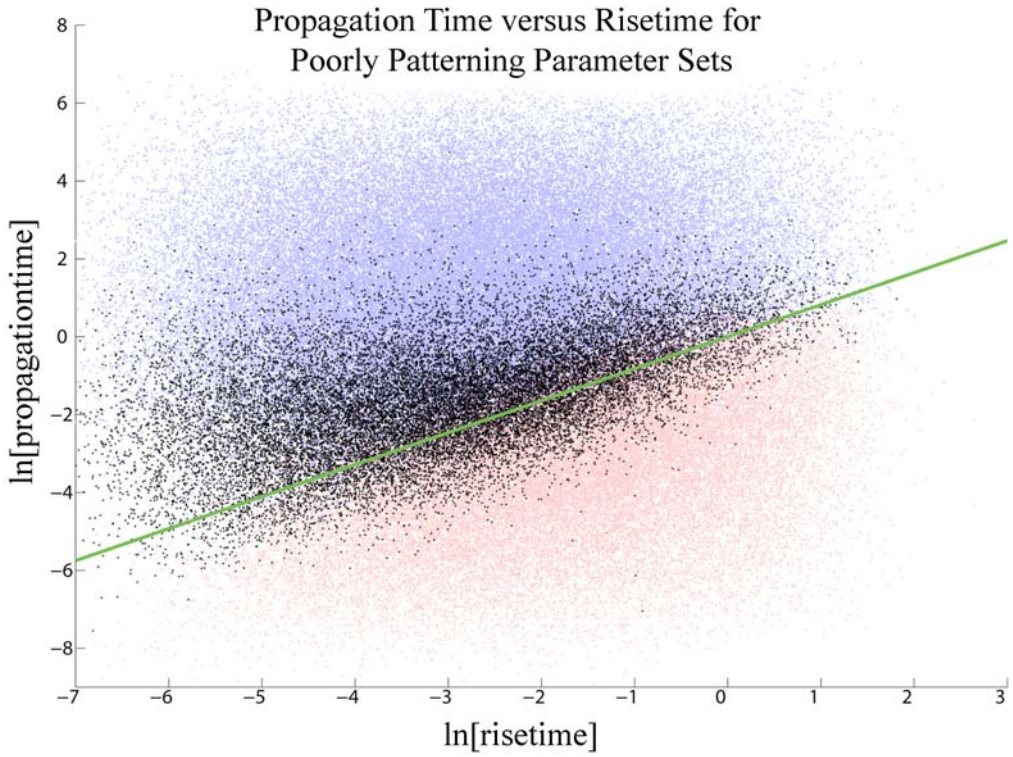

Figure 16: Timescale separation and complicated patterning behavior. The same plot as in Figure 15, but with an overlay of the points for which a pattern was predicted, but neither that pattern nor a uniform propagating front was observed. Very complicated behavior was observed in this set, and these parameter sets are particularly prone to very long transient behavior. Whether these solutions are in the process of settling down to one of the better-known behaviors (patterning or non-patterning) or are approaching other, more complicated limiting behavior is an open question. It is clear, however, that they arise between parameters that lead to patterning and those that merely propagate.

Maximizing the association between the classification and the actual class membership in terms of a statistic similar to a phi coefficient,

$$\max_{m,b}\left[\frac{A^2D^2}{(A+B)(A+C)(D+B)(D+C)}\right] \qquad \textbf{(27)}$$

but without penalizing asymmetric misclassification, yields a line where the sensitivity and specificity of classification are both in the mid-to-high 90 percents, as are the positive and negative predictive values for parameter sets randomly chosen from this distribution.

Inspection of the solutions showing patterns that do not have isolated activated nodes reveals that these are concentrated in the region of parameter space that is between the more easily classified patterns. All of this suggests that as one varies parameters in such a way that the timescale separation between a and h is reduced, one will first go from a situation where a propagating solution with isolated activated points is supported, to a region where only more complex patterns are supported, to, finally, a situation where the only propagating solution is one for which all the nodes end up activated. The exact nature of the transitional region, unlike the transitional region between patterns of different periodicity, is likely to hold very complex behaviors, and is difficult to study, in part, because of the very long transients that can be observed there. It is also likely that similar behavior can be observed in regions of parameter space with no predicted propagating solutions, as a reduction in the separation of the timescales can send the system from a state where all solutions stall to a state where rapidly propagating, poorly-patterned fronts can exist. Though some of our data applies to this case, and suggests such behavior, it remains to be studied in mechanistic detail.

The analytic theory presented here predicts not only the spatial period of a pattern, but also the front speed. We expect that the quality of these predictions should increase with longer times between the activation of nodes, since the (comparatively) invariant activation time of a single node, which our calculations effectively set to zero, will have a relatively smaller effect on the overall front speed under these conditions. For the parameter sets where we correctly predict the presence of a OUID pattern and its period, this is the case, as shown in Figure 17.

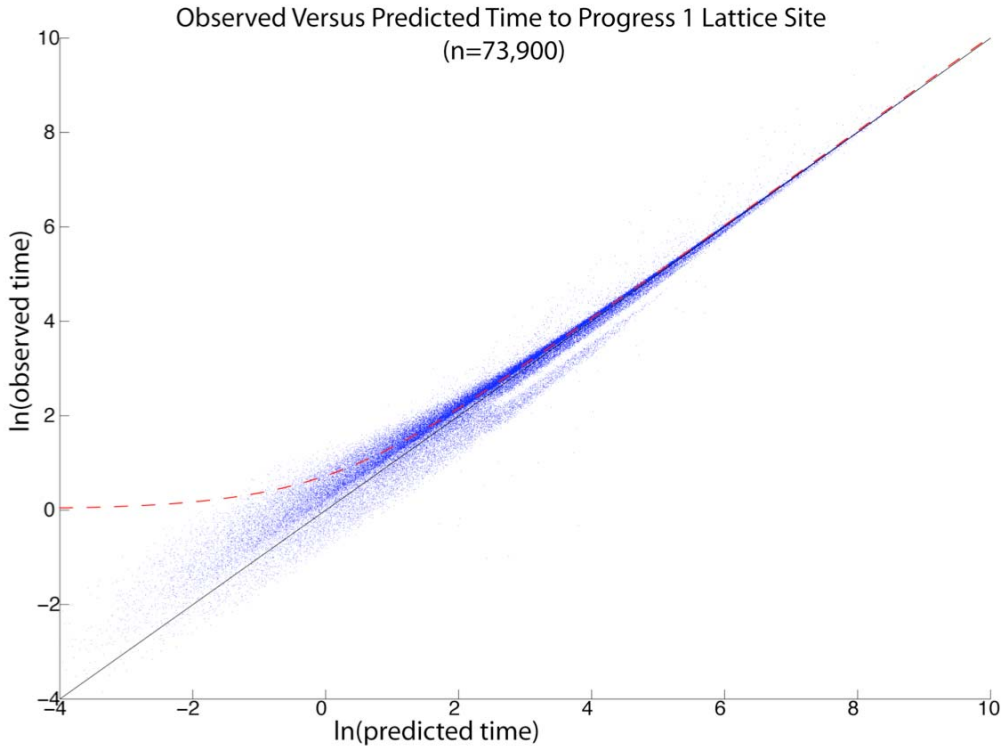

Figure 17: Quantitative comparison of observed versus predicted front velocity. Each dot is a parameter set exhibiting its predicted propagating behavior. The log-log axes are the predicted versus observed inverse velocities. The dashed red line shows an example of the deviation from identity that would be expected for adding 1 time unit to each step (to account for the finite rise time of a cell). It is unsurprising that the prediction becomes relatively better as the front slows down.

Discussion

Activator-inhibitor systems, and their ability to form and maintain patterns have been studied a great deal. Starting with Turing, most of this work has focused on the potential of reaction-diffusion systems with autocatalysis to have steady states that are unstable to finite-wavelength perturbations, and the dynamics of these systems (85-88, 92-100, 122). While the continuum has been studied extensively, there have also been many studies that have concentrated on cellular systems where isolated cells become active (93-100, 122). In particular, more than one system has been described in which an expanding patterned field both drives its own expansion and selects its own pattern subject to the linear instability governing a homogeneous steady state (96,122). The patterning system discussed here is unique in that it does not have a finite-wavelength linear instability: It does not rely on a large difference in the diffusive behavior of a local activator and long-range inhibitor, but on the large difference between the rate of pattern stabilization and field expansion.

Given an array of bistable cells that do not communicate with each other, any combination of active and inactive cells is a stable steady state of the system, and any arrangement that puts some cells at their unstable steady state is a steady state of the system unstable to perturbations of all wavelengths. The situation is nearly identical in this patterning system, with diffusive interactions turned on. Some of the steady states for the non-interacting system (those representing patterned half-spaces of high pattern density, for example) are no longer steady states, as they initiate propagating solutions, but no previously stable steady states have become unstable, and the cell-autonomous unstable steady state is never even approximately realized in the patterning process, let

alone simultaneously at multiple adjacent cells. The mechanism of pattern propagation is much more analogous to discrete autocrine models of signal propagation, such as those studied by Muratov and Shvartsman, in which cells are treated as a coupled array of bistable switches, or the extensively studied discrete Nagumo equation, than any classic propagating-patterning model system (115-117, 120). We have shown that the addition of an inhibitor to such a model very naturally gives it the ability to form patterns, and these patterns are formed by epitaxy, with template information about each previous column of cells being propagated to the next. Indeed, the specification of single active cells by this mechanism is a limiting case of the model, representing the slow expansion of a patterned domain. This means that in appropriate parameter regimes, the patterning behavior is essentially independent of parameter variations, a situation we have explored numerically.

At the heart of this patterning modality is the discretization of space represented by the cellular field. The fact that each cell has autonomous internal functioning that is not subject to any restrictions of continuity with its neighbors profoundly influences the interaction of adjacent cells with, for instance, a propagating front. As the front propagates there is a finite time delay between the activation of one cell and the next. If the internal dynamics of each cell is fast compared to this finite time delay, then the perturbation to the aggregate steady state of the two cells caused by the front is, by definition, large. If the internal dynamics are quite fast, the system is far outside the realm where linear stability analysis of multiple cells is meaningful.

Treating a group of cells as switch-like and giving them interactions potentially involving activation and inhibition, taken to an extreme, naturally yields dynamical

models that are more easily understood as finite state machines than as PDEs based on the diffusion equation. Indeed, the 1D map we presented in Figure 11, with *h* as a step-function is exactly this sort of model, and we will return to this concept in Chapter IV. What we have done in this work is take a model which is clearly based on the continuously variable nature of a biological system and that recapitulates the behavior of the system, and show that subject to physiologic assumptions it engages in patterning associated with its limiting behavior as an array of switches. We have shown that this behavior is dominant over a large range of parameters, and fails in the cases where explicit assumptions based on the observed physiology of the developing fly eye are violated. The exact structure of the boundary between patterning and non-patterning solutions remains obscure, and is likely a very difficult problem. However, we have characterized what appears to be the limit of importance, and have made predictions about the structure of solutions in parameter space. For a graphical summary of this parameter dependence, see Figure 18.

That the relevant limit is also one we consider to be physiologically important in the developing *Drosophila* eye, and the model's previous success in recreating patterning phenomena strikingly similar to experimental observations, suggest that this new patterning mechanism is the one that evolution chose to do this task, and gives us significant clues as to why it did.

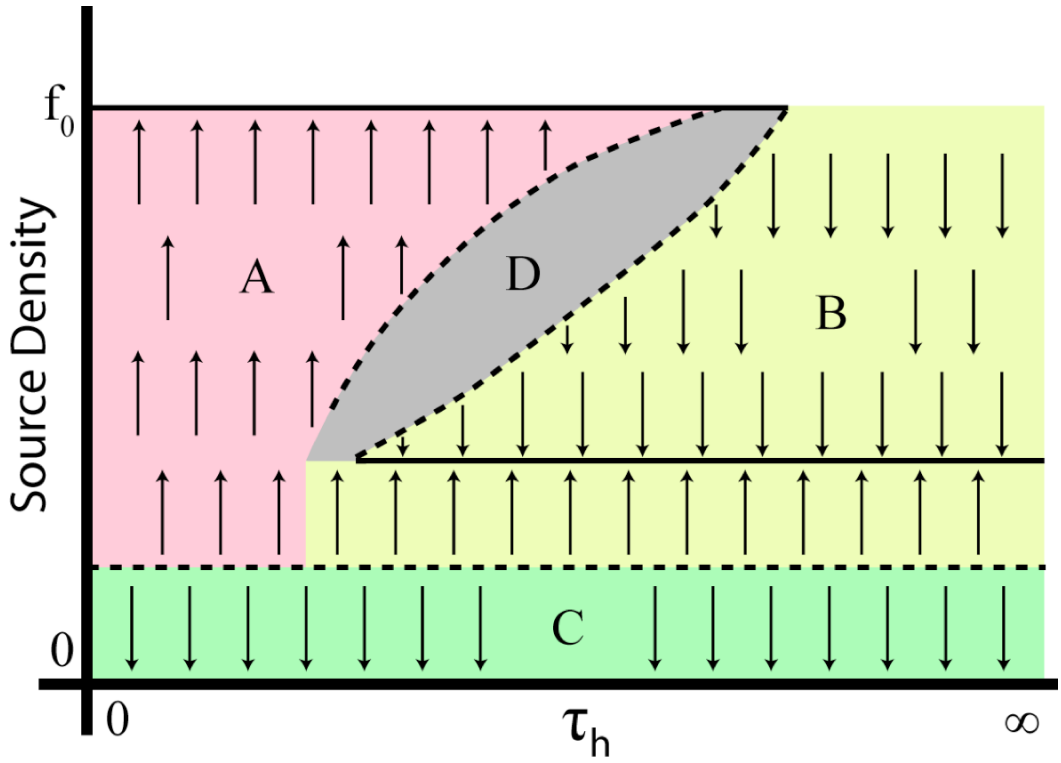

Figure 18: A theoretical bifurcation diagram for propagation and pattern formation with a parameter controlling the relative timescales of cell-autonomous dynamics and front propagation as bifurcation parameter. We take the source density of *h* as the output state, and it can range from 0 (stalled) to f_0, the maximum activity of a single cell. The analytic and numerical predictions we make in the paper are appropriate for parameter sets and initial conditions lying in regions B and C: stalled patterns and parameter sets with fast internal dynamics compared to front propagation. The structure of the boundary between B and A is unknown (gray, region D), but there are parameter sets where stable patterning and unpatterned front propagation are observed for different initial conditions. Parameters also exist where no patterning solution is possible, but a uniformly activating front is. Essentially, the parameter space of τ_h can generically be divided into three regions: a region of bistability with uniform and stalled solutions possible, a region of tristability where uniform, patterned, and stalled solutions are all possible, and the slow-*h* region of bistability between patterned and stalled solutions (which we have treated fairly comprehensively). The transitions between these regions could be as simple as saddle-node bifurcations, but if that is the case, the diversity and complexity of the transients involved near the boundaries has prevented us from seeing them clearly, and it is our feeling that much more complicated structures exist there.

Chapter III:

The Activation of Nearly Equivalent Cells, and the Resolution of Proneural Clusters

The variety of patterns that a propagating front in 2 dimensional media could generate is much larger than in one dimension. One key difference is that in more than one dimension, cells at the same position along an axis defined by direction of front propagation can be activated by a travelling front with an arbitrarily short delay between them. For this reason, it is impossible to define a single characteristic interval between the activation of one cell and the activation of the next. It is necessary to study the properties of groups of cells experiencing nearly simultaneous activation: a condition similar to what is assumed in many classic pattern formation models. As has been discussed, the model of R8 specification examined here does not appear to operate by one of these mechanisms. In this section I will analyze the function of our model of R8 fate specification in circumstances that mimic the selection of a single neural precursor from a small group of apparently equivalent cells expressing a proneural transcription factor: a proneural group.

Eye Context

As the MF sweeps across the eye disc, *atonal* is expressed in distinct stages. Anterior to column 0, the earliest column where *ato* expression is restricted to single cells, it is expressed broadly, and then in groups (intermediate groups, IGs, or proneural

clusters) that subsequently refine to one *ato*-expressing cell (47). Simultaneously, *senseless* expression increases in a few cells of the refining groups until it is expressed at a high level in the future R8, alone (2). This behavior, in which cells are first activated to an intermediate stage by signals associated with the MF, and then attain fate-permanence by a positive interaction between *atonal* and *senseless*, is captured in the 4-variable model of Lubensky et al (see Figure 5) (123-127). The refinement of proneural clusters to single cells, which happens in many other contexts, has long been of interest (7-14,32,41-43).

The refinement of clusters and the initial specification of their location and spacing have usually been regarded as physiologically distinct processes, with the former being driven by classical lateral inhibition, and the latter being mediated by longer-ranged signals mediated by, for instance, *scabrous* or *Egfr* (1-3,17,24). The observation that patterning in our model (including the appearance of structures resembling proneural clusters) can proceed with a single inhibitor, with one simple interaction with the master transcription factor, is surprising in this context; the inhibitor appears to be performing two distinct roles. It is necessary to reexamine the refinement of clusters of cells in the context of this model, which seems not to be behaving as previously thought.

Looking at the cells in a proneural cluster, it is nearly impossible to tell which cell will eventually become an R8 by examining *atonal* expression alone: They do, in fact, appear very nearly identical, as seen in Figure 19. It is quite simple, however, to look at the image of an eye-disc stained for *atonal* and pick out the one or two most likely cells to become R8s from any given proneural cluster; they will be near its posterior apex (2,46,47). This is because our eyes can recognize the pattern of previous R8s, and

extrapolate the pattern to the next column. What is significant about this exercise is that it makes clear that there is a hidden variable determining outcome, and the R8 is not randomly chosen from within the cluster (13). This is a good reason to suspect that the equivalence of the cells in a proneural cluster is superficial, and restricted to the expression of *atonal*: Our eyes need no special training to pick out the special cells, and are easily cued by the geometric arrangement of the cluster. What remains is to see if the understanding of the model behavior developed in the previous chapter works (with appropriate generalizations needed for 2D) to integrate this spatial information.

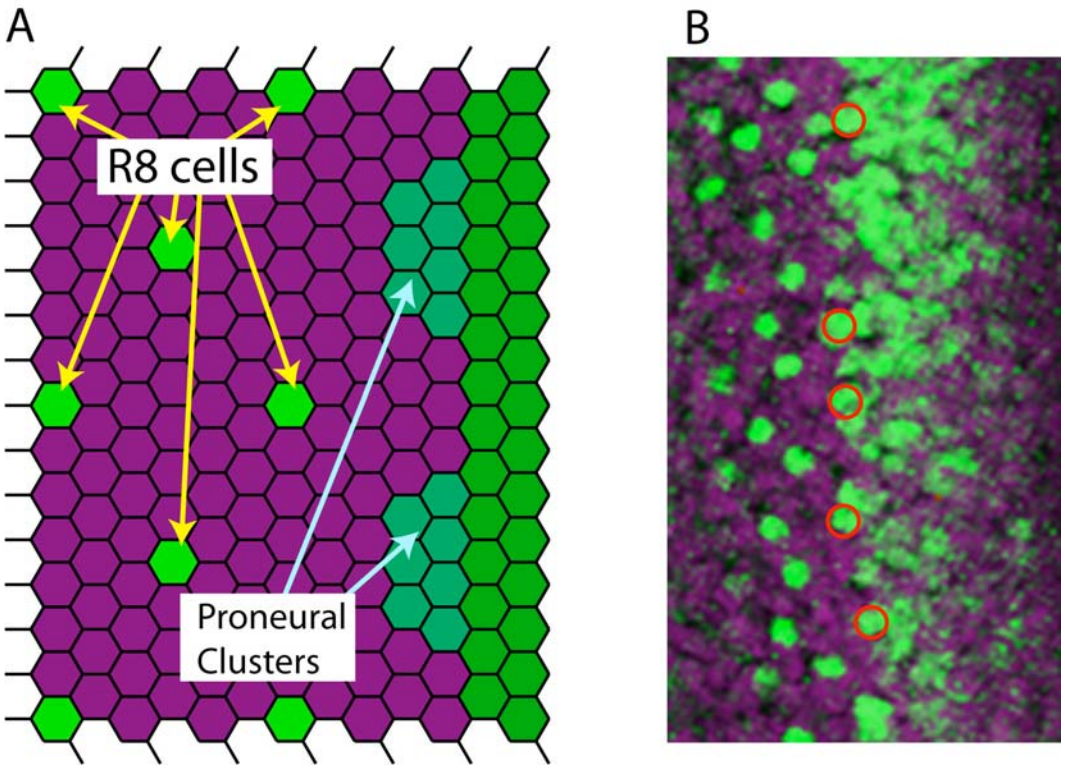

Figure 19: Schematic and image of wildtype MF stained for Atonal (green) and Dachshund (magenta). A) Shows a schematic of patterning near the MF, with previously specified R8 cells (green, single cells) influencing the position of the R8s being formed by the MF (right), which are selected from proneural clusters (turqoise). B) This image is a snapshot of patterning near the MF, which is moving from left to right. Proneural clusters in various states of resolution are visible. The red circles highlight the cells in these clusters likely to become R8s. Photograph courtesy of Nick Baker.

Approach

Following the multiscale approach outlined initially, and, once again, led by the fundamental autonomy of each cell, we go about this in the following way: First, the behavior of single cells in the 4-variable model must be described in some detail. Second, we will attempt to characterize the simplest possible patterning system that has a non-trivial patterned solution: Two cells interacting only with each other. The important connection to be made is the degree to which the two-cell behavior can be predicted from the properties of a single cell, and what aspects of (potentially detailed and complex) one-cell behavior must be known to make these predictions. Third, we will generalize the two-cell theory to small groups of cells that can be considered nearly equivalent in some way, which in this case means internally similar, and in direct contact. Again, this involves reducing the behavior of a functional module (a single mutually-inhibitory interaction) to its simplest fundamentals and using it as the foundation of our understanding of the next-larger level, which is a cluster of several equivalent cells. Fourth, we will examine proneural clusters that are not defined arbitrarily, but that arise in a simulated epithelium with a preexisting gradient of inhibitor produced by previously specified R8s.

Taken together, this represents a new theory of proneural cluster dynamics inspired by the eye disc system. As a general theory, it can make specific predictions for any well-formed question in its purview. We will discuss two specific predictions it makes, and counterpoint them with a classical lateral inhibition picture. We hope, also, to demonstrate the power of applying the analytic approach of dividing a system into autonomous functional modules defined by natural scale separations to biological

systems that integrate many different signals and processes. After explaining these behaviors, I will show simulation data that confirms the predictions made at each level of understanding.

Individual Cells

In the previous chapter, we showed that if bistable cells exchange 1) adequate activating signals, and 2) adequate inhibitory signals, and provided that the progression of the first signal is adequately slow, they are likely to become activated in a self-propagating pattern characterized by isolated active cells. We must generalize each of these concepts to the more complicated 4-variable model to proceed. The specific form of the model is as follows:

$$\begin{aligned}
\partial_t a_n &= \frac{a^{n_a}}{A_a{}^{n_a} + a^{n_a}} - a_n + B\frac{s^{n_s}}{S_a{}^{n_s} + s^{n_s}} + G\frac{h_n(t)}{1+\left(\frac{u_n}{U_a}\right)^{n_u}} \\
\tau_s \partial_t s_n &= \frac{a^{m_a}}{A_s{}^{m_a} + a^{m_a}} - s_n \qquad \textbf{(1)} \\
\tau_u \partial_t u_n &= \frac{a^{p_a}}{A_u{}^{p_a} + a^{p_a}} - u_n + D_u \sum_{n'} D_{n,n'}(u_{n'} - u_n)
\end{aligned}$$

The model discussed in the previous chapter was simplified for the sake of 1) facilitating a complete understanding of cell dynamics, and 2) allowing a very broad random search of parameter space for unexpected limits of behavior. This simplification eliminated the formation of proneural groups. Two main differences should be obvious between equation (1) and equation (4) of the previous chapter. First, we have removed the regulation of *h*, and made its time-dependence explicit, and shifted its meaning in such a way that *h* is now activation activity as seen by *a*, or *g(h)* from the previous chapter. The progress of a self-activating front is well understood at the level of a single

activator, and the characteristic scale and time of *h* dynamics are such that this field is not greatly perturbed by the local behavior of a few cells, regardless of what they do; dynamic *h* is unlikely to add much to a study of patterning in a single proneural cluster (115,116). It is enough to assume that a front exists, which we do by imposing an appropriate approximate time dependence on *h*, as derived in the previous chapter. Specifically, we use a piecewise linear form for the spatial variation of *h* that goes from zero to one over unit distance, and translate this form uniformly over space at varying velocities. Second, we have added a positive feedback loop between *a* and a fourth field, *s*, named for the gene *senseless*, which encodes a zinc finger transcription factor (126). This delayed activation loop allows for staged activation of the proneural transcription factor *a*. For this arrangement to give the desired behavior, parameters must be chosen so that a cell expressing *a* alone cannot sustain *a* expression without external activation from *h*, but a cell expressing both *a* and *s* can, yielding a bistable switch that goes through a distinct, reversible stage of intermediate activation, as illustrated in Figures 20 and 21. In this system, external activation leads cells to produce *a*, which reinforces its own production, but not to a sufficient degree as to make it independently high (127). This level of *a*, in turn, is sufficient to cause the production of some amount of *s*, which feeds back positively on *a*. At some point, the autoactivation of *a* and the positive feedback loop *a*-*s*-*a* become sufficient to maintain a high level of *a* (and, concomitantly, *s*) production. This situation can be very similar to the one-stage switch of the 3-variable model if the dynamics of *s* are fast, and *s* is simply slaved to *a*. There is a line in the *a*-*s* plane that defines the boundary between systems proceeding to the low steady state under no external activation (or large inhibition), and those proceeding to the high steady state.

This line is the unstable manifold of the intermediate steady state of the *a*-*s* system, illustrated in Figure 21, and is subsequently called the "fate-permanence separatrix," or simply "the separatrix." Third, we have replaced the tridiagonal nearest-neighbor diffusion operator with a coupling matrix $D_{n,n'}$ that represents the normalized diffusive coupling between adjacent cells. How we define this matrix, in detail, is described in Appendix D.

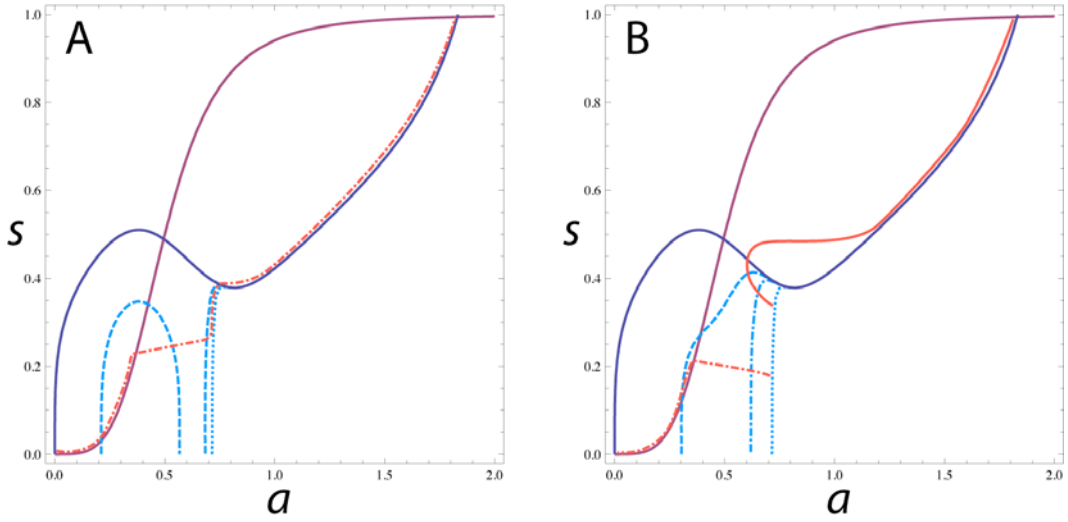

Figure 20: Nullclines and trajectories for different values of *h* and *u*. In each of the above graphs, the solid purple line is the nullcline in the *a*-*s* plane for $\partial_t s=0$, the various blue lines are the nullclines for $\partial_t a=0$, and the red lines are trajectories of the dynamical system representing a single cell in the 4-variable model. A) shows the nullclines for $h=0$ (solid, dark blue), an intermediate value of *h* (dashed, cyan), and maximal *h* (dotted, cyan), with no externally produced *u*, and $\partial_t u=0$. The condition of most interest is when *a* dynamics are faster than *s*. In this case, the expression of *a* and *s* in a cell starting at $a=s=0$ and experiencing increasing *h* migrate upward with the lower stable steady state until this state is lost in a saddle node bifurcation. At this point, the trajectory increases rapidly in *a* to an intermediate (proneural cluster-like) state. The amount of *s* then increases until it reaches a point at which *a* production can run away toward the permanent high steady state. This is illustrated by the dash-dotted red line. B) The second condition of interest is a cell that has received a proneural signal, but in the course of differentiation also receives an inhibitory signal from a neighbor. The nullclines in this graph represent a system with full *h* activation and increasing (dotted cyan<dash-dotted<dashed<solid blue) *u* from an external source. The red trajectories represent the two types of path a partially differentiated cell (the trajectories start at the proneural cluster stage, in the figure) could follow upon receiving this inhibitory signal. The dash-dotted red line represents a cell that has not yet achieved fate-permanence and returns to the low steady state. The solid red line represents a cell that has differentiated further, to the extent that its fate is no longer dependent on external activation, and it proceeds to the high *a*-*s* steady state.

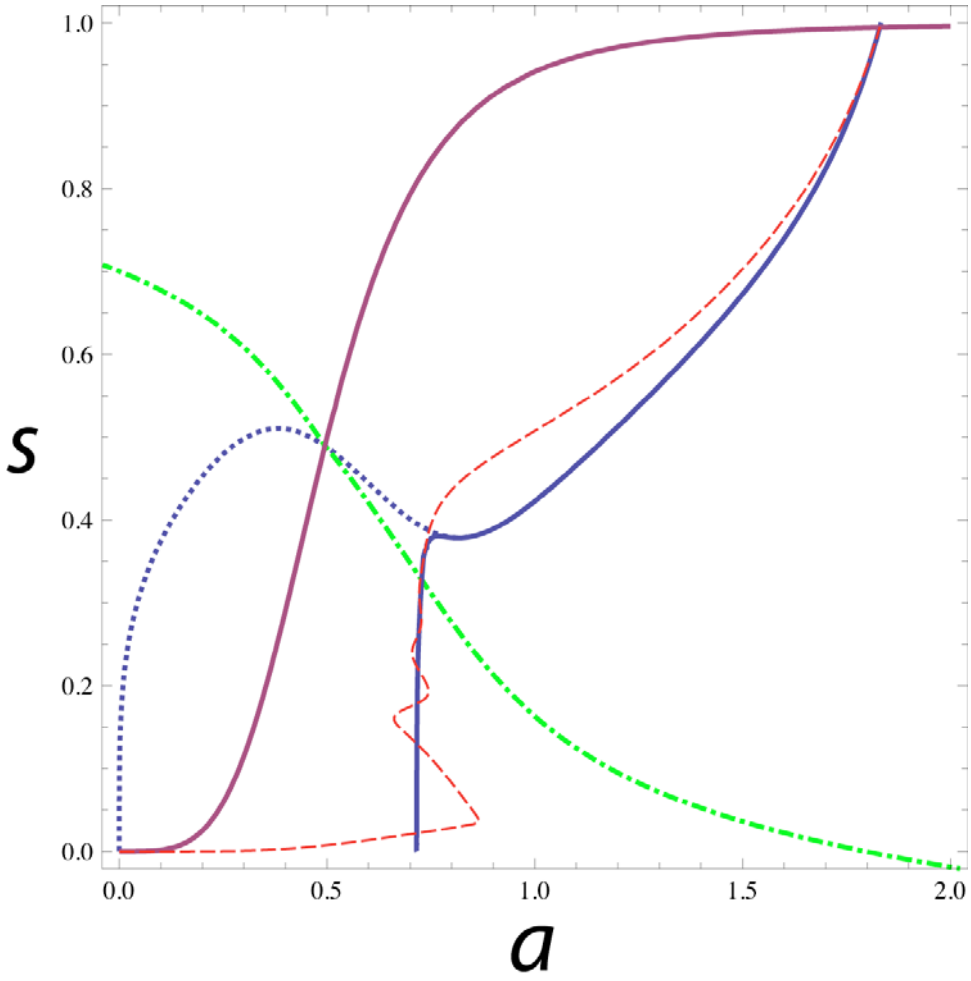

Figure 21: Nullclines, trajectory, and separatrix for an isolated cell. Here, the solid purple line is the nullcline in the *a*-*s* plane for $\partial_t s=0$, the solid blue line is the nullcline for $\partial_t a=0$ under maximal activation (no inhibition), the dotted blue line is the same nullcline under maximal inhibition, or no activation, and the dashed red line is an actual trajectory of the fully dynamical system starting at $a=s=0$ and suddenly experiencing maximal *h*. In this case, the trajectory moves rapidly to the intermediate value of *a*, about which it appears to experience damped oscillations. Eventually, it escapes this intermediate state and moves to the stable attractor at high *a* and *s*. The dash-dotted green line is the unstable manifold of the unstable fixed point of the fully inhibited system. In such a system, any trajectory that starts above this line will end up at the high fixed point, and a trajectory that starts below it will end up at $a=s=0$. It is the separatrix defining cells that will certainly become R8s from those that may or may not. We define the time T_1 as the time when a cell's trajectory crosses this separatrix, and its fate is sealed.

The time it takes for a cell that has received an activation signal to cross the immortality separatrix is a key intrinsic timescale of that cell. Before the cell crosses this line, interference from other cells through inhibition can substantially alter its behavior. Afterward, its fate is sealed. For an isolated cell (cell α), this time is a function of the amount of (static) external inhibition the cell is receiving, and we will denote it as $T_{1\alpha}(u_{ns\alpha})$, where the mnemonic device at work is that this is the time the cell crosses the first important threshold (T_1), which is a function of the non-self u (u_{ns}) it feels. In general, cells are capable of 2 local actions, and pattern formation requires both persistent auto-activation, and insurmountable inhibition of neighbors. The first process is summarized in T_1, the second is realized when an activated cell has been activated long enough that it has produced enough inhibitor to completely suppress a neighbor (cell β). This time depends on both the amount of inhibitor felt by cell α, which governs how quickly inhibitor is produced, and the amount of external inhibitor at cell β, which dictates how much additional inhibitor is needed to shut that cell down. We will denote this time as $T_{u\alpha}(u_{ns\alpha},u_{ns\beta})$, which is the time it takes cell α after activation to inhibit an adjacent cell, β, and can be thought of as the time to critical u. The concept underlying T_u should be familiar from the previous chapter. T_1 is a new concept, for this system, and is necessary for comparing similar cells activated at arbitrarily small delays. Alone, these two times are adequate to explain a large variety of patterning behavior, and are a simplification of what can be surprisingly complicated single cell behavior. For a sampling of the range of behavior a single cell is capable of, refer to Appendix F. In that appendix we examine the stability of intermediate a at fixed s and uncover the potential

for oscillator-like behavior of the system. The dynamics of cells at this intermediate state can be important, as that is where they are most susceptible to external inhibition, but for most parameters of interest, we believe this state is not long-lived enough to have much effect on fate determination.

Two-Cell System

The next step is to examine a system of two identical cells that can interact by exchanging *u*, represented by the following equations, where we have name the two cells α and β, introduced the constant p_c representing the effective population of a proneural cluster in which the test cells are embedded, and which act as sinks for inhibitor *u*, and a time delay Δt which sets a relative delay in their time of activation.

$$
\begin{aligned}
\partial_t a_\alpha &= \frac{a_\alpha^{n_a}}{A_a^{n_a} + a_\alpha^{n_a}} - a_\alpha + B\frac{s_\alpha^{n_s}}{S_a^{n_s} + s_\alpha^{n_s}} + G\frac{h(t)}{1+\left(\frac{u_\alpha + u_{ns\alpha}}{U_a}\right)^{n_u}} \\
\partial_t a_\beta &= \frac{a_\beta^{n_a}}{A_a^{n_a} + a_\beta^{n_a}} - a_\beta + B\frac{s_\beta^{n_s}}{S_a^{n_s} + s_\beta^{n_s}} + G\frac{h(t+\Delta t)}{1+\left(\frac{u_\beta + u_{ns\beta}}{U_a}\right)^{n_u}} \\
\tau_s \partial_t s_\alpha &= \frac{a_\alpha^{m_a}}{A_s^{m_a} + a_\alpha^{m_a}} - s_\alpha \\
\tau_s \partial_t s_\beta &= \frac{a_\beta^{m_a}}{A_s^{m_a} + a_\beta^{m_a}} - s_\beta \\
\tau_u \partial_t u_\alpha &= \frac{a_\alpha^{p_a}}{A_u^{p_a} + a_\alpha^{p_a}} - u_\alpha + D_u\left(u_\beta - (p_c - 1)u_\alpha\right) \\
\tau_u \partial_t u_\beta &= \frac{a_\beta^{p_a}}{A_u^{p_a} + a_\beta^{p_a}} - u_\beta + D_u\left(u_\alpha - (p_c - 1)u_\beta\right)
\end{aligned}
\qquad \textbf{(2)}
$$

Examination of the nullclines of this system reveals 9 steady states at h=0, $u_{ns\alpha}$=$u_{ns\beta}$=0, and Δt=0, if the cells are independently bistable. Four of these steady states are linearly stable and represent the ++, +-, -+, and -- states of the system, where + and -

refer to cells having either high *a* production (near *1+B*), or low *a* production (near zero). There are also 4 saddle points that correspond to one cell being near a stable state (+ or -), and one cell being near its unstable steady state. We'll call these saddles +0, -0, 0+, and 0-. The ninth steady state is an unstable node, and its nature should be obvious if we give it the name 00. So far, there is nothing about this system to differentiate it from two completely independent cells that happen to be graphed on the same axes. At high *h*, provided *G* is large enough that the bistable cells can be switched on, the -- stable steady state, the unstable node 00, and the saddles 0- and -0 have been lost, which should not be surprising given the bifurcation behavior of a single cell. Four steady states do not generically disappear in a single bifurcation, however, so this must be examined a bit closer. Zooming in on this process, it becomes clear that under increasing *h*, nodes --, -0, and 0- coalesce in a subcritical pitchfork bifurcation. This has codimension-1 because there is a symmetry related to the exchange of the two cells. The single steady state left by this process (it makes sense to call it --, still) is a saddle that is attractive along the symmetric axis, a_1+a_2, and repulsive in the antisymmetric direction. As *h* increases further, -- and 00 annihilate in a saddle node bifurcation, leaving only the steady states that have high *a* in at least one cell. These relationships are shown in Figure 22.

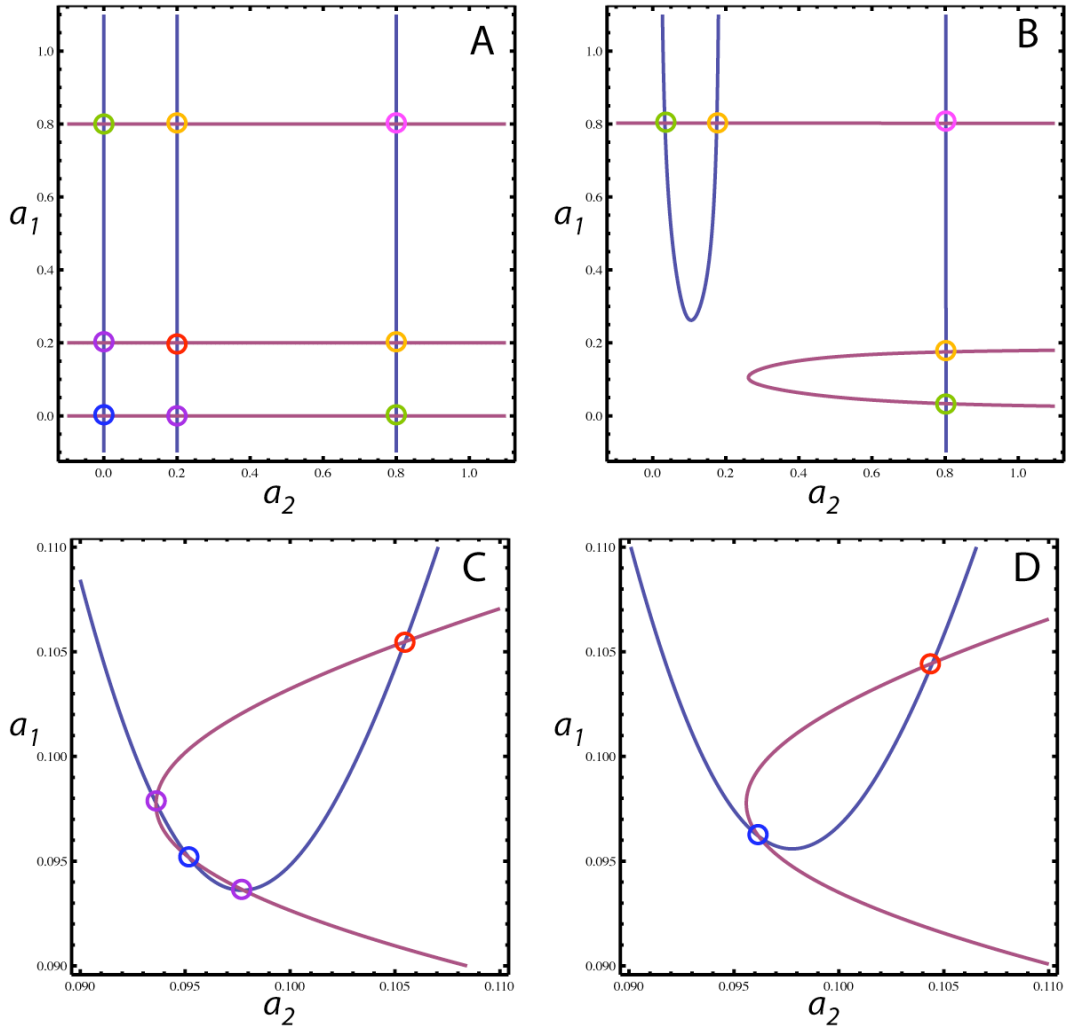

Figure 22: Nullclines and steady states for a two-cell system. A) shows the $\partial_t a=0$ nullclines for two interacting cells and $h=0$. The magenta circle marks the ++ stable steady state, and the blue circle marks --. The red circle is the unstable node 00. The paired green circles mark the asymmetric stable steady states, +- and -+. The purple and orange circles mark the various saddles, 0+, +0, -0, and 0-. B) shows the same system as A, but with high h. Several steady states have disappeared: --, 00, 0-, and -0. C) This figure zooms in on the lower 4 steady states as h approaches the first bifurcation, and D) shows the same region just after bifurcation. Varying h as a bifurcation parameter has lead to a subcritical pitchfork bifurcation on the a_1-a_2 axis. Increasing h even more leads to a saddle-node bifurcation between the blue and the red circles.

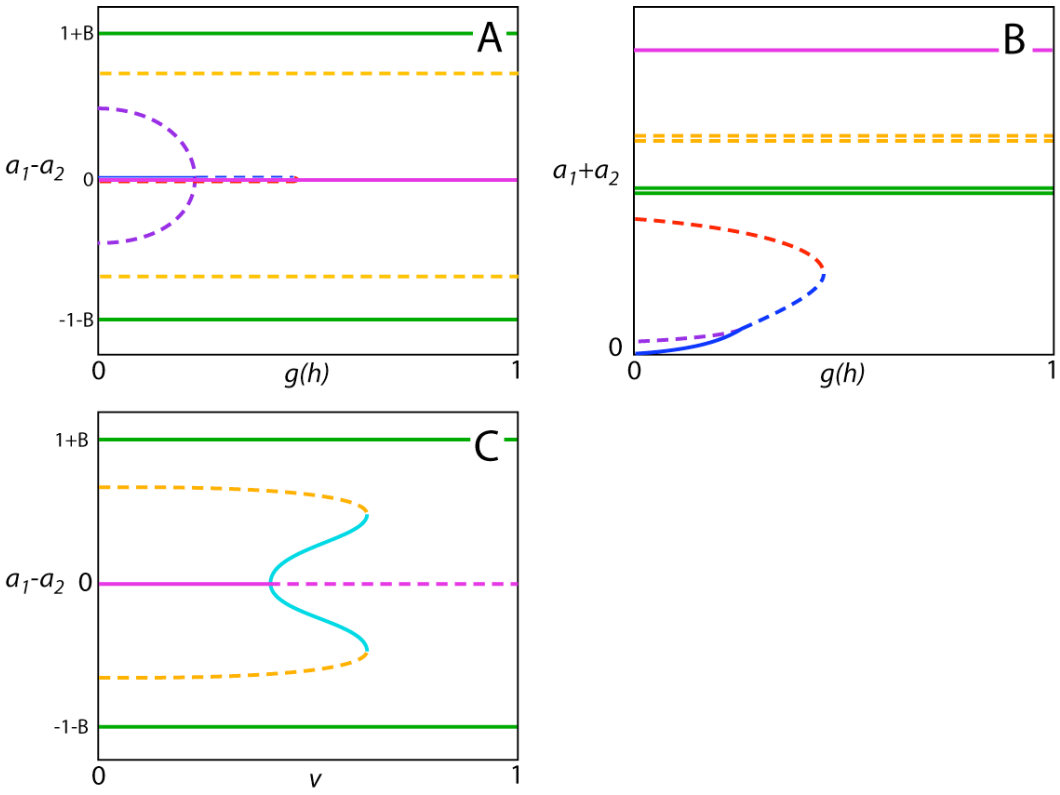

Figure 23: Bifurcation diagrams for two cells. In these graphs the convention is that a solid line represents a stable steady state, and a dashed line represents an unstable one. The color conventions are preserved from Figure 4. A) shows the coalescence and annihilation of the lower steady states (and the invariance of the higher ones) with increasing *h*, with special emphasis on the asymmetric states. B) shows the same process, but looking at the symmetric aspect of a_1 and a_2. The similarity of this diagram to the simple bistable switch of a single cell should be apparent. C) shows the bifurcation diagram of the higher steady states, using the maximum strength of a hypothetical juxtacrine inhibitor, *v*, as the bifurcation parameter. The symmetric high steady state, ++, gives rise to two additional asymmetric steady states in a supercritical pitchfork bifurcation, which subsequently annihilate with the saddles 0+ and +0. In the end, the only stable steady states are the two high-amplitude asymmetric ones.

The presence of a subcritical pitchfork bifurcation in this system suggests the presence of the discrete analog of the finite-wavelength instability that leads to Turing patterns. Closer examination reveals that this is not the case, however, and to make this subcritical pitchfork important to the final state of even the two-cell system would require an extreme level of parameter fine-tuning, and physiological conditions so idealized as to be ridiculous.

Three conditions would need to be met to have random small fluctuations about the newly unstable low symmetric steady state be amplified and quenched into the final state, here. First, the system must be adequately close to having a pitchfork bifurcation. A pitchfork is not a generic codimension-1 bifurcation; its existence is allowed by an underlying symmetry of the system. In this case, that symmetry arises from the two identical cells: they are exchange-symmetric. Of course, in real life, the cells are not equivalent. Beyond this, and of more interest to modeling, where idealized structures can be realized, there is a static symmetry-breaking influence that will be experienced by any two cells: The external inhibitor they feel from previously specified R8s. This influence is large, and will drive the fraction of cells that actually ever see something like a pitchfork bifurcation effectively to zero.

Second, the instability created by a pitchfork is linear. It takes time for a trajectory to leave the vicinity of the old stable steady state. This will happen deterministically with a characteristic timescale, which, in this case, is near 1, the intrinsic timescale of a. If the system undergoes other changes more quickly than this, the influence of the immediately post-bifurcation state can be near zero. In general, in this system, the unstable steady state created by the pitchfork bifurcation is subsequently

annihilated by the unstable node, 00, which leads to a finite-width basin of attraction for ++ extending down to $a_1=a_2=0$. The rapid succession of these events is a structural feature of the model, since the influence of *h* is sigmoidal and monotonic in time. The only obvious way to allow a lengthy pause in the linearly-unstable pattern-forming state is to tune the strength of the term containing *h* and *u*, (by varying *G*, most directly) such that the saddle-node annihilation of – and 00 never occurs, and the landscape is never changed dramatically. With even slight cooperativity in the equations, this requires very fine-tuning of *G*. It is worthwhile to recall that *G* rather directly relates to the strength of a promoter on physical DNA. The idea that the maximum activity of a single promoter would need to be tuned to a part in a hundred to ensure proper functioning of an entire organ is not easily believed, let alone tuning to parts in thousands or millions (128-130).

Third, even if two cells have a pitchfork bifurcation, and the topology set by that bifurcation persists forever, it is a moot point if the trajectory of two cells never closely approaches that steady state. This brings into play the second large symmetry-breaking influence any two cells will experience: The MF, which has a direction. In phase space, this symmetry breaking is no different in its pitchfork de-idealizing properties than differing amounts of external inhibitor, but the dynamic nature of this feature in the model, as well as its dramatic appearance in the physical system make it unique.

Now that we have listed some reasons why the simplest (linear) explanation of patterning can't be correct, we turn to what actually is important to the creation of the observed asymmetric steady states. Let's begin with some context, as illustrated in Figure 24.

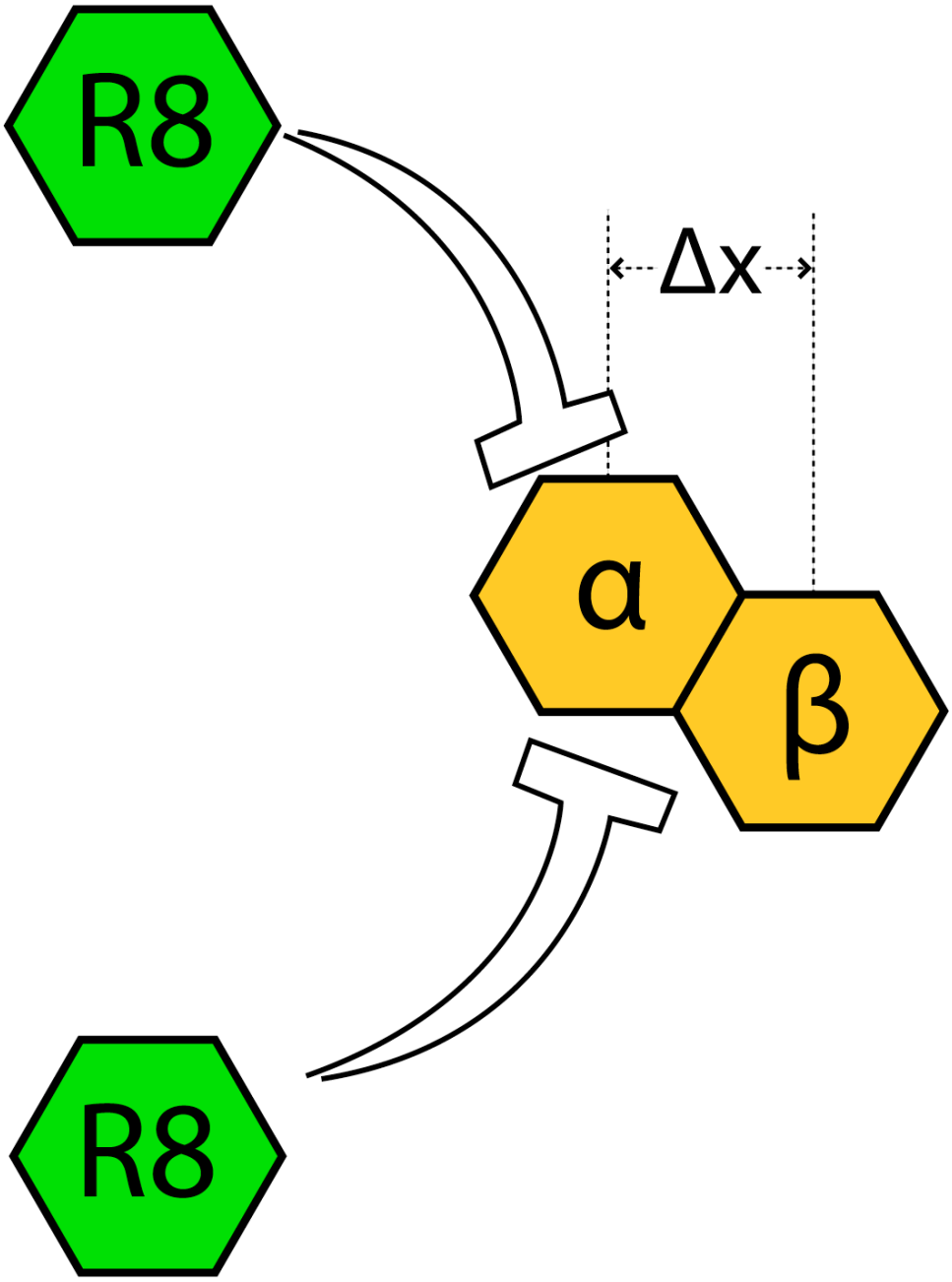

Figure 24: Schematic of the two-cell system. Cell α and β are the two cells that we are examining. They are very close together, and are separated by a distance Δx in the direction of MF travel. This distance and the velocity of the furrow can be translated into a delay time, Δt, between their respective activations. The cells also experience an inhibitory signal from previously specified R8 cells. We don't model these cells explicitly, in this case, but determine the behavior of cells α and β for all possible values of external inhibitor.

Consider the two cells, α and β to be identical, adjacent, and taken from an eye disc epithelium. In addition to $u_{ns\alpha}$ and $u_{ns\beta}$, the externally derived inhibitor at each cell, these cells are characterized by their location compared to the movement of the MF. If the MF propagates uniformly at a constant velocity, *v*, in the *x* direction, the activation of one cell versus the other is characterized by a simple constant time delay.

$$h_\alpha(t) = h_\beta(t + \Delta t)$$
$$\Delta t = \frac{(x_\beta - x_\alpha)}{v} \qquad \textbf{(3)}$$

Considering independently the possible end state of each cell in a 2-cell simulation, we get 2 inequalities relating the cellular characteristics T_1, T_u, and Δt. For cell β to end up in the low steady state, we require:

$$T_{1\beta} + \Delta t > T_{u\alpha} \qquad \textbf{(4)}$$

That is, cell α must make enough inhibitor to prevent cell β from being activated before cell β crosses the separatrix. A similar condition holds if we require cell α to end up in the low steady state:

$$T_{1\alpha} > \Delta t + T_{u\beta} \qquad \textbf{(5)}$$

To determine whether these inequalities are satisfied, we can either simulate the 2-cell system directly, or we can estimate the times from observing single cells. The simplifiying assumption at work, if these methods are to agree, is that the times T_1 and T_u are not functions of Δt. The degree to which this holds true is dependent on parameters,

but it is the case for a wide range of parameters of interest. Figures 25 and 26 show two simulations of a system with different Δts.

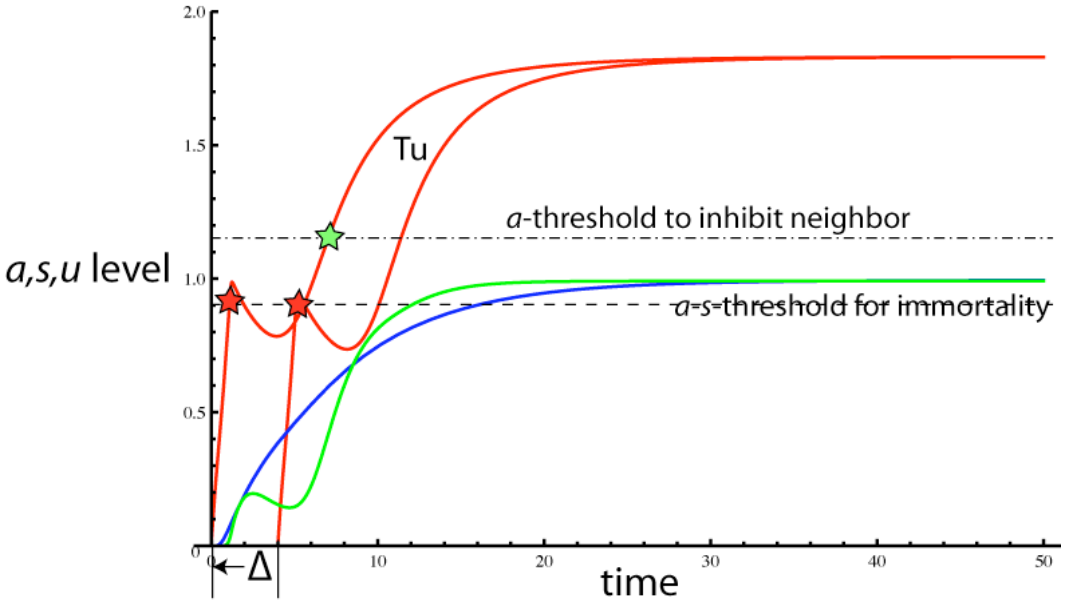

Figure 25: Trajectories over time of two identical cells activated at very small delay. The red lines represent *a* in cells α (starts at $t=0$) and β (starts at $t=4$). The blue line is *s* in cell α, and the green line is *u* in cell α. The red stars mark the point at which R8 fate becomes certain for a particular cell, at a delay T_1 from initial activation. The green star represents the point at which a cell is able to inhibit its neighbor, T_u. Of course, this value has to do with the amount of *u* that has been transported to that neighbor, but for simplicity, here it is a function of *a*. In this instance, $T_{u\alpha} > \Delta t + T_{1\beta}$, and $T_{1\alpha} < \Delta t + T_{u\beta}$, so both cells end up activated.

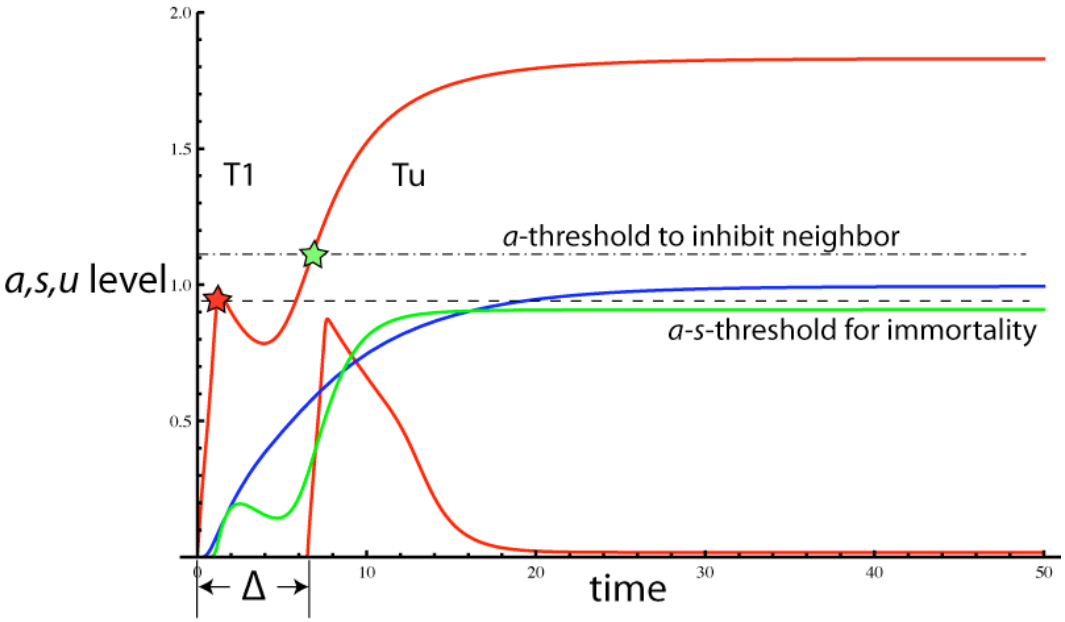

Figure 26: Trajectories over time of two identical cells activated at larger delay. The red lines represent a in cells α (starts at $t=0$) and β (starts at $t=6.2$). The blue and green lines are s and u in cell α, respectively. The red star marks the point at which R8 fate becomes certain for cell α, at time T_1. The green star represents the point at which that cell critically inhibits its neighbor, defining T_u. Here, $T_{u\alpha}<\Delta t+T_{1\beta}$, so only cell α achieves R8 fate.

But wait: How can this be true, at all? Varying Δt, at the point where it is becoming just large enough for inequality (4) to be satisfied, $T_{1\beta}$ is, by definition, diverging toward infinity, and thus changing very rapidly. The key to this seeming paradox is that the divergence of $T_{1\beta}$ is very sudden, and its behavior up until that point is basically independent of Δt. This is virtually guaranteed by the sigmoidal inhibitor production and response found in equation (1) and (2). In the language of stability analysis, we can say that for trajectories of the two cell system, the perturbation represented by Δt near the equality condition of (4) or (5) is large, but the low order terms in a series expansion for small Δt of the perturbed trajectories (expanded about the unperturbed trajectories) are very small. The system's behavior near the conditions that separate important outcomes, then, is highly nonlinear, and behaves nothing like the instabilities involved in Turing patterns, or classical Delta-Notch lateral inhibition. The abrupt divergence toward infinity of T_1, and the fact that it is basically a cell autonomous quantity, otherwise, pushed us down the path of treating the system, as a whole, as a set of Boolean variables that evolve solely according to a set of delays that govern their state, and the ability of their neighbors to change state.

Multiple Cells

If the cells are truly behaving independently, and the numbers T_1 and T_u can be taken straight from 1-cell trajectories (these trajectories can trivially represent more than one cell being simultaneously activated, what is important is that there is only one independent trajectory), it is easy to generalize (4) and (5) to apply to cells γ, δ, ε, etc,

provided these cells interact with each other identically: i.e. for a compact cluster. This means that we expect the 2-cell analysis, as derived from single cell behavior, to generalize by simply writing down inequalities (4) and (5) for all combinations of mutually adjacent cells. It is possible, in theory, to write down distinct inequalities of the form (4) and (5) for larger groups of cells with less restricted symmetry, but much of the elegance (and thus advantage) of this approach is lost: The quantitities T_1 and T_u can no longer be taken straight from single cells, since the delay involved in diffusion of *u* to a non-adjacent cell is much larger than transport to an adjacent one, and will be dependent on the many diffusion coefficients linking several nearby cells in roughly equal measure. If all the cells are equivalent and adjacent, though, and we examine every possible pair of cells to determine if one of the cells will be suppressed by the other, then the outcome of the whole system can be summarized by identifying cells that are never effectively suppressed by any neighbor. These cells will end up activated permanently, and become R8s.

Small groups of cells are well and good, but we are interested in 2D epithelia made up of tens of thousands of cells. It is desirable to map the (understandable) small groups of nearly-simultaneously activated cells from the previous discussion onto the proneural clusters of eye-disc development, since these co-evolving cells are nearly all co-adjacent. To do so, we need a method of identifying these clusters. Fortunately, an obvious method exists for the eye disc. Around each R8 precursor cell that has fully differentiated (in the model, this means that it is very near its high steady state value for *a*, and has been there for awhile), there is a roughly circular zone of cells that are fully inhibited. Nearby R8 cells have, in general, overlapping zones of complete inhibition.

The surrounding, incompletely inhibited cells are thus arranged in a scalloped pattern, with points pointing opposite the direction of MF movement. The cells at these points form the natural starting point for delimiting distinct proneural clusters. An incompletely inhibited cell that receives an activating signal and is not contiguous with a preexisting cluster founds a new cluster, and contiguous cells can be added to it in the order they receive activating signals from the MF (their location on the *x* axis). At some point, this process can be stopped, as the delays of subsequent cells from the activation of the first cell become too large for those cells to be pertinent to the R8 decision.

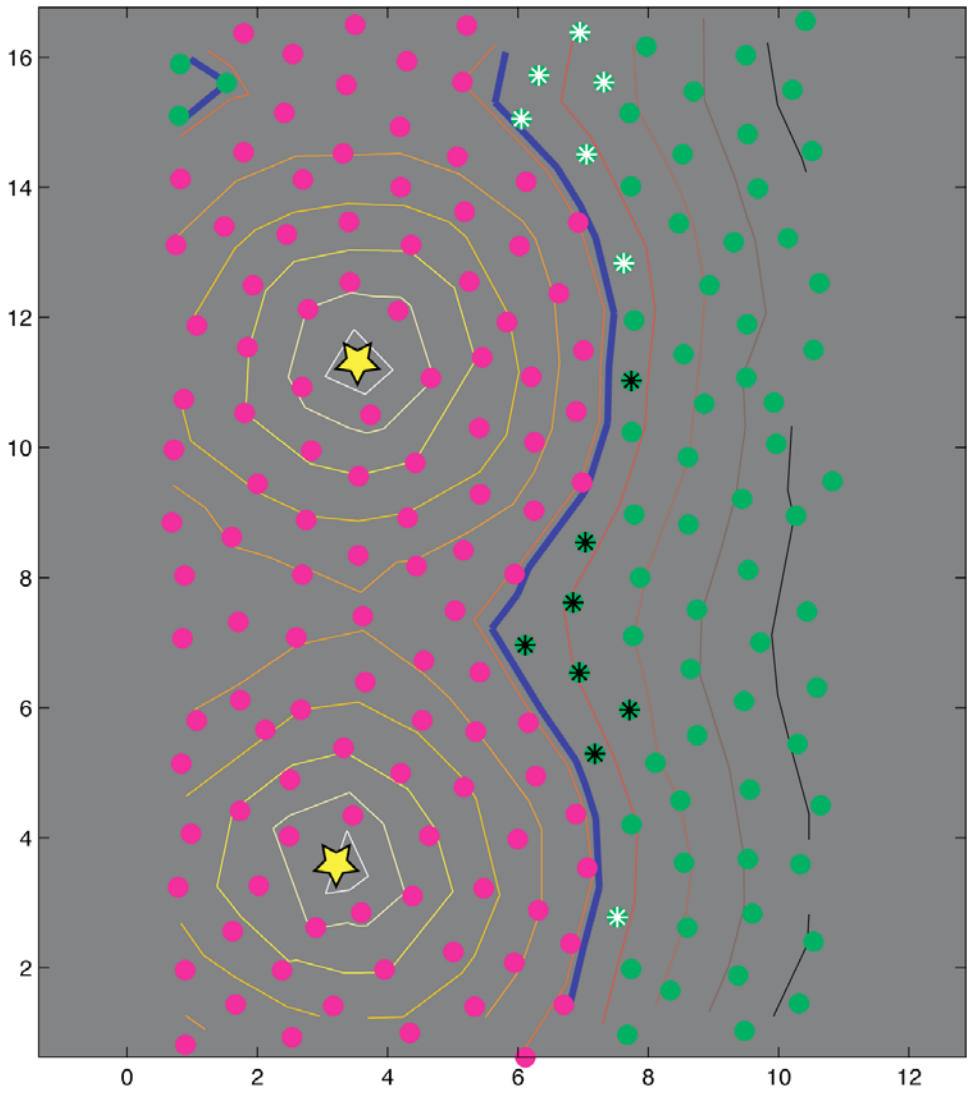

Figure 27: A small grid showing naturally arising proneural clusters. In this figure, the markers are the centers of cells in a 16x12 cell epithelium. The contour lines illustrate the stationary amount of inhibitor (on a log scale) produced by two template R8 cells (yellow stars). The strong, blue contour shows where the inhibitor is at the critical level needed to completely inhibit cells from being activated, and separates the inactivatable cells (magenta) from the ones of undetermined fate (green). The boundary conditions are periodic in the vertical direction, and the MF moves to the right. The white and black stars that mark some cells identify the first seven cells that can be assigned to one of two proneural groups, as explained in the text. Indeed, this picture indicates that seven is probably an over-large number, and that five or six cells need to be considered in each case.

Parameter Dependence

Once again, it is interesting to consider how general this theory of proneural group resolution is with respect to models of the form of equation (1). Compared to the model of the previous chapter, the system under examination here is considerably more complicated, and we expect it to do the unexpected more frequently. As well, the nature of the tests that must be done are significantly more computationally taxing than the integrations of the previous model, preventing us from testing hundreds of thousands of parameter sets with relative impunity. We can, however, do a few thousand.

As previously, there are several conditions that must be met by any parameter set before we consider it as being subject to this theory. Analogous to the requirement in the previous parameter scan that *a* be irreversibly bistable is the requirement that *a* and *s*, taken together, be irreversibly bistable. This is easily determined by examining the number of solutions with $0 \le a \le 1+B$ to the nullclines for $\partial_t a$ and $\partial_t s$ (equation (6), below), which should be three: One stable at $a=0$, one stable near $a=1+B$, and one unstable somewhere in between.

$$0 = \frac{a^{n_a}}{A_a{}^{n_a} + a^{n_a}} - a + B\frac{s^{m_a}}{S_a{}^{m_a} + s^{m_a}}$$
$$s = \frac{a^{n_s}}{A_s{}^{n_s} + a^{n_s}} \qquad \textbf{(6)}$$

For there to be an intermediate state, where cells are partially activated, but not yet permanently fated, the delay intrinsic to the *a*-*s*-*a* activation loop must determine when cells irreversibly become R8s. This would be undermined if the direct autoactivation of *a* were strong enough to sustain its production absent an external signal,

which imposes the further requirement that there be only a single solution to the following equation: A stable fixed point at a=0.

$$0 = \frac{a^{n_a}}{A_a^{\,n_a} + a^{n_a}} - a \qquad \textbf{(7)}$$

For stable, non-trivial patterning solutions to exist, a cell must be able to inhibit its neighbors, and must be able to be activated by the available external signal from h. Here, the situation becomes somewhat trickier, and simply examining the nullclines for an isolated cell is inadequate. The trouble arises from the ability of a cell to inhibit itself. With u fully dynamical (not infinitely fast, as in Chapter II), and cells embedded in an irregular 2D geometry, the amount of its own u that a single R8 cell feels depends on its own a history, its connections to its neighbors, those cells' connections to their neighbors, etc. Previously, they were infinitely fast, placed on a regular 1D grid, and self-u could be reduced to a function of a. In short, autoinhibition is necessarily a function of system geometry, and we are interested in studying many different geometries. It is necessary to evaluate the "can be activated" and "can inhibit neighbors" requirements empirically (by integrating the equations) for each significantly new geometry we introduce.

In addition to this effect of diffusible u, there is the potentially non-trivial effect of summed u from multiple cells activated nearly simultaneously. To understand this, picture a group of cells being activated by the MF. Each cell is activated at a delay from the previous one, as discussed. If the MF is moving very slowly, the bulk of the evolution of a, s, and u in cell α is done by the time cell β is activated, and its trajectory is likely to be similar to that of a single, isolated cell. For two cells activated nearly simultaneously (the result of a faster MF, for instance), the trajectory that is modified by

the perturbation Δt is that of the two cells rising in tandem. This difference, in general, is minor for only two cells, as there are delays in the production, diffusion, and transduction of u. Diffusion, though, is linear, and activating more and more cells, even partially, leads to more and more u. It is typical, therefore, for there to be systems where a cell can achieve high a production if the MF is slow and it is activated alone, but no cell can achieve that state if 7 neighbors are activated nearly simultaneously by a fast MF. This model feature is closely tied to the particular (linear, arbitrary) functional forms chosen for transport and decay, so we chose not to investigate it in detail. The fundamental physics it represents may be of considerable interest in the future, though. It is a representative of a class of behaviors related to proneural cluster size, which may be of biological relevance in this or another neural fate system. Investigating it in any useful way would almost certainly require a more detailed model of genetic interactions than the present one.

Results

Here we will address the results of the parameter scan as they pertain to the quality of 1-cell predictions of 2-cell behavior, the quality of 2-cell behavior in describing the behavior of 7-cell uniform, isolated clusters, and the how well 2-cell behavior informs the even-less-ideal case of patterning in randomized cellular epithelia, given a pre-existing template. The parameter scan was based two sets of 6400 parameters chosen as follows. We chose a reference parameter set for equation (1) p_{ref}, and $p_{static,}$ representing parameters we intended to vary and those we intended to leave fixed:

$$p_{ref} = \begin{cases} A_a = .65 \\ B = 1 \\ G = 1 \\ S_a = .65 \\ U_a = .00065 \\ \tau_s = 2 \\ A_s = .5 \\ \tau_u = 4 \\ A_u = 1.2 \\ D_u = .5 \end{cases}, p_{static} = \begin{cases} n_a = 4 \\ n_s = 4 \\ n_u = 12 \\ m_a = 4 \\ p_a = 12 \end{cases} \quad \textbf{(8)}$$

Using random numbers (x) distributed exponentially according to the distribution in equation (9), and multiplying them by the values in p_{ref}, we generated test parameter sets.

$$p\left(\ln\left[x / x_{ref} \right] \right) = c$$
$$.25 < x / x_{ref} < 4 \quad \textbf{(9)}$$

There were two exceptions to this rule. τ_s we chose from a uniform distribution with minimum .5, and maximum 6, and for τ_u we used an expanded distribution of the type in equation (9), where the maximum variation was a factor of 8 up and down, instead of a factor of 4. We examined each parameter set for 1) autonomous *a*-*s* bistability, 2) a lack of autonomous *a* bistability, and 3) an ability to prevent activation of the *a*-*s* switch in neighboring cells. If a parameter set had these properties, we kept it, and we did this until we had accumulated 6400 parameter sets.

These parameters were further winnowed down after doing 1-cell simulations to those exhibiting not just the desired bistable behavior, but also any possibility of

accessing the high steady state, given sudden *h* activation. For most of the studies presented here, we decided that Hill coefficients of 12 for inhibition-related processes were probably very high, and reduced these parameters to 8. This resulted in some previously functional parameter sets becoming uninteresting. We subjected each parameter set to several tests. We integrated the dynamical equations for a single cell, using standard Runge-Kutta integration (as included in MATLAB in the function *ode45*) according to equation (2), with *a* for cell β fixed at zero, and using p_c=7, for values of u_{ns_α} ranging from zero to 1.2*U_a, noting when that cell crosses the separatrix, and keeping track of the amount of *u* it has produced (for calculating T_u). We discuss this in more detail in Appendix E.

For parameter sets that could access the high steady state, we then pursued 2-cell simulations according to equation (2), and empirically mapped out the Δt required to satisfy the equality conditions for equations (4) and (5) as a function of u_{ns_α} and u_{ns_β}.

For 7 cell simulations, we no longer needed to use the parameter p_c, which was introduced to make the 1- and 2-cell simulations applicable to larger geometries. For each parameter set, we generated 150 randomized 7-cell rosettes. We set all of the elements in $D_{n,n'}$ for this geometry to 1, and used the geometry of the cluster only to determine 1) the position of each cell with respect to the movement of the MF, and 2) as an input to the function used to determine u_{ns} for each cell. This function was based on locating two R8 cells separated by 8 cell-cell distances at an adequate distance from the cluster such that no cell in the cluster would be completely inhibited. This produces a more-or-less smooth gradient of inhibitor within each cluster decreasing from “posterior” to “anterior.” We integrated these equations until a definite end-state was reached, and

recorded which cells had become permanently activated at that point. We used 11 different front velocities for each parameter set ranging from very slow to very fast (.02-2). This gives 150*11=1650 independent integrations on 7-cell clusters of each parameter set.

Lastly, for each parameter set we generated 8 distinct 192-cell simulated epithelia, with randomized cell locations and $D_{n,n'}$, as discussed in Appendix D. Given two permanently activated R8 template cells, and the steady state distribution of inhibitor they generate as initial conditions, we integrated these systems to stable endpoints with the same range of MF velocities as for 7-cell clusters, using a stiff ODE solver (*ode15s* included in MATLAB), and recorded the outcome of each simulation. The periodic boundary conditions used in these simulations mean that each grid gives 2 roughly independent proneural clusters, so each parameter set is subjected to 2*8*11=176 trials in this geometry.

The predictability of 2-cell behavior from 1-cell behavior, and 7-cell behavior from 2-cell behavior is remarkable. Figure 28 summarizes the former, and Figure 29 shows a specific example. We present no figure illustrating 7-cell behavior compared with the predictions from 2-cell behavior, as the fraction of parameter sets showing a better than 90% chance of predicting the correct fate of every cell in a 7-cell cluster varies between 90%-95% over a wide range (.02-2) of front velocities. The parameter sets that did not meet this high standard appear sporadic, and we have seen no evidence of this aspect of the model breaking down in a concerted way over the scanned range.

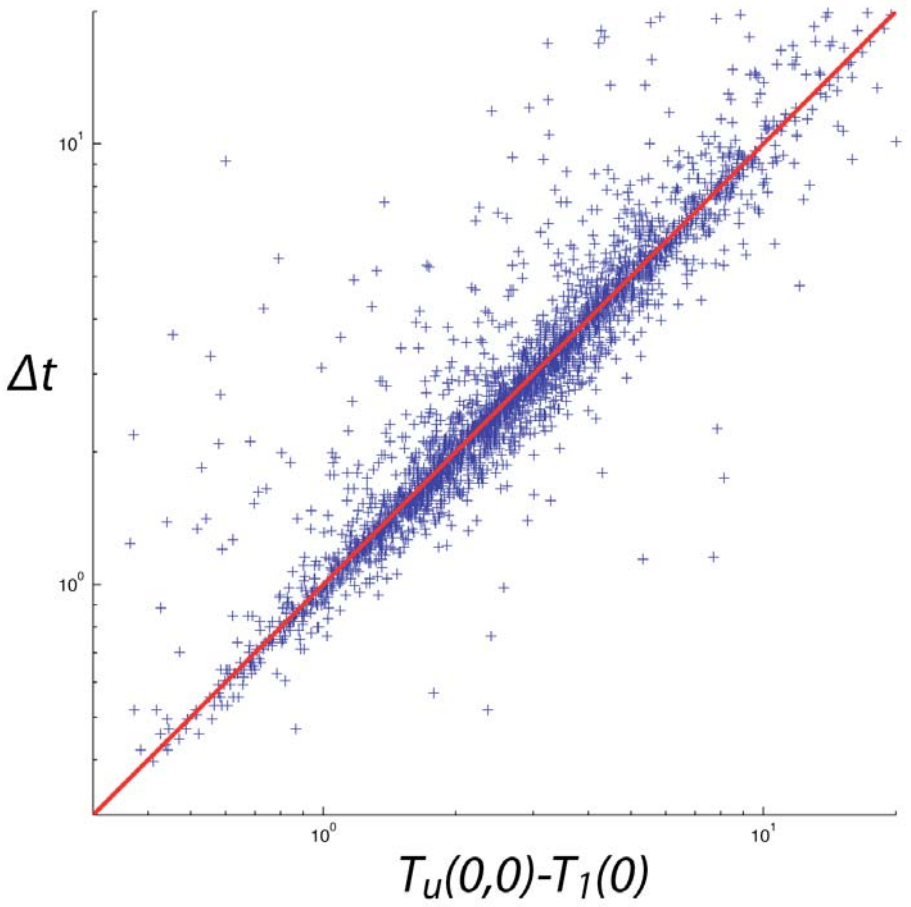

Figure 28: Correlation of empirical 2-cell critical Δt and those deduced from 1-cell simulations. This figure shows the results of the parameter scan as the relationship between the critical Δt needed for one or the other cell to win, as found by simulating a pair of cells at zero inhibition, and the same quantity calculated from one-cell simulations and using calculated thresholds. There is some spread, but the identity of these values has not been broken in any concerted way over this parameter regime. This shows that the close relationship between 1-cell and 2-cell behavior is quite robust to parameter variation.

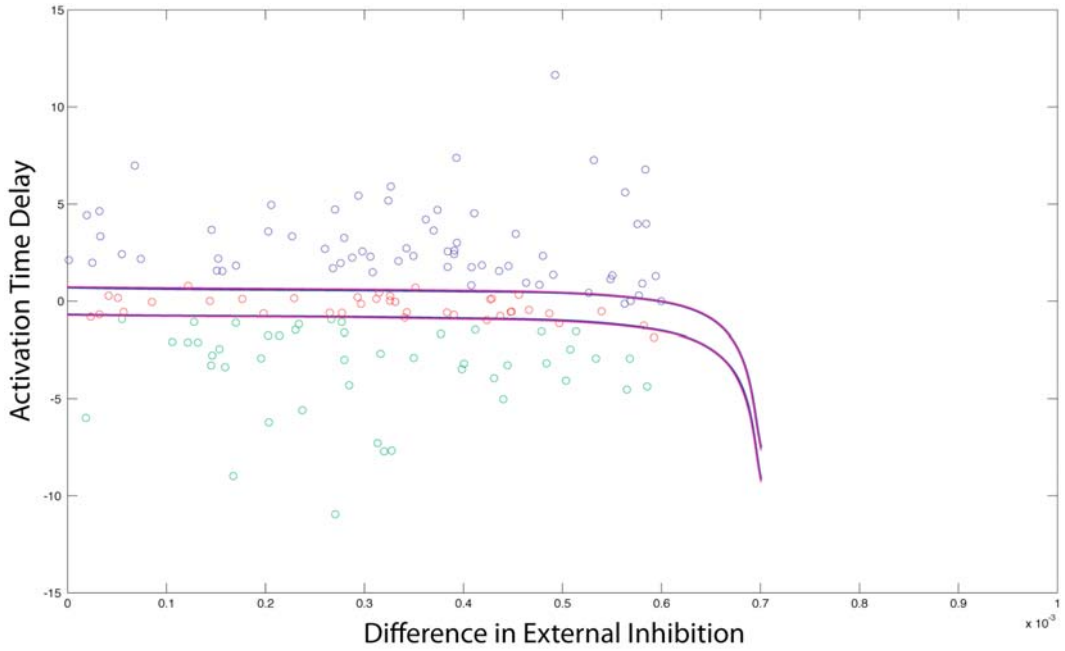

Figure 29: Predictions and observations of outcomes for a seven-cell cluster. This figure synthesizes the results of comparing 1-cell predictions to a 2-cell system, and 1- and 2- cell predictions to 7-cell systems. For this particular trial, we used a parameter set that patterns well, given a slow MF, and gave it a significantly faster MF, so that the quantity of twins produced would be meaningfully tested. The *x*-axis represents the external inhibitor experienced by cell β; cell α experiences none. The y-axis is Δt, the time cell β is first activated if cell α is activated at $t=0$. There are actually two pairs of lines on these axes, but they overlay each other very closely. The red lines represent our calculation from equations (4) and (5) of the Δt values that form the boundaries between different outcomes using T_1 and T_u from 1-cell simulations. On the upper half, and to the right of the graph, cell α alone becomes an R8. On the lower left, cell β, alone, does. Between the lines, both are predicted to be activated. The blue very lines represent the same boundaries, but empirically calculated by simulating 2-cell systems. The agreement, for this parameter set, is obviously very good. The points graphed on these axes each represent the interaction of the first two cells in a randomly oriented and position-randomized 7-cell rosette to receive an activating signal. The blue markers show a victory for cell α, the green ones for cell β, and the red ones represent observed twins. Again, the agreement is very good.

The approximations involved in jumping to a randomized 2D epithelium are much more extreme, since the individual diffusion constants between cells now vary substantially, and cells in a cluster are not equivalent in other ways influenced by geometry. Looking at parameter dependence over the scanned range for these simulations is more revealing, though the physics described above is still remarkably robust. The specific findings are discussed at some length in the captions to Figures 30, 31, and 32. We find, essentially, that the random parameter search encounters two regions of model failure at slow front velocities. The first is most interesting, and involves an increase in errors of all types (R8s gained, lost, and moved) correlated with the parameter changes that increase the strength of cell-cell interactions, namely large D_u and small U_a. This is, in fact, what we expect, considering that our quantitative understanding of individual cases is based on cells not interacting until a sudden threshold-crossing event. The second model failure involves finding marginal cases: Those parameter sets that barely met the requirement that they can inhibit their neighbors effectively. Given the finite and fairly large variation in coupling on a randomized lattice, we expect a good fraction of these marginal parameter sets to give bad results when we make predictions using D_u for all couplings, a result of using $D_{n,n'}=1$ for all the pairwise calculations.

Figure 30: The results of a parameter scan of simulations done on 192-cell randomized epithelia at low front velocity. The axes show the relative insensitivity of cells to inhibition (U_a, x-axis) and the diffusion constant, D_u, of models defined by individual parameter sets. In total, there are 3400 markers on this graph. Blue pluses indicate parameter sets where the exact correct outcome of a proneural cluster of four cells, as defined in the text, was observed in more than half of 16 trials (2582 parameter sets). Green triangles represent parameter sets where errors were more frequent than that, and the majority involved too few cells being activated (301). Red circles represent cases where the majority of errors involved more cells being activated than predicted (473). Magenta stars show the unique case of large numbers of errors occurring, but no net change in total cells activated from the prediction (44). Simply graphing the parameter sets on these axes reveals 1) the considerable robustness of two-cell predictions as applicable to randomized epithelia, and 2) two modes of failure of the theory. If we look at the points representing model failure, it is clear that they fall into two clusters: One in the upper left that consists of all three error modalities, and one in the lower right that primarily consists of simulations that specified more R8s than predicted. The upper left cluster of errors is explained as failure of the physics assumed in our model. High D_u, and low U_a have the effect of increasing the strength and speed of the dynamic inhibitor exchange that goes on within a cluster. This can lead to complicated dynamics, and we expect it to have a generally randomizing effect on observed outcome, which agrees with the observation of all potential error species, here. Parameter sets with low D_u and high U_a, on the other hand, are marginal with respect to the requirement that a cell be able to inhibit its neighbors. Introducing variation in local D_u can send individual pair-wise interactions into ranges where a cell either never inhibits its neighbor successfully, or does so much later than expected by a model that assumes fixed, uniform D_u, resulting in more R8s.

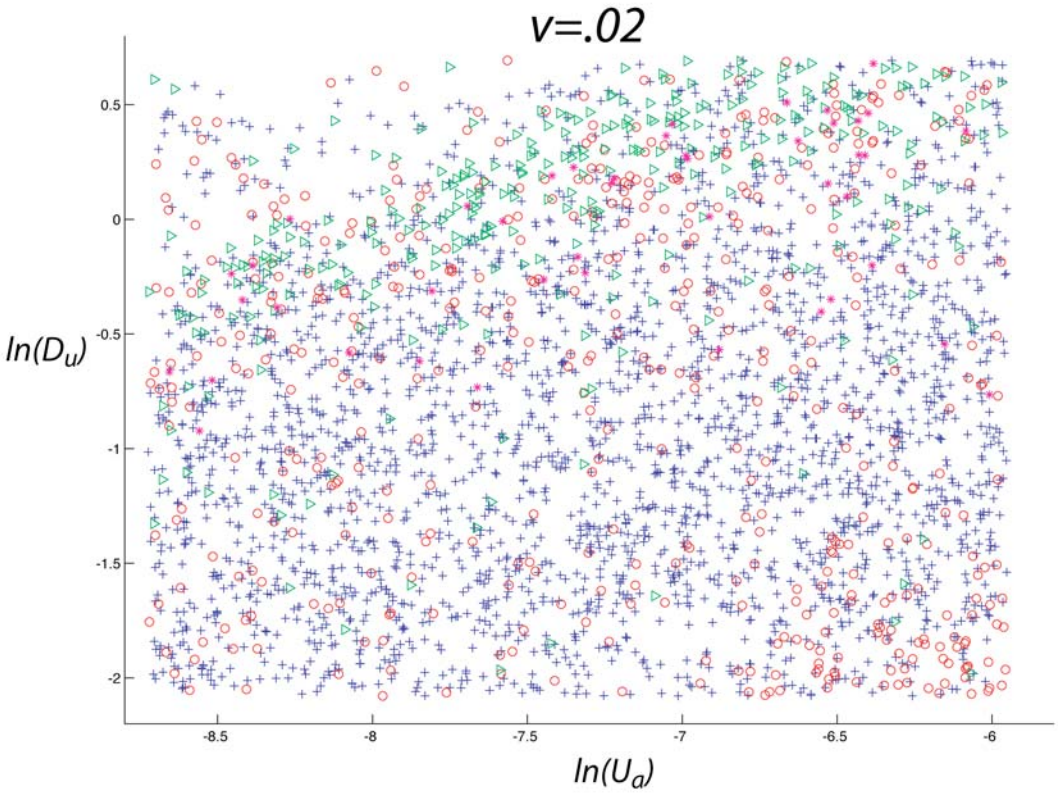
v=.02
0.5
0
-0.5
-1
-1.5
-2
ln(D_u)
-8.5
-8
-7.5
-7
-6.5
-6
ln(U_a)

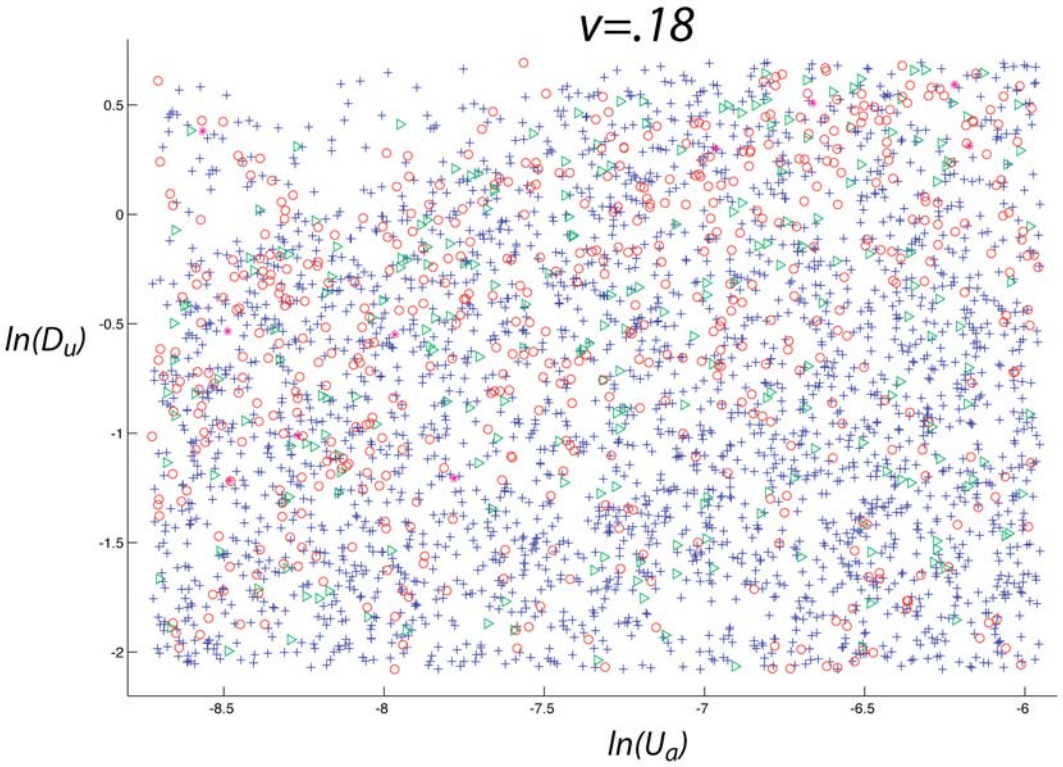

Figure 31: The results of a parameter scan of simulations done on 192-cell randomized epithelia at higher front velocity. The color-coding of this figure is the same as in the previous one, but there are 3362 total markers, of which 2583 are blue pluses (parameter sets making good predictions), 228 are green triangles (parameter sets where a two-cell analysis overestimates the number of R8s), 541 are red circles (underestimate R8s), and 10 are magenta stars (quantity of R8s is right, location is wrong). The distinction of the error clusters has been reduced, here, and the lower right error cluster has basically disappeared. As the front speed increases, we expect more cells to become R8s. As some proneural clusters saturate, with all cells becoming R8s, the predictions (of exactly this behavior) will become more accurate. This explains the disappearance of the lower right error mode. The broadening of the model failure in the upper left can be predicted (if not understood in detail) from the fact that our understanding and predictions are based on 2 cells interacting. At larger numbers of interacting cells (a faster front, for instance) it becomes less accurate.

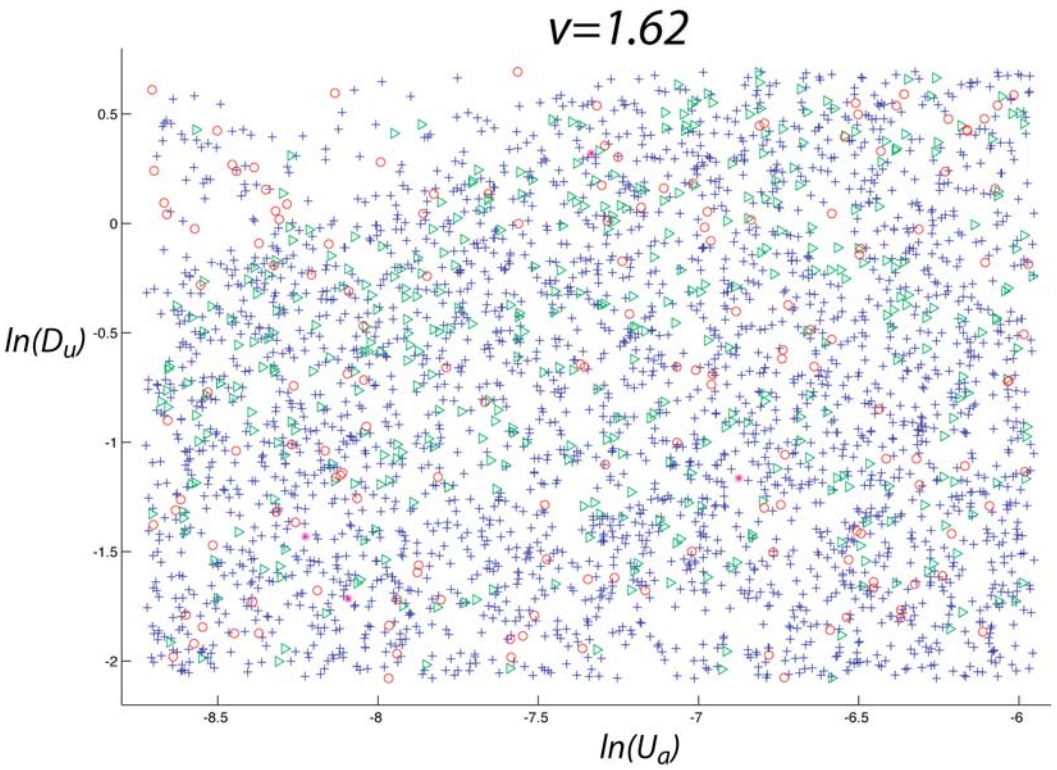

Figure 32: The results of a parameter scan of simulations done on 192-cell randomized epithelia for a very fast front. The color-coding of this figure is the same as in the previous two, but there are 3213 total markers, of which 2657 are blue pluses (parameter sets making good predictions), 396 are green triangles (parameter sets where a two-cell analysis overestimates the number of R8s), 156 are red circles (underestimate R8s), and 4 are magenta stars (quantity of R8s is right, location is wrong). This shows the breakdown of pattern formation, (most of the blue pluses represent every cell activated), as well as any meaningful interaction between these parameters in this range and error production. Notice that the this figure and the two preceding, represent the two limits of pattern formation as outlined in the previous chapter: Good, steady, 1-up patterning, and a uniform, undifferentiated front of activation. The additional distinction, here, is that there is additional parameter dependence that determines the predictability of the pattern selected in 2D.

Specific Predictions

In this section we have developed a theory of the behavior of a mathematical model based on genetic interactions in single cells. The scope of the theory, at this point, extends to groups of several identical cells, and has been applied to isolated proneural clusters in simulated epithelia. This theory is of considerable use for a few reasons. First, and most importantly, it provides a framework for understanding this system beyond the simple observation of outcomes of simulations. It is this system-level understanding that is the perennial goal of developmental biologists, and this is a significantly complicated system with several interacting signals.

So far, this understanding is of a formal mathematical model, and its predictions must be proofed against experimental results. It is no hollow theory, though: Any genotype that is sufficiently well understood to mathematize can be evaluated by it, and specific predictions made. The remainder of this section is devoted to discussing three specific cases of particular interest. First, the theory at this stage can explain the observation of stripes of R8s specified behind the MF under certain conditions. Second, we will compare this theory with the predictions made by a classical lateral inhibition picture. We will also examine its predictions of the outcome of an experiment in which groups of cells with predetermined neural fate are artificially introduced into the eye disc.

Striped Pattern Possible

One of the observations that drove early interest in this model of eye development was the fact that it could generate a propagating pattern of stripes parallel to the MF, where the lack of dorsal-ventral (DV) patterning in each stripe is recapitulated in the next. This was subsequently observed in eye discs. A parameter set capable of

producing a good, self-propagating hexagonal pattern is not typically capable of producing stripes, as it too-powerfully selects single cells, and the stripes break up. If inhibition is made "defective," however, self-propagating stripes can exist.

The easiest way to change a patterning parameter set into a stripe-forming one is to make *a* less sensitive to *u*, and make *u* dynamics slower. This destroys the hexagonal pattern of the original simulation, but given initial conditions that don't have any spatial pattern parallel to the MF, stripes can be observed.

In eye discs with a background knockout mutation in the *scabrous* gene, a poorly patterned array of R8s is specified. The key observation, here, was made when a temperature-sensitive allele of *Notch* was also bred into the flies. Over the course of retinal patterning, the incubation temperature experienced by the larvae was temporarily reduced to a degree that *Notch* function was destroyed. This transiently destroys the signal specifying the location of the next column of R8s, and many R8s are activated with little regard for position or density. Restoring the temperature, and thus *Notch* function, then causes the recapitulation of this stripe down the retinal field. Conducting the same experiment with N^{ts} and no *sca-* background yields a similar destruction of effective templating, but stripes don't form; instead, a random-looking pattern of single R8s does.

There are two main observations in the *sca-* disc that are pertinent to the current analysis. First, in all cases the *sca-* disc has more mutually adjacent R8s than seen in wildtype; an estimated 20% of R8s are specified as twins, even absent N^{ts} (49). Stripes can be considered an extreme expression of this R8 multiplicity. Second, stripes are reliably formed by stripes, but not from a disordered pattern: There is initial condition dependence of the stripe phenotype.

Examining the summary data from the two-cell analysis of various parameter sets reveals the origin of this phenomenon. For a given template, u_{ns} is fixed in every cell, and the critical delays for selection of a single cell from any pairwise interaction can be deduced. For a patterning system with effective, quick inhibition, the range of delays that will yield a twin for a given interaction is quite narrow, and most interactions resolve decisively in favor of one cell or the other. By making the inhibition slower and less effective, effectively increasing T_u, this range becomes much larger. This is very generic behavior, and the fraction of twinned cells increases, as does the failure of a regular hexagonal pattern.

The difference between a stripe template and a hexagonal template on cell selection is less obvious. The zone of complete inhibition around R8s is roughly circular, and so the arrangement of the first layer of cells that can possibly be activated as the MF progresses is scalloped for a hexagonal template. In this case, distinct proneural clusters are formed, and the most posterior proneural cells have, on average, a finite headstart over their closest competitors. Given a stripe template, however, the next closest adjacent cell is likely to be oriented parallel to the MF, at a very small time delay. Looking at a distribution of time delays for random pair-wise interactions given these two templates, then, we expect the distribution of delays for a hexagonal template to be more tail-heavy than that for a stripe template, though they are both symmetric about zero and have nearly the same domain, which is defined by cell size. This information is summarized graphically in Figure 33.

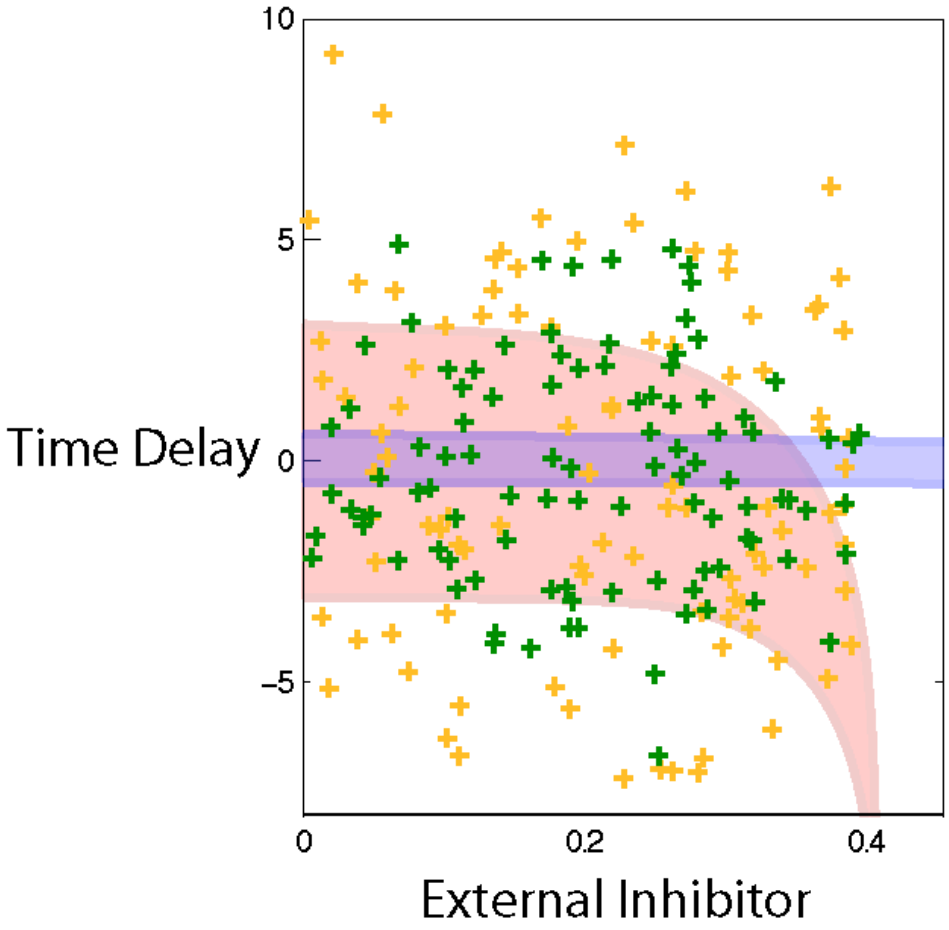

Figure 33: Summary of pattern v. stripe template analysis. In this figure, each cross represents the intrinsic properties (time delay and external inhibition) of a reference cell with zero inhibition and its closest competitor in a simulated proneural group. The shaded regions are where we expect, based on two-cell simulations, both activated cells to become R8s. The blue region represents a parameter set that gives wild-type-like results, whereas the salmon region represents a parameter set with a defect in inhibition that makes it effectively slower, and gives *sca-* type results. The yellow crosses are taken from simulated proneural clusters that are defined as they would be given a hexagonal grid of template R8s in the previous column. The green crosses are taken from a system with a stripe template at the same MF speed. Comparing the two distributions to the blue region shows qualitatively similar results. The large majority of cell groups are resolved definitively in favor of one cell or the other, with some being activated as twins. The difference between the patterned and the stripe template for the *sca-* parameter set is dramatic, though. Of course, a much larger number of cells are activated as twins given a patterned template, but most still are activated singly. But with the stripe template, the large majority of cells fall within the salmon region. This indicates that these cells will attain R8 fate in large contiguous groups: stripes.

For a parameter set that patterns well, the range of delays where twins are produced can be very small. Comparing this data with the distribution of delays generated by a hexagonal template versus a stripe template, reveals little: a marginal increase in a low frequency of twinning that may or may not be large enough to observe in experiments. For *sca-* parameter sets the situation is much more interesting. The behavior of interest is most pronounced when the range of delays resulting in twin formation is not simply sampling a narrow segment of the delay distribution near the peak delay frequency, but is separating the body and the tails of the distribution. Necessarily, in this case a significant number of twins are observed. Changing the template can dramatically change the frequency of twinning. For a parameter set showing a significant, but still distinctly minor, fraction of R8s as twins given a hexagonal template, the shift to a stripe template can change the vast majority to twins. This results in the specification of large contiguous groups of R8s: stripes.

Comparison to Classic Lateral Inihibition

It helps, in justifying work on a model, to have points of comparison. How does our model improve upon the standard? Does the standard model have some advantages? Can they be tested against each other by experiment? Etc. The standard theory of proneural cluster resolution involves Delta-Notch lateral inhibition. In this system, Delta is a membrane-bound ligand for the receptor, Notch, and they interact at the apposed membranes of the cells expressing them. Binding of Delta to Notch initiates a signaling cascade that results in increased Enhancer of Split (E(spl)) transcription factors in the nucleus, which, in this case, act as inhibitors of neural fate (62, 131). It is not the specific proteins or interactions that are different in this model compared to ours. The difference

is in the presence, in the textbook model, of an instability guaranteeing only one cell out of a group being able to sustain R8 fate (1-3, 13). This kind of interaction is easy to generate with the opposing-membrane, juxtacrine signaling described above. The equations below are an example of a simple modification of our model that effects this by having two inhibitors: One (*u*), that sets cluster spacing, and one (*v*) that resolves clusters.

$$\begin{aligned}
\partial_t a_n &= \left(\frac{a^{n_a}}{A_a{}^{n_a} + a^{n_a}} + B \frac{s^{n_s}}{S_a{}^{n_s} + s^{n_s}} \right) \frac{1}{1 + \left(\frac{\langle v_n \rangle}{V_a} \right)^{n_v}} - a_n + G \frac{h_n(t)}{1 + \left(\frac{u_n}{U_a} \right)^{n_u}} \\
\tau_s \partial_t s_n &= \frac{a^{m_a}}{A_s{}^{m_a} + a^{m_a}} - s_n \\
\tau_u \partial_t u_n &= \frac{a^{p_a}}{A_u{}^{p_a} + a^{p_a}} - u_n + D_u \sum_{n'} D_{n,n'} (u_{n'} - u_n) \\
\tau_v \partial_t v_n &= \frac{a^{q_a}}{A_v{}^{q_a} + a^{q_a}} - v_n
\end{aligned} \qquad \textbf{(10)}$$

Here, the operator $\langle v_n \rangle$ encodes the juxtacrine signaling that is a potent source of instability. It represents the sum of the secondary inhibitor *v* at all the cells adjacent to *n*, but not at *n*, itself.

$$\langle v_n \rangle = \sum_{n'}^{D_{n,n'} \neq 0} v_{n'} \qquad \textbf{(11)}$$

Proper tuning of the new parameters V_a, A_v, and τ_v makes the condition where two adjacent cells are both at the high-*a* state unstable, and this leads to significantly different bifurcation properties than the model of equation (2).

It is not our current goal to fully explain the range of behaviors possible in this new, more complicated model, but some limited studies have yielded results that are of interest.

The basic function of this model, as we have designed and parameterized it is the following. First, the *a*-*s*-*h*-*u* subsystem behaves exactly as explained previously. When cells near the high-*a* (now not necessarily permanent) state, they begin to produce the secondary inhibitor, *v*, relatively slowly. This inhibitor has no effect on the cell producing it, so an isolated cell is unchanged. If multiple adjacent cells are at the high steady state, though, they start aggressively inhibiting each other, and the high state becomes unstable in a supercritical pitchfork bifurcation. Unlike the trivial subcritical pitchfork bifurcation we dismissed earlier, this one is impossible to avoid: The cells have been focused to the high steady state, which is nearly independent of u_{ns}, and any headstart has lost its meaning at this point. In a physical system, it would be reasonable to say that the branch the system ends up following could be determined randomly. The two stable asymmetric steady states generated by the pitchfork bifurcation become more and more asymmetric as *v* builds up in the winning cell. Eventually these steady states annihilate the unstable states 0+ and +0, leaving only the two stable asymmetric steady states and the unstable symmetric steady state, as shown in Figures 34 and 23.

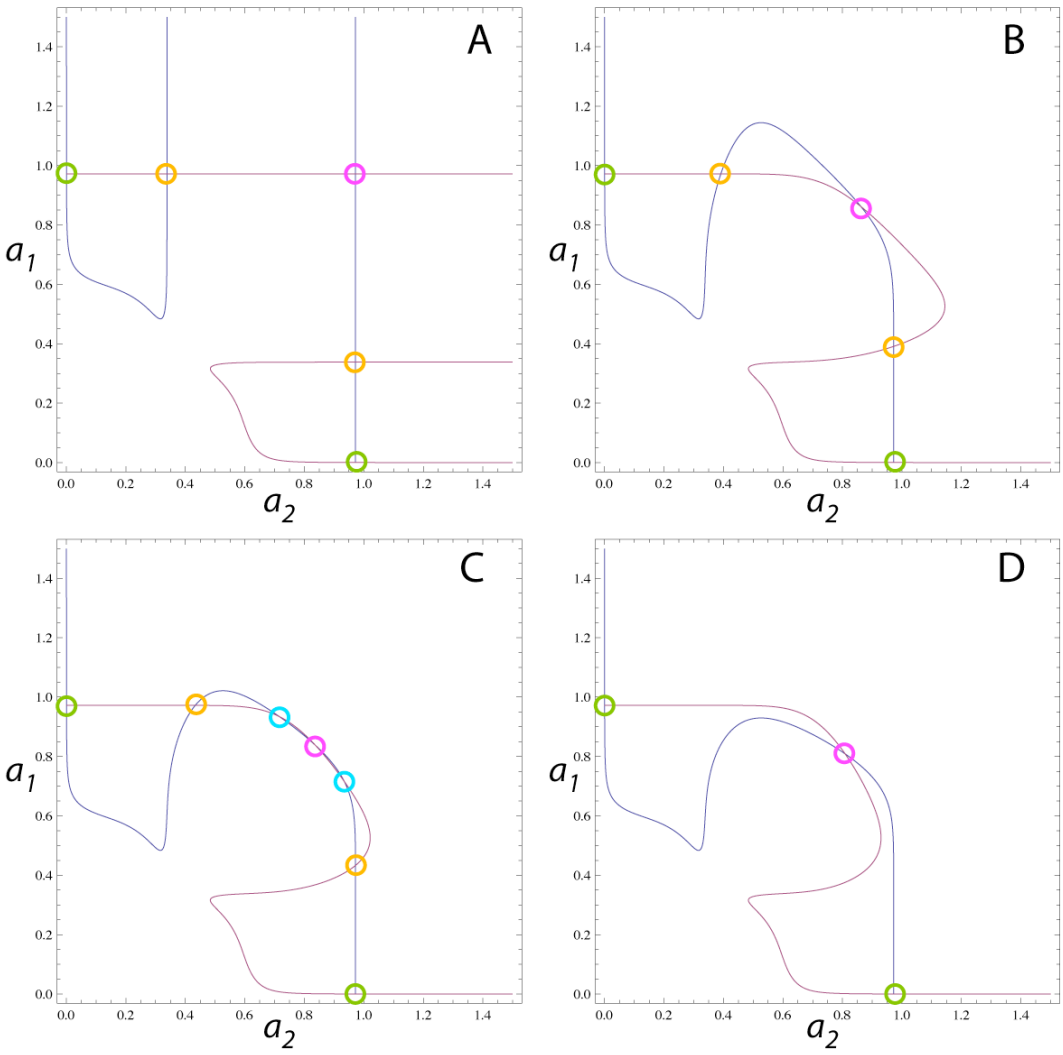

Figure 34: Nullclines for unstable symmetric high steady state in the 2-inhibitor model of equation (10). A) shows the nullclines for a system of two bistable cells experiencing full activation and v=0. In this system, we have added a secondary inhibitor v, with juxtacrine signaling capability. The other panels show what happens as this inhibitor slowly builds up, which we simulate by incrementally decreasing V_a. B) At high-but-finite V_a, the situation remains largely unchanged in terms of steady states. C) Eventually, the ++ steady state can go through a supercritical pitchfork bifurcation, becoming unstable and spawning two asymmetric stable steady states (cyan). D) As V_a decreases, the new asymmetric steady states annihilate the +0 and 0+ saddles in saddle-node bifurcations, leaving only the saddle at ++, and the stable large-amplitude asymmetric steady states at +- and -+.

With parameters chosen to permit the behavior described above, this model is incapable of producing twins. Thus, it is also incapable of producing stripes. This means, definitively, that this is not the process going on in *sca-* discs. It cannot be excluded from WT discs, at this point, and may well apply in other neural fate specification systems. It is almost certainly not important for eye disc patterning for another reason, though. This system prevents twins, but twins weren't a big problem in the simpler model, more of an incidental finding. In destroying twins, it resolves potential twins randomly, with no regard to the template or choosing the "correct" cell. This is template-destroying. Perhaps for twins this isn't a big deal (see the next chapter), but if the cluster is randomly resolving to a single cell from amongst 3, 4, 5 or more equivalent possibilites, much of the template information is lost in a single step. It seems reasonable to suspect that even if such a mechanism exists, it is not *used* except infrequently, even in WT discs. This is analogous to the situation discussed earlier in the chapter where an unstable state can only be considered important if trajectories pass nearby with any regularity.

Behavior Near Neurogenic Clones

An experiment that gives dramatically different results for our model versus a lateral inhibition-containing one is, fortunately, a simple one. A common technique in *Drosophila* genetics is to use the FLP-FRT system to introduce clones of cells with a targeted gene knocked out (133). The larvae in this case are mosaics of two genotypes, and very informative. Here, we consider mosaic larva eye discs that have a clonal boundary separating WT cells on one side from cells that are guaranteed to become R8s

(a neurogenic clone, with LOF mutations in *E(spl)*, for example) running through an individual proneural cluster.

In this situation, the proneural cluster cells in the neurogenic clone will become R8s, regardless. What is in question is the fate of the WT cells. In a classic lateral inhibition situation, it is obvious that the guaranteed winners in the cluster will suppress the WT cells in the cluster. In our model, however, R8 fate is permanent, and determined by processes outside the proneural cluster: The MF and the template of the previous column of R8s. If these processes select a WT R8 naturally, that cell will still be selected in addition to the ectopic R8s in the clone, provided the dynamics of their differentiation aren't too perturbed by the mutation. If the "natural" cell happens to be one of the ones in the neurogenic clone, there will be no visible difference in outcome between the models. Thus, our model predicts that there will be R8s specified arbitrarily close to a neurogenic clone, but still outside it. The textbook theory predicts that there will never be R8s any closer to a neurogenic clone than the width of a proneural cluster. Our theory additionally predicts that there will be a polarity to this effect with respect to the relative orientation of the clonal boundary to the MF. These predictions are currently being tested. The first, it is safe to say, has been confirmed (31).

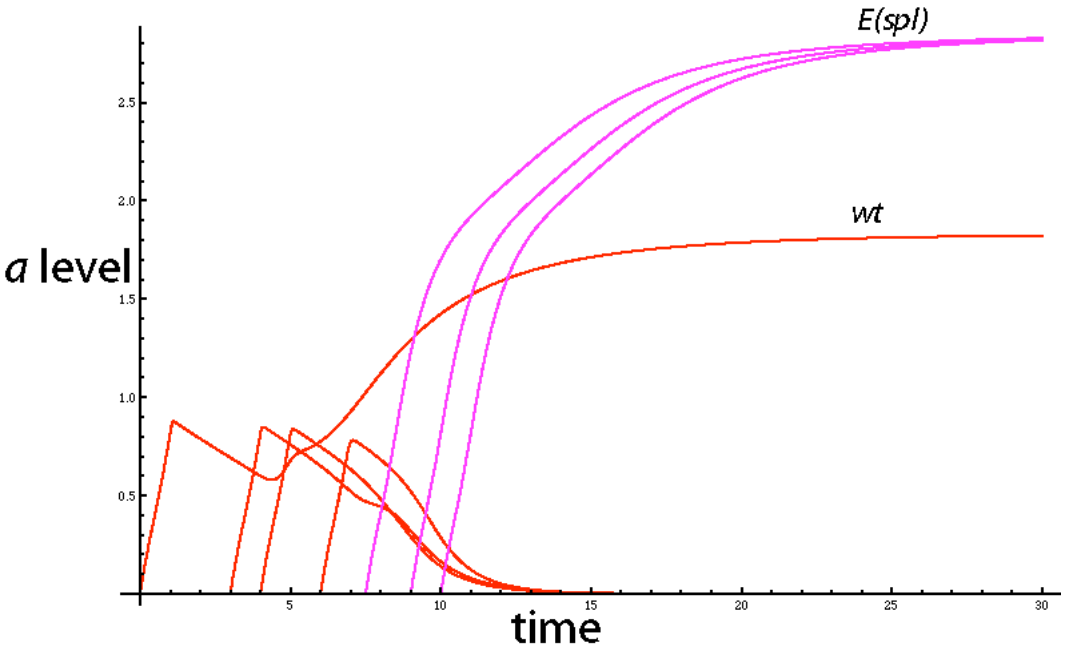

Figure 35: Trajectories of a in seven cells incorporating a neurogenic clone. In this graph, each line is the trajectory of *a* for a cell in a seven-cell proneural cluster. The red lines have a "wild-type" genotype, whereas the magenta ones are a "neurogenic clone," where a mutation has been introduced rendering them immune to the action of *u*. It is clear that the neurogenic mutant cells will become R8s regardless of what else happens. Due to the permanence of R8 fate in this model, and the selection of cells by a combination of inhibitor template and timing derived from geometry, it is possible that WT cells in such a cluster will also become R8s, if they are selected early enough.

Chapter IV:

Long Range Patterning

Thus far, we have discussed a model of R8 specification based on genetic interactions and addressed its ability to form self-propagating, stably patterning solutions in 1D, and the generalizations required to analyze cell selection in small sections of 2D epithelia. The last stage of the multiscale model involves using knowledge of a cell-selection subsystem to predict long-range patterning behavior. In this section we will largely abandon continuous time, and examine the question, "Given an epithelium and an initial pattern of R8 cells arranged in a column, what will be the pattern of cells in the next column? And the next? And the next?" The answer to this question should inform the distinction between the regular pattern-forming WT parameter sets and the disorder-producing *sca-* ones. The knowledge will be more powerful than that, however: It will necessarily be a theory of the production of pattern errors, their persistence, resolution, and propagation. In this section, I will first discuss what patterns we see in eye discs stained for Senseless (which corresponds to R8 fate). Then, I'll discuss the model formalism we have developed to facilitate the study of long-range patterning, and some preliminary data from applying it to simulations. Lastly, I'll discuss some applications of this model formalism to specific biological questions of interest.

Order in the Eye Disc

The ordering of the R8s of a developing eye disc (hexagonal, stripe, or basic lack-of) is easy to detect with our own eyes. Human sight is legendary, when it comes to pattern detection, for both its ability to detect subtle order, and to misjudge it. To address patterning at the scale of a whole eye disc, or a large section thereof, we should look at the patterns formed with more quantitative rigor. We have examined eye discs of several genotypes immunostained for Senseless, and imaged by confocal microscopy by our collaborators in Nick Baker's lab at Albert Einstein College of Medicine (31). We processed these images with an automatic method for identifying the locations of *senseless*-expressing cells, and registering them with a local coordinate axis representing rows and columns, or the direction of progression of the MF. Since some of the genotypes we deal with involve temperature sensitive alleles, or heat-shock promoters, it sometimes made sense to divide an eye disc into distinct regions representing pre- and post-restrictive temperature regions. We did this manually, and treated these regions separately. Given the positions of nuclei from R8-specified cells, we attempted to evaluate their arrangement in space in a principled way.

To detect hexagonal and stripe ordering in an array of R8 cells, we used the orientational order parameters $\left\langle e^{6i\theta} \right\rangle$, and $\left\langle e^{2i\theta} \right\rangle$, respectively, where the angle, θ, was defined in relationship to the local direction of MF progression, and represents the angle formed by the vector separating two cells and the local coordinate axis. Rhe averaging was done over cells defined to be neighbors by a criteria based on separation distance (134). The regions containing R8s are often not very large, and frequently have very elongated shapes, making edge effects quite significant. For this reason, we needed to

compare the order parameters observed for any given eye disc not with zero, but with relevant null hypotheses based on the geometry of that disc. Generating null hypotheses involved defining a region of interest, counting the cells in it, and then repopulating an identical region with that number of cells according to some ordering rule. The first null hypothesis we used involved liquid-like ordering, in which cells were not densely packed, and had a circular zone of exclusion about their centers. Populating a defined region according to this rule is simple: Pick a random location, if it is far enough away from all the other cells that have been placed so far, accept it, otherwise, reject it and repeat. A rule for a stripe-like hypothesis is similar, but with the addition of a sinusoidal function modulating the maximum probability of acceptance as a function of a cell's displacement in the direction of MF progression. Radii of exclusion and stripe separation were taken from image averages. Appropriate hexagonal patterns are significantly harder to generate, so at this point we treated hexagonal patterning as a classification of exclusion when a system is compared to the other two patterns. Any number of specific manifestations of the null hypotheses for a given geometry can be generated, and order parameters calculated. The distributions of these order parameters in the complex plane provide the basis for reference that the measured order parameter for the actual arrangement of R8s should be compared against. This works marginally well for classifying stripes. Indeed, for experimental results where the stripe-forming behavior is somewhat messy, without large continuous stripes, the overall ordering can still be detected by order parameter when it might not have been by eye, as in Figures 36 and 37. In other cases it works less well than our intuition would suppose, as in Figures 38 and 39.

Figures 37 and 39 show the summary data that this analysis provides for two eye discs with transiently destroyed templating. In the first disc (Figure 36, analysis in Figure 37) the template has been temporarily destroyed by increasing Notch signaling via a heat-shock promoter-driven Notch intracellular domain, direct evidence of which can be seen in the broad stripe where no R8s are specified. The second disc (Figure 38, analysis in Figure 39) shows the action of the previously-discussed temperature-sensitive *Notch* allele that allows temporary disruption of R8 suppression. These genotypes, while they do similar things with respect to destroying template order in the DV direction, have clear qualitative differences. The orientational order parameters measure the average of local ordering in the locations of cells, and do not require a coherent long-range positional pattern to yield a signal. They are, accordingly, able to detect "stripeness," even in a system (such as the eye disc in Figure 36) where the stripes are broken apart and shifted over the pattern region, and not part of a single crystal domain. Analyzing such a pattern with a stripe-detecting orientational order parameter yields strong concordance with a distribution of test patterns generated from a stripe-forming hypothesis, and strong disagreement with test patterns generated from a disordered hypothesis. No notable hexagonal patterning is observed.

This type of ordering in the second, temperature-sensitive Notch phenotype is not as robust. Though at least a couple long, relatively contiguous stripes of R8s are visible in the eye disc in Figure 38, and the stripe-detecting order parameter for that system shows better concordance with a stripe hypothesis than a disordered hypothesis, the degree to which stripe hypotheses can be separated from a disordered hypotheses in this geometry, at this density, is not impressive. This is due to the fact that the stripes, here,

have some internal structure, and there is an overall excess of R8 cells. Indeed, a positional order parameter would work better for detecting the order in this disc, whereas it is unworkable in Figure 36. The need to use different pattern detection schemes for different genotypes giving related phenotypes suggests that the understanding of the pattern that inspired these detection methods is somehow incomplete, and should be reexamined.

Trouble arises in this type of classification when there are broad distortions to the underlying lattice. This complicates matters, as the eye disc is far from flat and even. While it is an epithelial monolayer, it is twisted and bent in 3D into a characteristic shape, and it is not clear how this affects the local patterning system (2). Secondly, for purposes of cell-location, we use nuclear staining, but the nucleus does not necessarily represent the "true" location of a cell compared to its neighbors very well. Third, and most fundamentally, R8 fate is fixed for a single cell, but the geometry of that cell's neighborhood is dynamic. The morphogenetic furrow is, recall, so named because it is a physical distortion in the epithelium, and it moves; it is also accompanied by changes in nuclear location within cells. These distortions are near their most highly dynamic when the patterning process is actively occurring (1-3,17,27-30). If we could characterize the distortions precisely, we could transform the system in such a way that isotropic order parameters provide an adequate measure of the pattern. Unfortunately, the only way we can see to arrive at an empirical understanding of these distortions, with the present data, would be to do something patently dishonest, like assume a final hexagonal pattern of the R8 cells, and calculate an effective local lattice based on that.

It is worth asking why stripe-detection by order parameter still works, at all. The explanation for this is that the direction of the stripes (parallel to the MF), is decoupled from the direction of maximum dynamical distortion (perpendicular to the MF), and that stripe spacing is considerably larger than within-stripe R8 spacing, making the order relatively insensitive to the exact distance range used to calculate neighbor interactions. For hexagonal order, there is no such decoupling; stretching any axis affects all other predicted spacings and angles for nearest neighbors. Additionally, the difference between cells associated at 90 degrees relative to an axis, versus 0 is dramatic, even with the levels of noise and uncertainty in the current system. The difference between 0 degrees and 30 degrees (equivalent maximum and minimum probability angles for hexagonal patterning) is much smaller, and higher-symmetry long-range order is just more delicate in such a finite, suboptimal system.

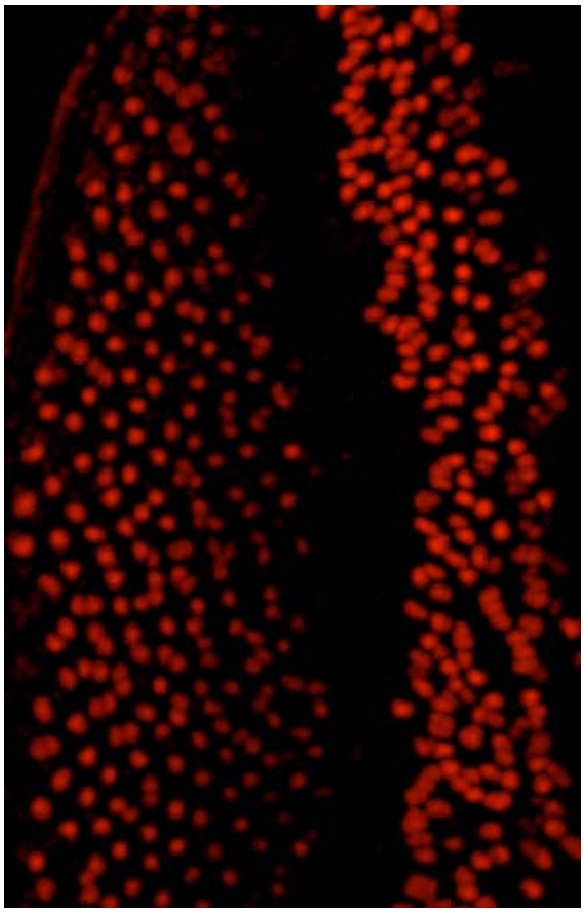

Figure 36: A *hs-N_{intra}, sca-* eye disc with Notch intracellular domain driven by a heatshock promoter. To generate stripes in this eye disc, instead of temporarily shutting down Notch signaling with a temperature-sensitive allele, Notch signaling was temporarily enhanced by driving a gene expressing the Notch intracellular domain (the transcriptionally active part) with a heatshock promoter. The temporary lack of any R8s being specified, at all, is visible in the center of the field. Incidentally, the portion of the eye disc on the left side gives a good idea of what the *sca-* phenotype looks like in terms of R8 specification. The post-heat-shock patterning seen in the stripe at right is difficult to evaluate, by eye. It appears that it may contain stripe-like order, but the stripes are broken and jumbled to a significant degree. Photograph courtesy of Nick Baker.

Figure 37: Ordering and null-model comparison for the eye disc in Figure 36. This figure shows the results of using a pattern-detection method based on the orientational order parameter, $\langle e^{in\theta} \rangle$, which is sensitive to the relative positioning of neighbors with regards to a local reference axis defined by MF movement. *n* is the order of rotational symmetry expected. In each figure, the blue pluses represent trials of a null model consisting of an identical number of cells observed in a region of interest arranged with liquid-like order. The red pluses represent trials of a null model representing cells that exhibit both local exclusion (as the blues do), and overall stripe-like positional order. The colored ellipses represent the regions containing 95% of the null model distributions, given Gaussian behavior. The green dot on each set of axes represents the orientational order calculated from the positions of the cells in the actual eye disc in question. A) shows the order calculations for the portion of the eye disc in Figure 36 that was patterned after the template-destroying heat shock. There is good separation between the striped and disordered null models, and the observation clearly falls within the order parameter predictions for stripes. B) shows the same system examined for six-fold ordering. As expected, there is little distinction between the striped and liquid-like null hypotheses. There is also no indication of excess hexagonal order in the eye disc. C) shows the pattern evaluation for the pre-heat-shock portion of the eye disc, which shows the unperturbed *sca-* phenotype. Testing for stripe-like order shows no disagreement with a disordered system. D) testing for 6-fold order shows, perhaps, a very slight amount of hexagonal patterning. This finding is not robust, at all, and even for wildtype discs, random variation and systematic lattice distortion stymie use of the *n=6* order parameter near the MF, where patterning is actively occurring.

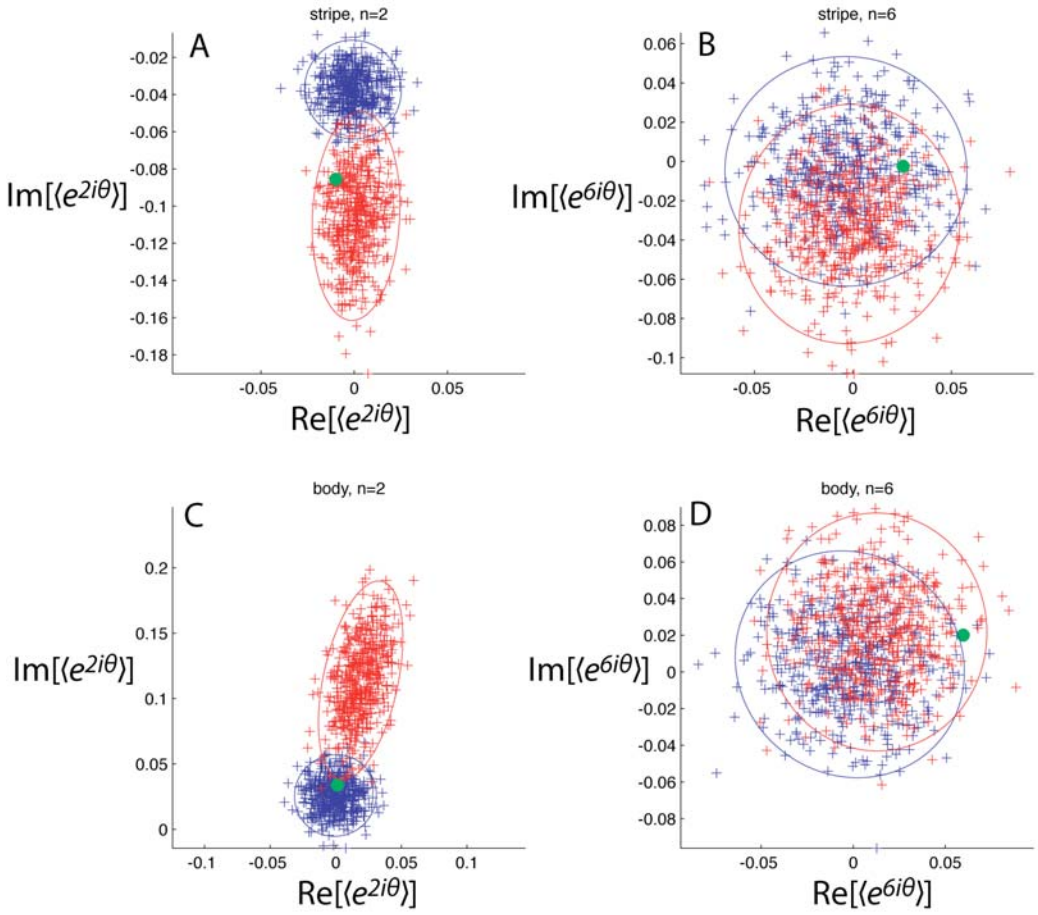
stripe, n=2
A
Im[⟨e^{2iθ}⟩]
Re[⟨e^{2iθ}⟩]
stripe, n=6
B
Im[⟨e^{6iθ}⟩]
Re[⟨e^{6iθ}⟩]
body, n=2
C
Im[⟨e^{2iθ}⟩]
Re[⟨e^{2iθ}⟩]
body, n=6
D
Im[⟨e^{6iθ}⟩]
Re[⟨e^{6iθ}⟩]

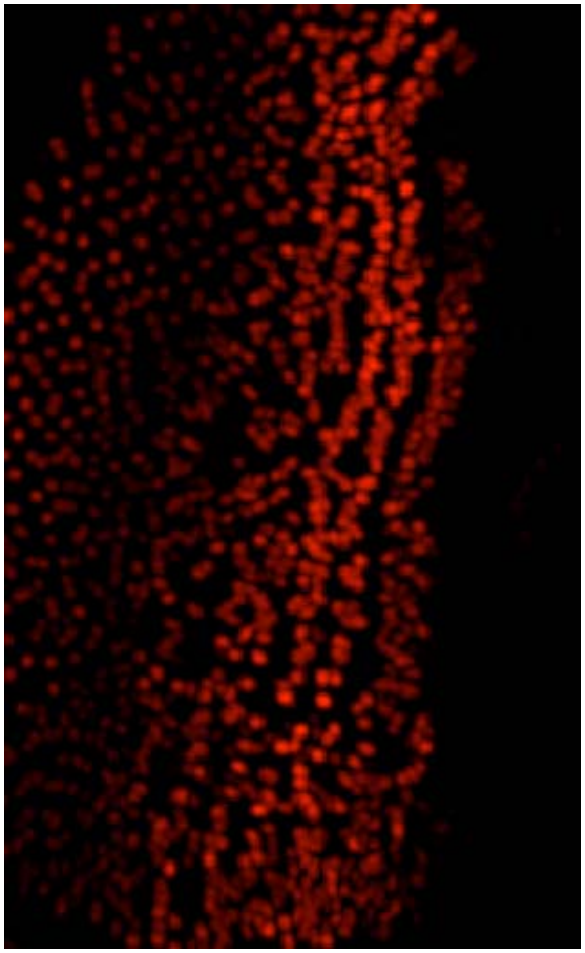

Figure 38: A *sca-* eye-disc with temperature sensitive Notch that shows a clear pattern of stripes. In this figure stripes were formed after Notch signaling was temporarily disrupted with a temperature-senstive Notch allele. Long, continuous stripes of R8s are clearly visible, but they have finite width, which complicates evaluating their order. Photograph courtesy of Nick Baker.

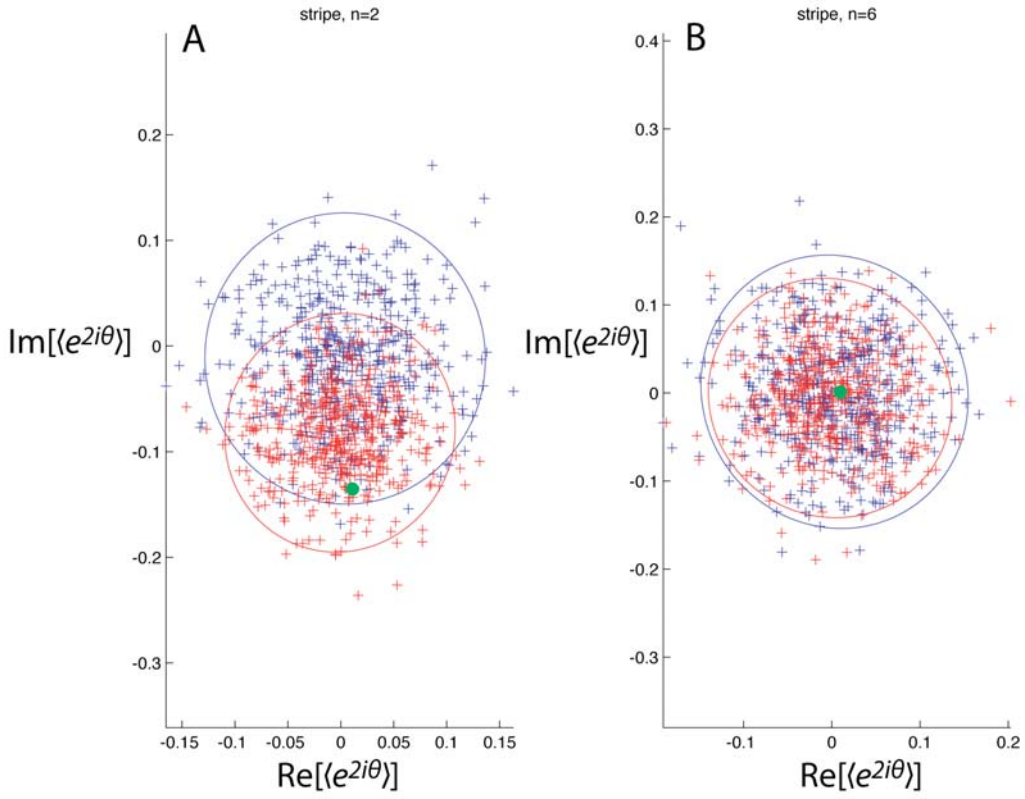

Figure 39: Ordering analysis of the eye disc in the Figure 38. In these graphs, which follow the same labeling convention as Figure 38, we examine the orientational order-parameters $\left\langle e^{in\theta} \right\rangle$, with n=2 and n=6 for the region of the eye disc in Figure 35 that appears to contain stripes of R8s. A) shows, somewhat surprisingly, and illustrative of the vagaries of comparing images of different eye discs, with different genotypes, that were fixed at different developmental times, is the fact that the null models based on liquid-like disorder and stripe-like positional order are not very distinct, according to the *n=2* order parameter. Nevertheless, the observed data in this eye-disc favors stripe-like order. B) shows the same data examined for 6-fold symmetry. There is none.

We decided, after examining this system and its properties, as discussed here, that perhaps the statistical-mechanics-inspired viewpoint of ordering was not the best way to examine R8 specification (though it is likely useful in other contexts). This is not, as we understand it, a thermal system where many particles interact and seek a minimum in some collective thermodynamic potential. Each column of R8s has a role in specifying the locations of the next, but, also, there is some variation that occurs in this process that is quenched into the pattern (1-3,49,50). In this viewpoint, the order of the pattern is contained in the process by which one column specifies the next. This iterative process can be understood without having to invoke true long-range order in the distorted eye disc. What order exists is imprecise, and the exact spatial order seen in adult flies arises later in development after cell rearrangements. For R8 specification, though, we have a new target. Previously we studied how an R8 cell is chosen by our model, now we will study whether that chosen R8 cell is the right one to extend the previous pattern.

Concept and Method

In dealing with a process that has fundamentally discrete time (column 1 specifies column 2. Column 2 specifies column 3: $t_1 \rightarrow t_2 \rightarrow t_3 \rightarrow \ldots$), a number of formal approaches exist. A finite epithelium of N bistable cells suggests the classification of its state as an N-bit binary number. If we consider a system that is always in a state where every cell can be classified, and these binary classifications are adequately precise (the MF moves slowly, essentially), then each state will lead to another, deterministically, and the system can be summarized as a deterministic finite-state machine. If cells can only make the transition $0 \rightarrow 1$, and not the transition $1 \rightarrow 0$, there will be terminal states that

"become" only themselves, and there will be source states that exist only *ab initio*. Since the system is deterministic, each state will only lead to one other. Furthermore, if the bits are ordered, and the fate of each bit is determined in order, each state will have only one state that leads to it: The overall structure of the system will be like a tangle of many separate strings. Of course, a finite state machine with 2^N states is a scary thing, and N doesn't need to get very big before our understanding of the system becomes hopelessly clouded. The goal, then, is to coarse-grain the system in a way that preserves all the detail we care about, and is simple enough to facilitate understanding (59,60).

This entire thesis has been about coarse-graining in one form or another. To illustrate the goals of coarse-graining the pattern-propagation system, let's look back on the simpler 1D system as a finite-state machine. On a finite 1D lattice, and given an MF moving from left to right, the number of distinct strings is simply the number of different initial conditions we allow. Fate determination rules applied at each step (each time step, in this case, is most conveniently defined as "when the next cell is activated") extend these chains until a terminal condition is reached. In the patterning system, cells that are far away from a cell currently having its fate decided by the MF have very little direct influence over this decision. It makes sense, then, to have the first simplification of the finite state machine be a reduced number of states representing only the range of states near the MF, effectively translating to a moving reference frame. The system is still entirely deterministic, so we expect no branching, but now paths from different initial conditions can coalesce, as the details of those initial conditions are "forgotten" by the reduced state space. Coalescing states can be taken to more extreme levels. If the implication of each transition is perfectly understood, along with the initial condition, no

information need be lost, but it is likely that the new, rule-based states have little direct resemblance to the detailed states of the full system (132). For purposes of understanding and explicating a system in which the rules are unknown, or at least not known in easily-summarized detail, the intermediate level of simplification seems most desirable. For the 1D system this hierarchy of simplification is illustrated in Figure 40.

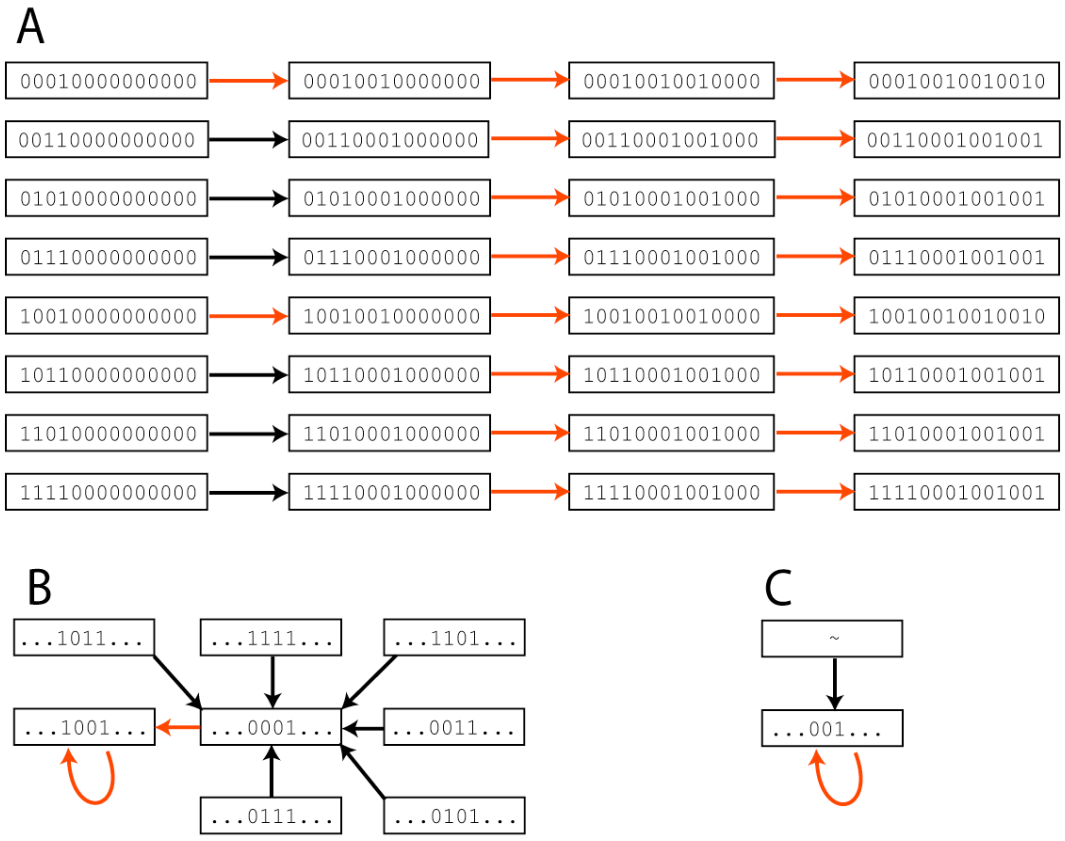

Figure 40: Coalescing a 1D patterning finite state machine. A) shows the deterministic evolution of 8 allowed initial conditions on a grid of 14 bits. The rule at work here is a simple threshold; if the two bits preceding the right-most 'on' bit are 'off', then the next two bits stay 'off,' while the third becomes 'on' (red arrows). Otherwise (black arrows), there are three 'off' bits followed by one 'on.' Since the machine is deterministic, and the entirety of the history is stored in the bit-string, the overall structure consists of parallel strings. B) this is the same rule applied to a moving reference frame (the bit most recently switched 'on' is always the right-most one in each state) in an overall field of unknown size. All but the most recent history of each state is "forgotten" at each step, and this machine is much easier to interpret as a single physical process. Even if we didn't know the different meaning of the red and black arrows (in this case, they refer most directly to the size of the frameshift at each step), we could read off many aspects of the system. To wit, it has a periodic absorber, and the general approach to that state involves a one-step transient through the state 0001. C) shows the maximum coalescence of this system, where we have redefined the states to match the rules (below threshold, not below threshold). Since we know exactly what the rules were, nothing has been lost. If, however, we didn't, so much detail has been lost, here, that it would be hard to back out the physics of the process.

The familiar branching structure of a Markov process arises when a system is probabilistic in some way. Our model can be quite complicated, but it is deterministic. In 1D we treated it as deterministic and regular, with a distinct spatial periodicity to the lattice. In 2D, however, we use a randomly generated lattice of cells, with interactions determined by the length of the interface between adjacent cells, as defined by a Voronoi tessellation (for more on the lattices, see Appendix D). For a patterning system in a moving reference frame, then, there are an infinite number of states and initial conditions, and the whole point of shifting to this viewpoint has been destroyed unless we can make a decision as to how to aggregate the states. In the process of this coarse graining, which involves reducing an infinite number of randomly generated states to a finite number of state-categories, the system gets a probabilistic interpretation that results in branching paths.

Given a propagating pattern, and asked which is the next cell that should be activated to extend that pattern, it is likely that there will be one or two cells that are, essentially, good enough. There will be many cells, and many more multiple-cell combinations, that are very, very wrong. There are likely to be several possibilities that do not fit well into either category: Cell selections that don't extend the pattern correctly, but don't totally disrespect it, either. In a patterning situation, the activation of the correct cells is favored by their interaction with the previous pattern. If a cell is specified in an egregious, pattern-destroying location (or locations), that bias for the correct cell to be specified in the next column is destroyed, and the situation now favors the specification of incorrect cells, which are far more numerous. Given that we aren't concerned with the specific random pattern generated by a system with a destroyed

template, it makes sense to lump all of the badly mispatterned states into one self-regenerating, disordered state. What remains to decide is how to treat the transition between the perfectly-patterned and the unpatterned states: The small but significant errors.

At one extreme, all errors can be treated as very important and treated in full detail, bringing us back to square one. At the other extreme, all errors can be treated as fatal, giving us a total of two states: good pattern, and no pattern. In between these extremes of overwhelming detail and triviality lies the ideal of physics-preserving coarse-graining. The "small error" states must be modeled in some detail: If they are close enough to the correct-patterning state that they can *lead back* to that state with any notable probability, they contain important physics. Treating them more casually can significantly change the interpretation of the patterning state, the non-patterning state, or both. How these important "small error" states are defined is dependent on the state-space loop we decide to call "patterning."

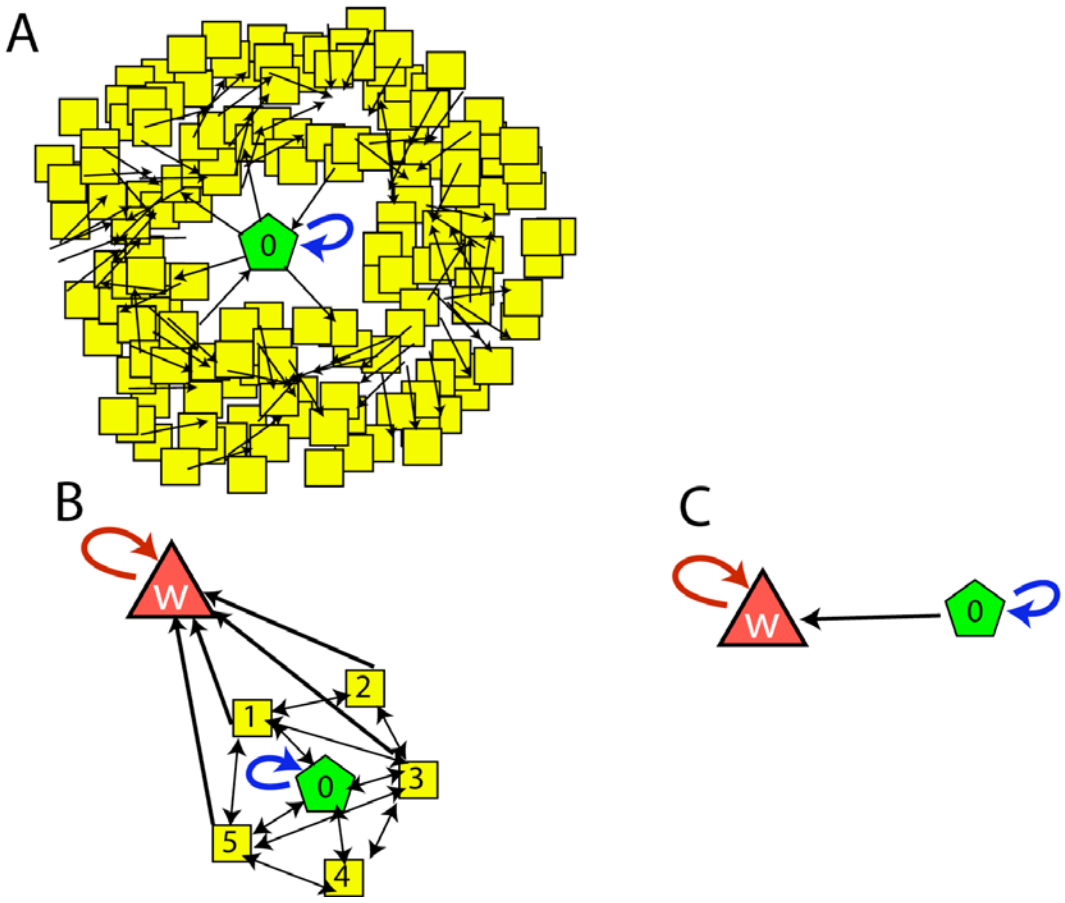

Figure 41: Coalescence of the 2D patterning system, schematic. A) There is one state in the patterning system that represents the correct, repeating pattern (state zero). In a 2D system, there are potentially very many states that represent an incorrect pattern (yellow squares), and they cannot all be treated in detail, lest the machine become hopelessly complicated. B) Using the assumption that a bad error will, in general, produce more bad errors (or at least be very unlikely to spontaneously produce a good pattern) we coalesce most of the error states into the stable, absorbing unpatterned state, *w*. C) In the most extreme case, all of the states except zero can be coalesced into state *w*. Our understanding of these processes is necessarily incomplete, though, and if we do this we have probably destroyed the detail that will provide a key to understanding the system. A machine more like 'B' is desirable.

It is easiest to make this concrete for a system specifying successive stripes of R8s. The perfect, self-regenerating state is that of a continuous, straight stripe. The obvious types of small defects include a cell missing from the stripe (a gap) and an ectopic cell present in addition to the stripe, but near it. These defects arise in different quantities for different parameter sets (averaging over many lattices; recall that the probabilistic interpretation arises because a new lattice is encountered every time we shift reference frame with the MF), and for different error conditions in the template. They can occur in combination, and since single errors only define three distinct states, we are capable of treating limited classes of multiple errors. See Figures 42 and 43 for a discussion of how these multiple error states are defined. The jump from the perfectly patterning case to the large-error state is possible, though it tends to be more likely if the system already has a small error in the template. An error-containing template, however, can lead back to the perfect stripe (or another small-error state) with significant probability. This would appear in a larger patterning system as a self-healing capability, or an ability to completely recover from finite size errors. This is observed in large simulations of stripes, and in eye discs expressing stripes of R8s, as shown in Figure 44.

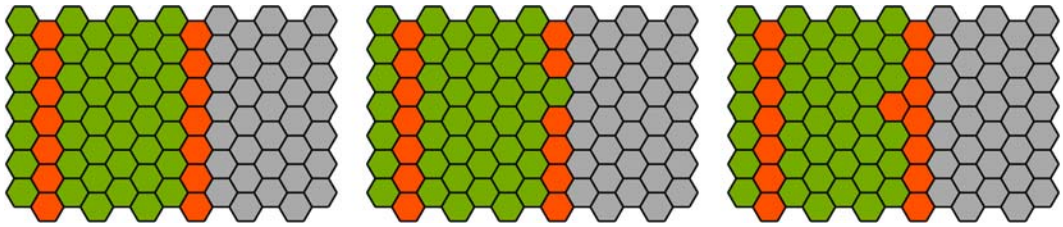

Figure 42: Basic stripe errors. A Perfect stripe, a gap, and an ectopic cell. More error states can be enumerated as combinations of unit errors. In this case the case of stripes it is simple to consider a state as leading directly to a new state, without going through a branching-recombining process with adjacent unit processes.

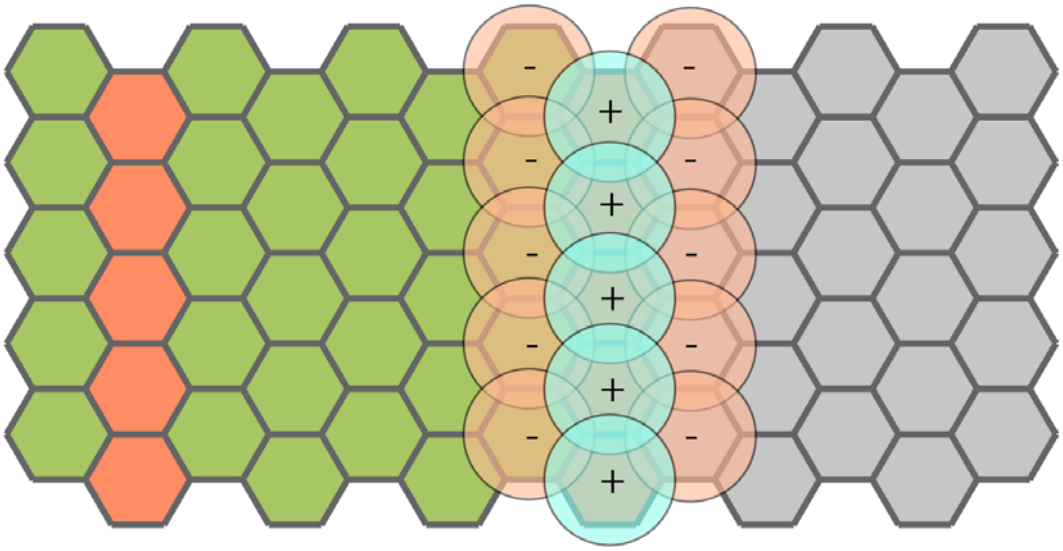

Figure 43: Schematic of stripe classification. On a 5 by *n* grid, we define a set of overlapping regions. The grid itself is randomized, in practice, and we do simulations on many hundreds of these randomized grids. The blue regions represent the predicted location of cells in a stripe, the red ones ectopic locations nearby. In actuality, the regions are rectangular and have much greater overlap than shown. We first try to assign cells to regions such that there is exactly one cell in each of the '+' bins. Any leftover cells are then assigned to '-' bins. Examining all possible arrangements with no more than one cell in each bin, each arrangement is scored by the number of errors; an empty '+' bin or full '-' bin counts as an error, and the overall identity of the state is defined as a linear combination of all the minimum-error states. There are 18 error states (and 1 perfect state) with 2 or fewer errors, and accounting for translation and reflection symmetry perpendicular to MF motion.

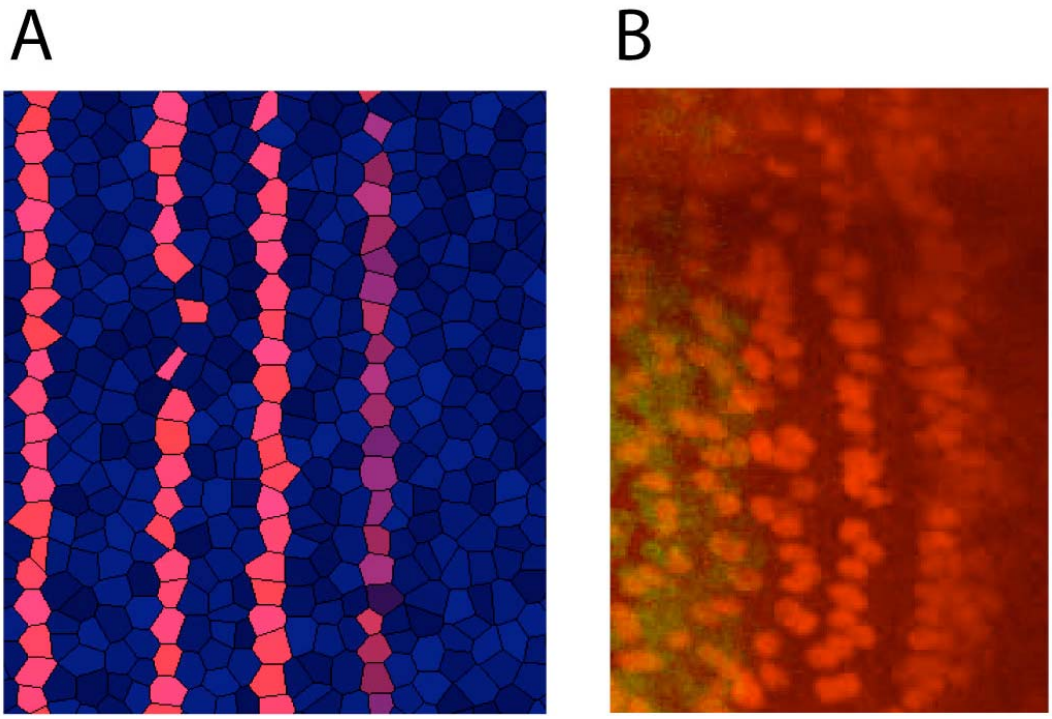

Figure 44: Simulation and eye disc showing stripes capable of significant self-healing. A) shows *s* for a simulation on a randomized epithelium with a parameter set that forms stripes. The initial condition was the full activation of the continuous stripe of cells on the left. Subsequent stripes show spontaneous errors (gaps, in this system), that can be "healed" in the next stripe. B) shows a similar observation in stripe-forming eye disc stained for Senseless. Photograph courtesy of Nick Baker.

Developing a coarse-graining for a hexagonally patterning system involves additional challenges. In the fundamental patterning unit of this system, two R8s in a regular arrangement (or some perturbation thereof) specify the location (more or less well) of a new R8 in the next column. Each template cell influences the location of two new R8s, though, and each new state (states consist of two R8s, taken together) is influenced by the outcome of two decisions made by the previous system. The obvious fundamental unit for this system, while its properties fully determine the behavior (as long as adjacent outcomes don't influence *each other*), does not generalize immediately to a large system by simply arranging many independent parallel units. The unit process, is, in fact, just another module in a larger machine with many modules interacting in a stereotyped way.

Why is this effect obvious for a unit process in the hexagonal system, but not for a similar process (where it surely must exist, also) in the stripe-forming system? The answer lies in the number of cells that are influencing the activation of the next R8s, and the effective influence of a finite size error in one of them. In a stripe, there are several cells almost directly posterior to a newly specified R8 that are influencing its specification strongly, and many cells further away that influence it very little. A perturbation at one of these positions that is more removed along the dorsal-ventral axis is unlikely to cause a finite jump in the outcome of the local stripe. For this reason, as long as the single step iteration of a stripe is done on adequately large sections of epithelium (which can be quite small), it will represent a sort of mean-field approximation of the system as a whole, and that approximation will be good.

To characterize the location of a new R8 specified by 2 R8s in the previous column, we use the following procedure. First, we define a circular zone, centered on the point where a new R8 would be optimally specified on average, and large enough to incorporate the spatial variation of a random lattice (choosing the radius equal to .6 times the mean cell-cell separation works well). Concentric to this, we draw another circle, divided into four quadrants centered posterior, anterior, dorsal, and ventral to the "optimum" circle. These areas represent the regions where a cell can be erroneously specified and still be considered a small error. We divide the circle into the four quadrants because those symmetries are broken, and these states are likely to have very different properties: The MF breaks the AP symmetry, and different errors in the two template R8s would break the DV symmetry. We could divide this circle more finely, certainly, but it makes more sense to add another kind of error possibility to the coarse-graining: Twins. Twins are, recall from Chapter III, at the very center of our understanding of the fate-selection sub-system. They are also a key feature of mutant phenotypes. In addition to the four obvious small errors that are defined by displacements in the location of the specified cell, we treat analogous errors representing one of these displaced cells specified ectopically in addition to the correct cell. Defining large error states is simple: A "zone of influence" of the two template cells is defined as a third, even larger concentric circle. Roughly, if a cell is expressed in this area and not within one of the smaller circles, it is the fault of these particular template cells, and it counts as a catastrophic error. Poorly located twins, and multiple R8s of higher multiplicity also count as large errors. There are, accordingly, 10 distinct outcomes for a

single input state: A perfect R8, 4 displaced R8s, 4 orientations of twins, and the disordered state.

The outcomes of adjacent specifications must be combined to make new states. There is the obvious state representing a perfect template. There are the obvious states typified by having one cell in the correct location, and the other displaced or twinned in one of the ways characterized earlier. There is also, obviously, the diordered state, which will catch all the states we don't define specifically. We must decide how to treat the case where both of the template cells have a small error. It is generally the case that two small errors adjacent to one another make a larger error, and we will call these error states unrecoverable. The exception is when two R8s are displaced in the same direction. In this case, they produce a perfect template that is shifted from the previous template, or a shifted twin error. If the two erroneous R8s are specified in a column that is otherwise perfectly patterned, the two error states that would have been produced by just one of these R8s are still there, just further apart in the DV direction. The pattern information (including discrete phase shifts, not exact locations of cells) is still included in the states.

In a machine of the size outlined here, it is reasonable to directly measure the probability of every transition by doing many simulations on small grids.

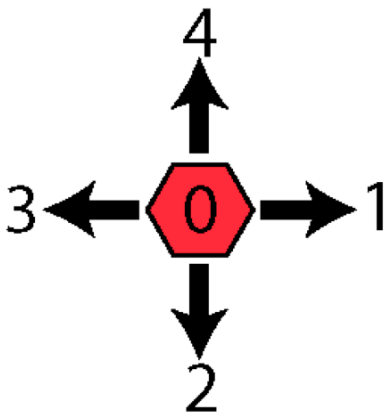

Figure 45: Small error states for hexagonal patterning. The simplest group that can be called a state in the hexagonal patterning system is two cells in a column. If they are arranged parallel to the column, and at an appropriate separation for the pattern, this is the ideal state we call ‘0’. The most obvious ways for this state to be modified, but it’s nature not completely lost, involve moving one of the cells in relation to the other, leading to states ‘1’, ‘2’, ‘3’, and ‘4’. These states are oriented, and this can be significant if they are embedded in a larger system, giving them the modifiers ‘+’, and ‘-‘. The states ‘5’, ‘6’, ‘7’, and ‘8’ can be defined by the presence of a twin consisting of the correct cell and a displaced cell. State ‘9’, the disordered state, comprises everything else.

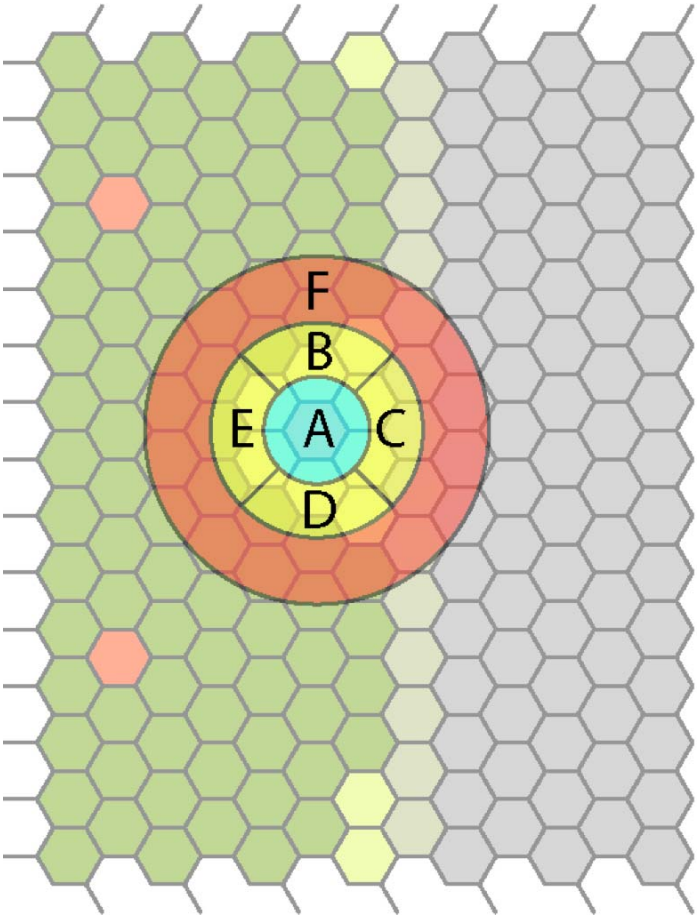

Figure 46: The result of a state. A unit state, defined by two template R8s, or their poorly specified analogues, does not lead simply to another state. It specifies a single cell. This cell can be in the correct location, 'A', or a somewhat incorrect location, 'B', 'C', 'D', or 'E', analogous to the relative shifts of the error states. It can also be a twin (A+C, for instance), or completely incorrect (F, B+C, or a triple or higher multiplicity R8).

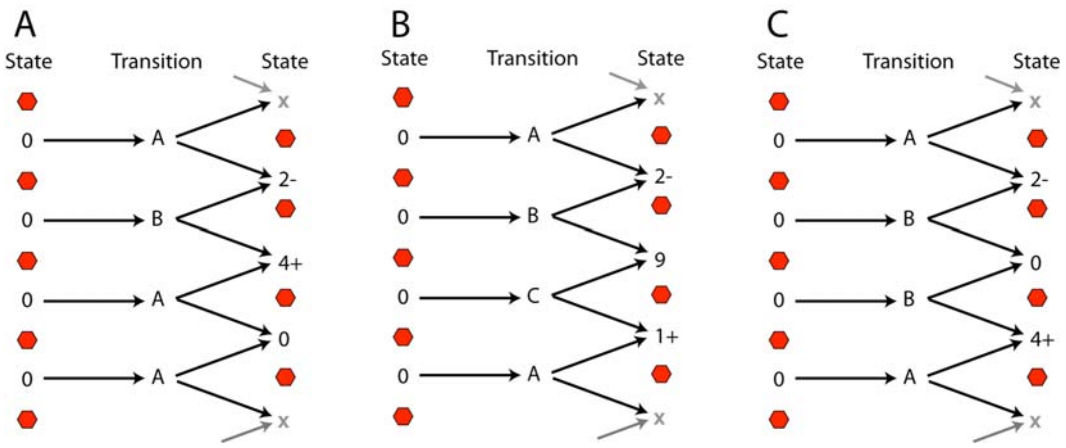

Figure 47: The state-state transition process. The outcome of two adjacent unit processes is necessary to produce the next state. An error in one process results in two related error states in the next state array. A) shows a simple upward shift of one cell produces a state with an increased template interval in the orientation (relative to the overall lattice) of Figure 45 (4+), and an adjacent one with a reduced interval in the opposite orientation (2-). B) shows two small errors resulting in a state that is classified as a large error. This is typical, in this system. The state labeled '9' will propagate its influence at each iteration until it dominates the field. This is deterministic, so our main focus is on how rapidly state '9' is generated *de novo*. C) not all small errors add to make a large error. Two adjacent small errors that are related in their displacements can produce a shifted but internally unperturbed lattice. The related errors (4+ and 2-, in this case) are still present flanking this area.

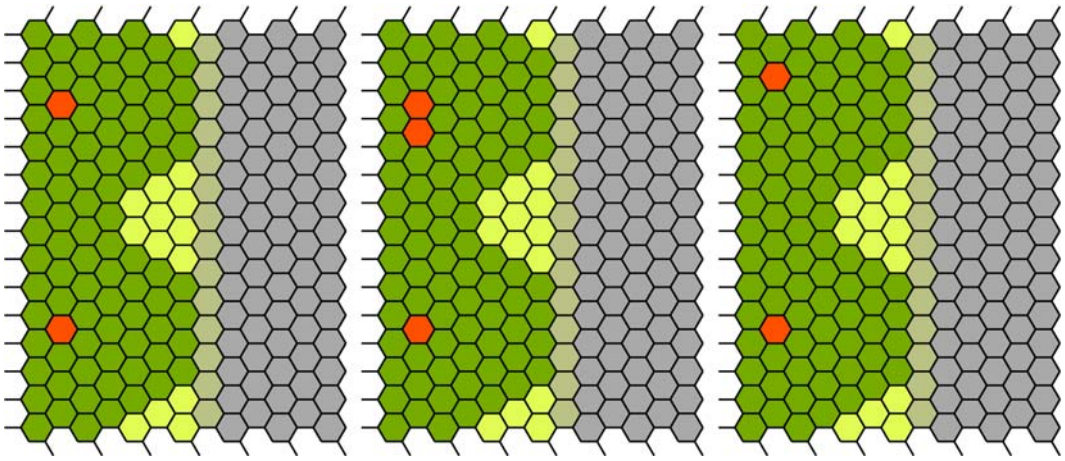

Figure 48: Examples of templates used to explore transition space. A good template, a twin, and a displacement shown on a small grid. The fully inhibited (green) and proneural cluster (yellow) cells are shown, here, with reference to the overall pattern, and it is clear that the error states will lead to a higher probability of certain errors than would a perfect template. Self healing is also likely in some cases. The actual lattices used are randomized, and the outcomes considered probabilistic.

Examples

We have explored several parameter sets representing different behavior as iterative processes approximated by finite state machines. Starting with a parameter set that was qualitatively biased toward hexagonal patterning behavior, and a parameter set that differed only at U_a and τ_u that produced stripes, we produced interpolating parameter sets and determined the outcomes of simulations on 1000 distinct 192-cell epithelia for every small error state for each parameter set using both hexagonal and stripe templates. To interpret the branching nature of the hexagonal pattern we used the following simplifying assumption: That the surrounding pattern seen by any particular cell is a perfect pattern. The results can be interpreted as an approximation to the system behavior in the limit of rare errors.

A couple of interesting observations can be made on these results, both informing our understanding of these particular parameter sets and proofing the method before we apply it to bigger, more interesting questions. The first observation is the relative sensitivity of hexagonal patterning to parameter variation compared to stripe patterning. In varying the parameters from one situation to the other, we are, of course, using the particular parameterization chosen fairly arbitrarily in constructing the model so many steps ago. It is thus not really fair to say something like “good hexagonal patterning is not robust because it disappeared very quickly when we varied some parameters,” which assumes that the parameters we chose, and the variation of them reflects some natural scale of the system. We can say, however, that while good hexagonal patterning disappeared abruptly upon varying the parameters, stripe patterning disappeared comparatively gradually and continuously. This is shown in Figure 49.

Also in Figure 49, the self-healing of the stripe pattern can be observed. The rate at which the system leaves the perfect stripe-forming state is significantly compensated by systems re-entering this state from states with some finite error. This shows up in the relationship of the rate out of the patterning state (as measured directly) compared to the net rate out of this state after giving the system a chance to evolve for one or more iterations (this rate will approach the largest eigenvalue of the linear process). Here, the difference is between 85% of systems leaving the perfect stripe state gross, and 50% leaving it, net, for the "best" stripe parameters. It is likely that if we attempted to optimize the stability of this system, we could find much more stable parameter sets. Example data and parameter sets can be found in Appendix G.

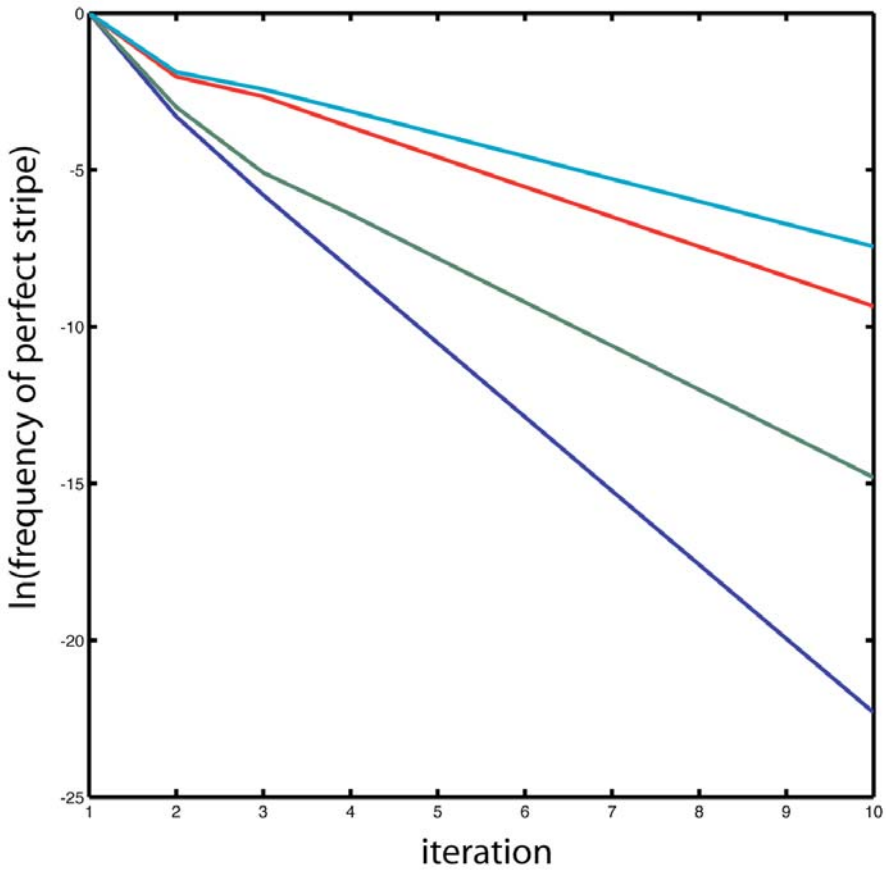

Figure 49: Rates of leaving the perfect stripe condition for simultaneously decreasing τ_u and increasing U_a. Each line in this graph represents the average frequency (*y*-axis) of a perfect stripe pattern being observed in subsequent columns (iteration, *x*-axis) of a simulation, based on simulations of one patterning step performed on 80-cell simulated epithelia. The blue line (for which stripes are destroyed most quickly) represents a parameter set that has been tuned, to some degree, to produce a hexagonal pattern. The cyan line represents a similar parameter set where τ_u and U_a have been increased to the point where some stripe-forming behavior can be observed by eye. The lines in between represent parameter sets chosen to interpolate between the hexagonal-patterning and stripe-forming ones. We see that the instability of stripes decreases as we tune these parameters. In contrast, if we examine hexagonal patterning the same way, it is lost abruptly and completely for a smaller shift in parameters. Self-healing can also be observed in this figure as a discrepancy in the slope of each line from column 1 to column 2 and the asymptotic slope. It is clear that imperfectly patterned states can lead back to perfect stripes, and this behavior is captured in our coarse-grained model. Neither of these findings speaks definitively about the biology, of course, since these represent just a few presumably unimportant parameter sets, but they illustrate the use and some of the features of our coarse-graining methodology.

The role of specific intermediate error states in producing self-healing is evident in the hexagonally patterning system, and the (still not fine-tuned) parameter set that most favors it, as illustrated in Figure 50. Evaluating the transitions from a perfect template, we see a very clear bias toward having the next cell come up shifted toward the template cells, suggesting the pattern we defined as optimum is systematically sub-optimal in this direction. The next most common errors are small shifts parallel to the MF. These errors all have relatively high-probability paths back to the perfectly-patterned state, though they are also fairly common intermediates on the path to ultimate disorder. Again, concerted optimization of parameter sets could probably reveal parameters with far more stable patterning. With a tool this powerful, though, we can begin to answer less formal questions about patterning (and its failure) as observed in nature.

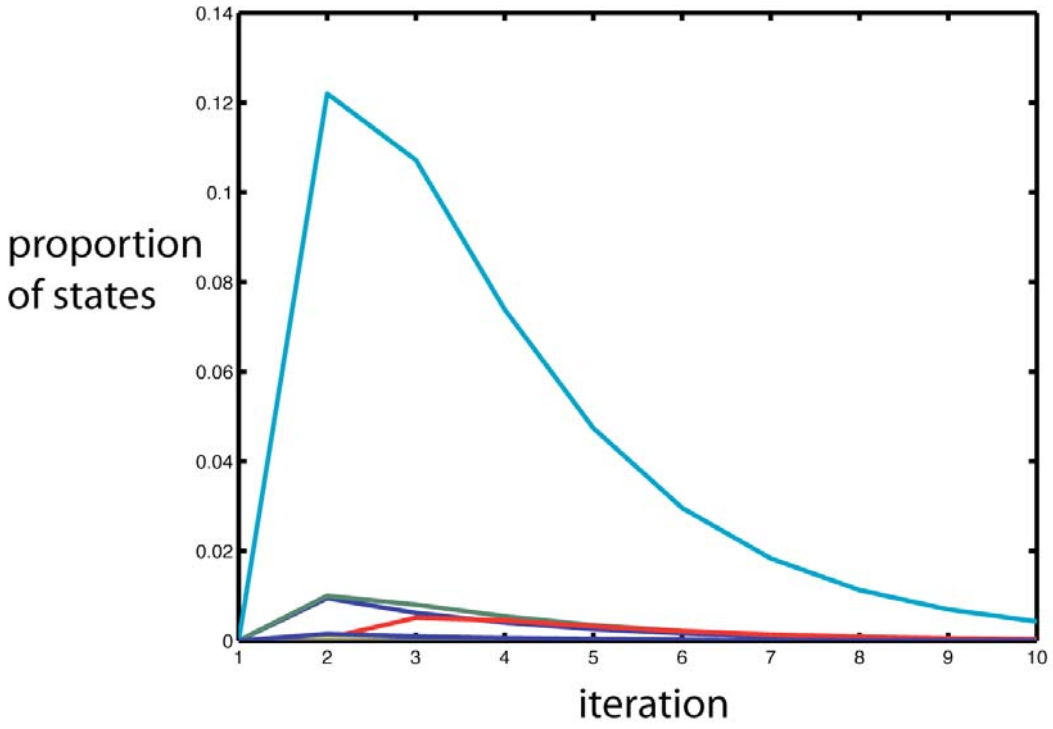

Figure 50: Intermediate error states generated by a sample pattering process. We can also look specifically at the intermediate states experienced as an ordered system collapses to diorder. In this figure each line represents the population of a different small error state of a hexagonally patterning system, as observed over many iterations, with an initial population of 1 in the perfect-patterning state. The parameter set is the one from Figure 46 that showed the worst stripes (and best hexagonal) pattern. Clearly, one of the small error states dominates, here: The one shown by the cyan line. This small error state happens to be the one representing an R8 shifted to the posterior of its optimum (average) location. The next-most frequent error states (the blue and green lines) are shifts parallel to the MF. The likely one-step errors can be seen to produce a distinct jump in a fourth type of error, in the third iteration, representing R8s shifted in the anterior direction. Small errors involving twins are very unlikely for these parameters.

Specific Applications

WT versus inhibitor-mutant patterning

As mentioned previously, and as shown in Figure 36, the R8 cells in a *sca-* mutant eye disc, or one with *Egfr-*, are not arranged in a hexagonal pattern (50). This is despite the fact that in any very small section of retina, there is likely to be an R8 specified roughly anterior to and between two other R8s. It seems that the basic patterning mechanism is not greatly changed, but the pattern, itself, clearly has. This can be explained, in general terms, as a decrease in the stability of a system previously optimized for stable patterning when subjected to a random change. This change in overall patterning quality can be observed in analyses of the sort described, here. More importantly, we can tell much more about the action of a "mutation" in the model by examining the finite state approximation of the patterning system than can be inferred from a snapshot of the level of one chemical at one time point. Observing end-state disorder in an eye disc is, after all, basically analogous to a binary classification of the rate of absorption ("fast" or "slow") of systems to the unpatterned state. Examining the patterning machine approximation we can, for instance, tell if the overall destabilization of patterning is due to an increase in the essential error rate, reduced ability to self-heal a damaged pattern, or a shift toward more-damaging types of errors. This, in turn, can help us separate system-level roles of the different genes that have patterning phenotypes. For instance, can the increased twinning observed in a *sca-* eye disc alone account for the loss of a long-range pattern?

To approach this question, we start with a parameter set that behaves in a *scabrous*-like way: Producing a bad pattern given a hexagonal template, and producing

stripes given a stripe template. We perform many simulations with a hexagonal template on small grids to get values for the transition probabilities between all the tabulated states in the patterning machine. Some of these states are twins, and some paths to disorder proceed through a twinned state. We now imagine another, un-modeled, process that is capable of resolving a twin by randomly deactivating a cell. In this case, whatever the transition probabilities from a twinned state were, they are replaced with a 50% chance of going to each of whichever states would be represented by having one of the cells inactivated. The effect of this change in the model on the stability of patterning, can be estimated without having to generate and characterize a whole new ODE model, as we did in Chapter III.

Intrinsic Errors: Edge effects and expanding domains

An eye imaginal disc is a finite object; it fits inside a larva, and the retinal field is roughly round. The MF as it proceeds across the field is not straight, but convex toward the anterior, and specifies the R8s of the next column in the center-most rows of the field before specifying the R8s of the previous column near the edge of the field (2,31). These observations may have important implications for modeling. First, the finite size of the field means that there must be edge effects. Second, not only are the cells in a column not specified simultaneously, the order of specification of R8s in a single column is not random, and DV symmetry is broken in a well-defined way. We are now equipped to examine the importance of these observations.

One more observation: Even in a wild-type eye disc, there are many R8s specified at the edge of the retinal field that are not part of the overall pattern: For our purposes, they are errors. Despite this, the pattern directly anterior to them is generally

intact: The disruptive influence of these errors does not expand symmetrically as one would expect. These observations suggest the following study.

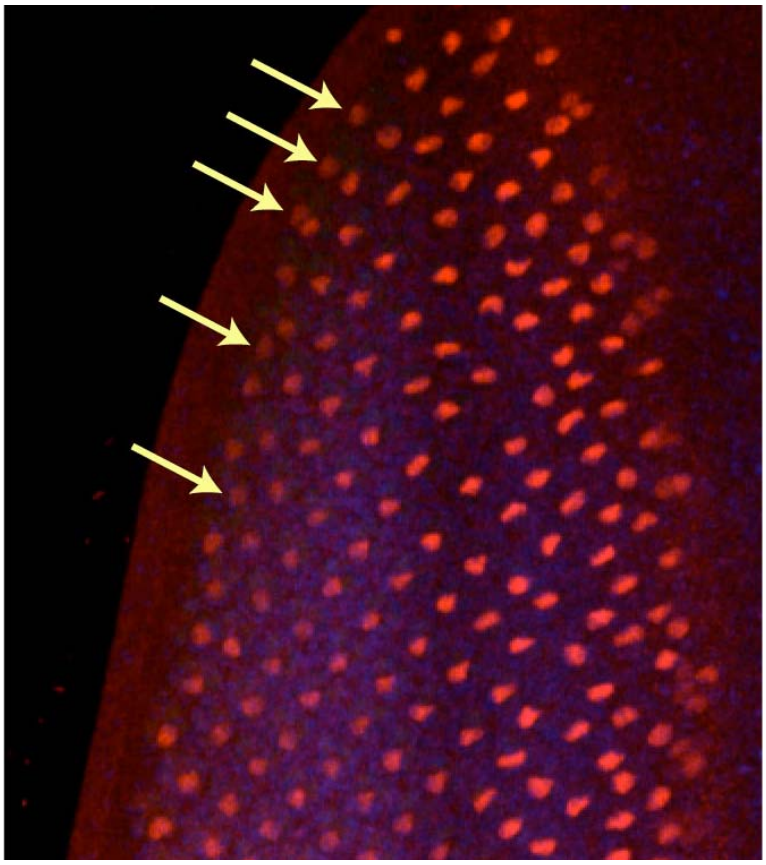

Figure 51: Eye disc stained for Senseless with attention drawn to pattern errors near the edge. In general, up until this point, we have considered uniform MFs proceeding on lattices with periodic boundary conditions, approximating an infinite epithelium. In reality, the eye-disc is finite, and the overall length of R8 columns first extends, and then contracts as the MF proceeds from posterior to anterior. The edge of the patterning field affects the patterning system. Examining the edge of this eye disc we see many cells near the edge (labeled with arrows) that do not seem to belong to the overall pattern. Interestingly, they do not seem to affect the pattering of R8s in columns directly anterior to them. This figure also shows the non-uniformity of the MF, itself. If the column being specified near the DV midline is numbered 0, and columns to the left have positive number indexes, the column being specified near the edge appears to be 2 or 3. Each column, then, is specified starting in the center, and working its way out. This broken symmetry can have an effect on how errors are produced and propagate. It is possible to examine these effects by our iterative method. Photograph courtesy of Nick Baker.

Let's treat the edge as a source of errors, and the head-start of the MF away from the edges as a symmetry-breaking perturbation that could potentially influence the propagation of an error to the next column. This requires at least two different rounds of calculating finite state machines. The first round of calculations is needed to determine the kind of errors a boundary might produce, and is accomplished by introducing artificially suppressed cells to the small-grid simulations used to estimate the transition probabilities. The second round of simulations is needed to determine the influence of the asymmetric MF on the errors produced, and, especially, the asymmetry of the errors produced by a mispatterned R8 in its two daughter states. This effectively doubles the minimum number of unique error states, as for a fixed front geometry the state with a poorly specified cell located dorsally is no longer related by symmetry to the similar state with the poorly specified cell located ventrally. The task becomes figuring out what the eventual fate of the errors anticipated by step 1 is when operated on by step 2, as illustrated in Figure 52. The results, here, could easily be counterintuitive, and this work is ongoing, so generalization would be premature. That the positioning signal from the more medial cell is read "first" by the MF seems plausible, though, and this would lead to a net flow of errors toward the margins of the eye disc. Whatever specific predictions are generated, they can be tested directly by the introduction of clones that locally destroy the pattern, or alter the structure of the MF. This is, really, a very rich direction for exploration. We are just beginning to appreciate the possibilities presented by examining the patterning system by this method. With this diversity of possibilities, close collaboration with our experimentalist colleagues is imperative.

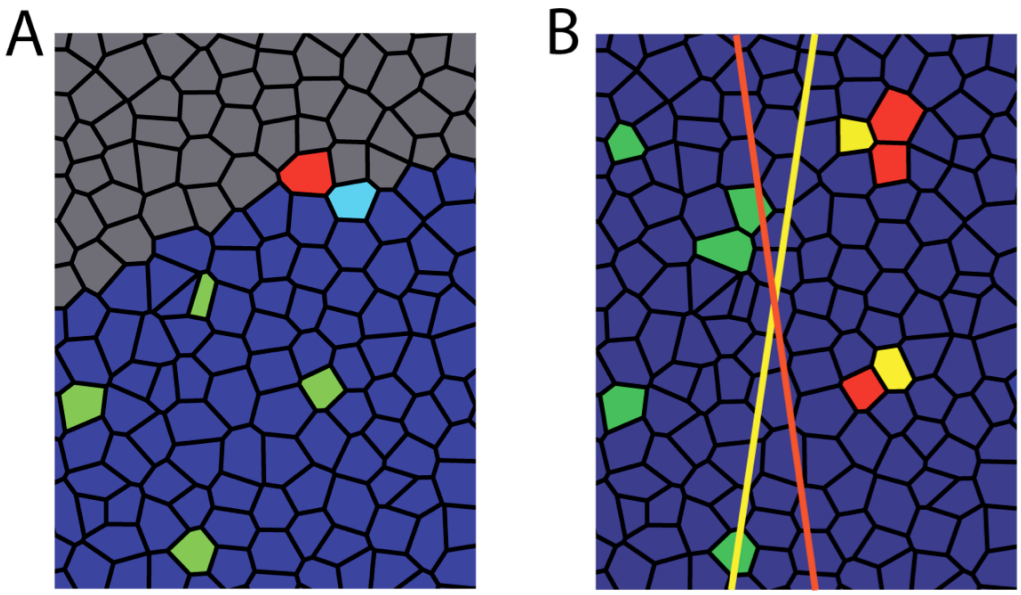

Figure 52: Studying edge effects and MF asymmetry. A) The edge of the retinal field introduces errors into the pattern. In this figure, the pattern-appropriate cell to become an R8 is colored red, but it lies outside the retinal field. The light blue cell becomes specified, instead, making a characteristic error for this edge geometry. We can use small simulations to determine what the characteristics of these errors are and compare this with observations. This can also be used to dictate what the initial conditions should be for a study of error propagation near edges or clones. B) Of particular interest is the possible physiological reason the MF is not parallel to columns. In this figure we show a hypothetical differential outcome for a MF angled one way (yellow) and the opposite way (red) as it encounters a spontaneous template error (twin). With the dorsal-ventral symmetry broken, the influence of errors no longer needs to propagate symmetrically away from an initial event. This could shed light on the reason edge-created errors seem to have no impact on the pattern in the main part of the disc, even directly anterior to the initial error.

Chapter V:

Conclusion

Starting with an ODE model that recapitulates WT R8 patterning in the *Drosophila* eye disc, as well as unexpected mutant phenotypes, we have developed a multiscale theory of the new form of pattern formation that it represents. The first step was to confirm the existence of self-propagating patterning solutions, given appropriate choice of parameters and initial conditions in a simplified 1D system. This study, summarized in Chapter II, yielded the following results. First, the formation of regular patterns is possible in this system, and those solutions are stable. Second, this behavior exists in a limit of the system characterized by a large separation of timescales between the functional modules governing MF propagation and local fate maintenance, and is thus very robust to parameter variations. Third, more than one stable solution to the equations could exist, with drastically different behavior, depending on initial conditions. The patterning system is not characterized by linear instability of a homogeneous steady state to inhomogeneous perturbations, or the interpretation of a morphogen gradient by factors with many different sensitivities. Single cells with arbitrarily large separation are selected with only one simple, diffusible inhibitor. All of these results were found in a model limit (fast inhibition) that precludes the existence of an oscillator, and thus a clock-

and-wavefront patterning system, though there is some interesting overlap between the function of these systems.

To understand the model more generally, we attempted to generalize the patterning mechanism characterized in 1D to 2D, and a more complicated ODE model that reproduces the proneural cluster phenomenon seen in eye discs. This involved, sequentially, characterizing the behavior of ever-larger groups of cells. First, we characterized the behavior of isolated cells in detail, and found we were able to reduce their important behavior to the delays they exhibit between receiving an activating signal and 1) achieving R8 fate-permanence, and 2) inhibiting their neighbors effectively. These thresholds proved to summarize the behavior of pairs of cells, synthetic 7-cell proneural clusters, and the proneural clusters that arise spontaneously in an epithelium templated with previously specified R8s over a range of parameters. The distributions of outcomes of cell-fate decisions we expect for different initial conditions explains the observation of stripes, and frequent twins in inhibition-mutant eye discs. Additionally, our understanding predicts that R8 cells can be specified arbitrarily close to a neurogenic clone, such as *E(spl)*-. These studies are described in Chapter III.

Lastly, we have developed a method for looking at long-range pattern formation that takes as an input a mechanism of fate selection, such as we characterized in Chapter III, and uses a finite-state machine approximation to predict its behavior over many iterations. While still exploratory, this method is directly inspired by the physics of the system, as we understand it, and very general in its predictive capabilities. It can account for the ability of patterns to self-heal with respect to small but significant errors, the fragility of hexagonal patterning to significant mutations, and the relative robustness of

stripe-formation to those perturbations. We plan to use it to address larger-scale questions pertaining to the orientation of the MF, and retina-field edge effects, which were previously very difficult to address.

The success of this model, and our theory describing its function, lies in its predictive power, which is general, and also in the understanding it gives us of this type of system.

Appendices

Appendix A: 1D Parameter Scan Details

In this appendix I will discuss in greater detail the numerical processes involved in simulating and classifying the behavior of the large parameter scan of the 1D system presented in Chapter II.

Each of the 640,000 parameter sets for the 1D system described in Chapter II was subjected to several numerical and analytical tests. First, as an undirected exploration of the system's behavior, each was used to define a model of form equation (1) on an array of 1024 cells with periodic boundary conditions. Initial conditions were set to be zero for all fields over all cells except for a on 100 adjacent cells, which was set to random uniform variants between 0 and 0.25. The equations were then integrated forward in time using an explicit Euler integrator, but treating the linear interaction terms fully implicitly. Each model was integrated forward in time 5000 time steps with dt=.06. All of the basic behaviors discussed in the paper (non-patterning front, stalled systems, patterning fronts, fronts producing complicated patterns and transient activation) were observed in this test. Patterns were analyzed by eye to get a sense for the scope of the problem, and algorithmically to systematically classify the results. Another, similar test was conducted on a subset of stalled fronts using random uniform variants up to .35, which yielded the results that some of the stalled solutions became propagating solutions and demonstrating this simple predicted initial condition dependence.

The first step in automatically classifying patterns was to apply a threshold to *a* corresponding to halfway between the zero-activation high steady state and the zero-activation intermediate steady state (the "point of no return," analogous to the separatrix in Chapter III). For parameter sets where these steady states do not exist (A_a>.569) an arbitrary but functional threshold of 0.5 was used. The easiest behavior to classify, in general, is transient activation, as it requires only to see a point that was once above threshold go below threshold. It is easy to classify the non-patterning fronts next. Due to the fact that the range of the inhibitor is, in general, pretty short, we decided to classify as non-patterning any front that showed at least 20 consecutive cells above threshold behind the first active cell at the end of integration. If the front overran the entire field in a shorter amount of time, the front was additionally classified as "fast," and the last saved time point where the periodic boundary conditions were considered trivial was used to evaluate the pattern. The vast majority of "fast" fronts were unpatterned, but there were exceptions, and it became clear that for more careful comparison, a one-size-fits-all integration time-step would not work. To be considered regularly patterning, the last five groups of adjacent active cells had to consist of single active cells, and 3 of the 4 intervening gaps had to be equal in size. The solutions producing complicated patterns were subdivided into those with multiple adjacent cells in one of the most recent 5 groups, and those without. The first group dominated this category. To be considered stalled, a front had to produce no new active cells between time steps 2500 and 5000. Slipping through the cracks in this analysis are parameter sets that form very slowly propagating solutions. Indeed, parameter sets not conforming to any of the descriptions above were provisionally labeled "unknown behavior," but upon detailed examination

most proved to produce solutions that activated <5 cells, but did activate at least 1 in the interval 2500*dt*-5000*dt*, thus failing the test for stalled-ness.

To calculate propagating solutions based on the structure of our theory, we needed to calculate the amount of inhibitor at the points ahead of a patterned halfspace (which is simply a geometric series), and the time when h_{crit} is exceeded for each of these points. Once that is calculated, the priority of the point representing continued patterning must be established by calculating h and h_{crit} at its neighbors. h_{crit} is easily calculated by setting $\partial_t a$ to zero, finding $g(h)$ as the root of the resulting polynomial, and then inverting that function if it is less than 1. $h_x(t)$ was constructed numerically, and a standard root-finding algorithm was used to solve the relationship $h_x(t) - h_{crit} = 0$ for t at all integer x up to either the maximum value of x where $h_x(\infty) - h_{crit} > 0$. The numerical approximation for $h_x(t)$ involved summing contributions from more and more distant active patterned sites according to equation #, using a Runge-Kutta integrator with adaptive step size (because of the presence of more than one time-scale in the integrand) for the time integral, until one of two truncation conditions was met. The first truncation criterion was rarely used and involved a simple truncation if the contribution from the last patterned site was less than 10^{-11} of the running total. The second truncation method involved evaluating the ratios of contributions of consecutive sites, and, in the event the relative change in these became less than .01, extrapolating the further contributions as the total of an infinite geometric series with the appropriate decay constant, which gives excellent results.

With this new information, a second pass over the parameter sets was made, setting initial conditions and integration parameters according to the predicted patterning

behavior. The initial conditions for all cells and all fields were zero, except for one cell at the end of the (no longer periodic) array which had *a* at the high steady state. *h* was put into the system as a time-dependent boundary condition based on the solution to the unpatterned continuum problem with the appropriate constants, and corrected to account for the h produced by the initial 1-cell prepattern. The time-step, *dt*, was set to be .02 times the amount of time the front was expected to take to propagate 1 lattice unit, or .06, whichever was smaller, and the equations were integrated for twice as long as we anticipated it would take to produce 5 active cells. This led to some very long integrations. The time of each cell's activation was recorded and used to calculate the front speed. Pattern classification was conducted by methods similar to those described above. The main differences in the classification between these parameter sets were that some parameter sets that yielded non-patterning fronts originally yielded patterning ones, and those that were too slow to classify in the previous test were shown to propagate and pattern as expected.

Appendix B: 1D Limit Cycle Amplitude

In this appendix I will discuss the change in shape of a propagating wavefront of the activator *h* due to periodic spatial structure in its source.

We are interested in the behavior of the following equation as $t \to \infty$.

$$\tau_h \partial_t h = \cos\left(2\pi x / n\right)\Theta\left(-x + vt\right) - h + D_h \partial_{x,x} h \qquad \textbf{(1)}$$

Making the substitution $x\text{-}vt \to z$ and taking the Fourier transform with respect to z and conjugate variable q we get an easily solved ODE:

$$\tau_h \partial_t \tilde{h} + iqv\tau_h \tilde{h} = F\left(\cos\left(\frac{2\pi\left[z+vt\right]}{n}\right)\Theta\left(-z\right)\right) - \tilde{h} - q^2 D_h \tilde{h} \qquad \textbf{(2)}$$

Taking the Fourier transform of the source term, applying arbitrary initial conditions, setting to zero terms which decay in time, and inverting the transform for the resulting solution for $\tilde{h}\left(q,t\right)$ to get *h(z,t)*, we arrive at the general solution, which must be defined piecewise:

$$h\left(z,t\right) = f_0 \begin{cases} \dfrac{e^{-z\left(\frac{\tau_h v + \sqrt{\lambda}}{2D_h}\right) - i2\pi v/n}}{\sqrt{\lambda}}\left(\dfrac{D_h}{\left(b^* + \sqrt{\lambda}\right)} - \dfrac{D_h}{2\left(b + \sqrt{\lambda}\right)} - \dfrac{D_h}{2\left(-b + \sqrt{\lambda}\right)}\right) - \dfrac{e^{-z\left(\frac{\tau_h v + \sqrt{\lambda^*}}{2D_h}\right) + i2\pi v/n}}{\sqrt{\lambda^*}}\left(\dfrac{D_h}{\left(b + \sqrt{\lambda^*}\right)}\right), z > 0 \\ \dfrac{\cos\left(2\pi\left[tv + z\right]/n\right)}{1 + 4\pi^2 D_h / n^2} + \dfrac{e^{z\left(\frac{-\tau_h v + \sqrt{\lambda}}{2D_h}\right) - i2\pi v/n}}{\sqrt{\lambda}}\left(\dfrac{D_h}{2\left(b + \sqrt{\lambda}\right)} + \dfrac{D_h}{2\left(-b + \sqrt{\lambda}\right)} - \dfrac{D_h}{\left(-b^* + \sqrt{\lambda}\right)}\right) - \dfrac{e^{z\left(\frac{-\tau_h v + \sqrt{\lambda^*}}{2D_h}\right) + i2\pi v/n}}{\sqrt{\lambda^*}}\left(\dfrac{D_h}{\left(b + \sqrt{\lambda^*}\right)}\right), z \le 0 \end{cases} \qquad \textbf{(3}$$

$$\lambda = \tau_h^2 v^2 + 4D_h - i8\pi D_h \tau_h v / n$$

$$b = \tau_h v + i\,4\pi D_h / n$$

Using the fact that $\mathrm{Re}\left[\sqrt{1+iy}\right] \ge 1$ for all real y, it is clear that the terms where e is raised to a power of y all decay faster in space for finite n than do the spatially dependent terms for a homogeneous source density. The terms describing the overall

scale of the solution (which is best thought of as a correction to the homogeneous-source solution) are complicated in detail, but the general parameter dependencies are notable. Most notably, we are interested in the limit where $D_h \gg \tau_h v$. We see, in this case, that for very large n, i.e. long wavelength, the amplitude of the correction terms approaches the amplitude of the average solution. On the other hand, for very short wavelengths, the proportionate amplitude of the corrections goes to zero at least as quickly as $n^{3/2}$. We can estimate the scale that determines the dominant behavior by setting the magnitudes of the two final terms in λ equal and solving for n.

$$\begin{aligned} & 4D_h = \frac{8\pi D_h \tau_h v}{n} \\ & \Rightarrow \\ & n = 2\pi\tau_h v \end{aligned} \qquad \textbf{(4)}$$

This tells us that diffusion really starts evening out the variability from the source when the characteristic scale is smaller than the amount of source traversed by the moving front in an amount of time characterized by the internal dynamics. If the source pattern is a sum of harmonic terms with a largest spatial scale given by the pattern period, it is possible to calculate a bound on the maximum amplitude of the limit cycle. It involves the Riemann Zeta Function and tends to be not-very-big:

$$\frac{n_{\max}^{3/2}\zeta\left(\frac{3}{2}\right)}{\sqrt{\pi^3 D_h \tau_h v}} \approx 0.0415 \frac{n_{\max}^{3/2}}{\sqrt{D_h \tau_h v}} \qquad \textbf{(5)}$$

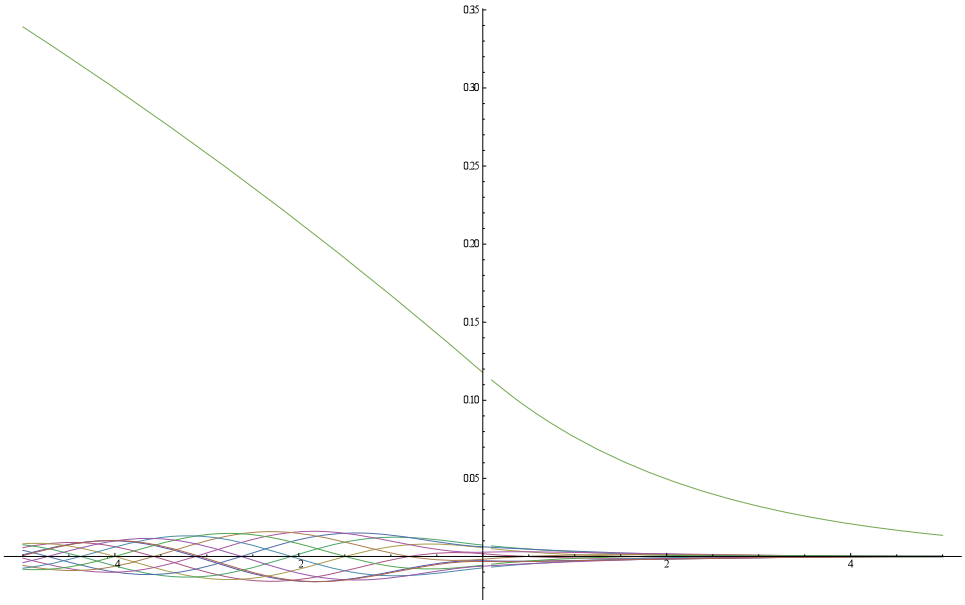

Figure 53: Average propagating *h* for reference parameters in the continuum with deviations produced by a periodic template. The deviations are quite small compared to the overall *h*.

Appendix C: Generality of the *h*-*u* Interaction

In this appendix I will discuss the interaction of the moving *h* gradient and the stationary *u* gradient. The goal is to illustrate that the two limits characterized in Chapter II (piecewise linear *h*, and step-function *h*) are sufficient to characterize the dynamical interaction in this system.

We consider the interaction of a uniformly translating front of h interacting with an inhibitor template exponentially decaying in space, u.

$$\begin{aligned} h_x(t) &= h(z) \\ z &= x - vt \\ u_x &= u_0 e^{-k_0 x} \end{aligned} \qquad \textbf{(1)}$$

There is a critical value of h, h_{crit}, which is dependent on u.

$$\begin{aligned} h_{crit}(u) &= H\left[\frac{1 - h_c - h_c\left(u/U\right)^{m_u}}{h_c\left(1+\left(u/U\right)^{m_u}\right)}\right]^{-1/m_h} \\ h_c &= h_{crit}(0) \end{aligned} \qquad \textbf{(2)}$$

Here, we have introduced h_c as the (easily approximated) bifurcation value of h with no inhibitor. Setting the equation equal to a particular reference value of h_{crit} (h_r) and solving for x yields:

$$h_{crit}\left(u_x\right)=h_r$$
$$\Rightarrow$$
$$x=\frac{\ln\left[u_0\right]}{k_0}-\frac{\ln\left[U\right]}{k_0}-\frac{1}{m_u k_0}\ln\left[\frac{-h_c+\left(h_r/H\right)^{m_h}-h_c\left(h_r/H\right)^{m_h}}{h_c\left(1+\left(h_r/H\right)^{m_h}\right)}\right] \quad \textbf{(3)}$$

Unsurprisingly, the self-similarity of exponential functions means that a change in the source strength of the inhibitor leads to an overall translation of the continuum version of h_{crit} dependent only on the length scale of u, $1/k_0$. Since the function is actually only defined for integer x, we would generally expect the first point to exceed h_{crit} as time goes forward to be one the integers flanking the continuum solution representing tangential contact between continuum h and continuum h_{crit}.

$$x=\left\lfloor \arg_{x'}\left[h_{crit}\left(x'\right)=h\left(x'\right),\partial_{x'}h_{crit}\left(x'\right)=\partial_{x'}h\left(x'\right)\right]\right\rfloor+\frac{1}{2}\pm\frac{1}{2} \quad \textbf{(4)}$$

Small changes in u_0 can only switch the first point between these two options, generically. "Small changes" in this case means that all possible contributions to u from the pattern preceding the most recent patterned point will not shift x by more than one half. For preceding patterns with period n and $n+1$ this means.

$$\frac{\ln\left[u_0\left(\frac{e^{nk_0}}{e^{nk_0}-1}\right)\right]}{k_0}-\frac{\ln\left[u_0\left(\frac{e^{(n+1)k_0}}{e^{(n+1)k_0}-1}\right)\right]}{k_0}<\frac{1}{2} \quad \textbf{(5)}$$

This condition is always met if $nk_0>ln[3]\approx1.009$. This suggests that for general h, the ideas involved in dealing with the map are sound as long as the characteristic decay length for the inhibitor is not longer than the period of the pattern.

The exception to this rule is when the shapes of h and h_{crit} are very similar near their point of first contact, so that small changes in u *could* lead to large changes in their intersection at discrete points. By definition, if we expand about x' in Taylor series, h and h_{crit} are identical at the constant and first order terms. The second order term is positive and potentially quite large for h_{crit}, as it is proportional to k_0^2, whereas for h, we expect it to be very small for two reasons. First, it is proportional to the inverse square of the length scale of h, which we have determined (through design and parametrization) will be much longer than that for u. Second, our knowledge of the physics of the system strongly implies that the pertinent value of h_{crit} will be very close to the inflection point in *h(z)*. The propagating solution for h has a finite discontinuity in the second derivative at *z=0*, but the average second derivative about this point is proportional to $1/D_h$, which we expect to be very small, indeed. Essentially, unless we invoke more exotic functional forms that lead to more near-contacts between h and h_{crit} *distant* to the contact which defines a certain pattern, the physics of the model will be such that a sharp, unique intersection is guaranteed, and the behavior of the map is as simple as for the step-function and piecewise-linear cases.

Appendix D: Artificial Cellular Epithelia

In this appendix I discuss the generation of structured cellular lattices for running simulations on 7-cell and 192-cell systems.

Lattices for cellular systems representing disordered 2D epithelia are necessary for our 2 dimensional studies. 1-cell and 2-cell systems are trivial in this respect, so this discussion begins with 7 cell clusters. To produce these clusters, we used an optimum arrangement of 7 cells in a rosette as a starting point, with unit distance between the centers of mass of adjacent cells. We then perturbed the location of each cell in 2 orthogonal directions by adding normally distributed random numbers with σ=.*2*. We then rotated the overall locations of the cells by a random angle $0 \le \theta \le \pi/6$ drawn from a uniform distribution. The symmetry of the system guarantees that this covers all distinct orientations versus in space compared to a fixed axis. This fixed axis we take to be the *x* axis, along which the MF propagates in the positive direction. The location of each cell projected on this axis, and divided by the time characterizes the delay, Δt.

Producing lattices with significant 2D structure is more involved. In this case, the starting point is a hexagonal lattice that is periodic in the dorsal-ventral direction, which we also choose to be the direction of one of the (non-orthogonal) basic lattice vectors. Again, the cells are perturbed shifted by uniformly distributed random numbers with σ=.*2*. In these systems, we have chosen to randomize the strengths of the interactions between adjacent cells (and which are adjacent! We don't want to preserve the perfect hexagonal structure, which is non-physical). A Voronoi tessellation based on the points as located, so far, gives an overall appearance that quite resembles a cellular epithelium,

and gives the obvious benefit of defining adjacency in a systematic way. The cells near the boundary we desire to be periodic can be treated by replicating the lattice in these directions before tessellating, and inferring the periodic links by mapping to the appropriate equivalent cells. It remains to define the strength of diffusive coupling between adjacent cells. The obvious metric, which relates the hopping rate to the inverse square of the distance between the points the tessellation was based on has a problem: The maximum strength of the coupling between adjacent cells is unbounded, which seems inappropriate. For the studies in this thesis we make the coupling strength proportional to the length the edge separating two cells in the Voronoi tessellation. We set the average strength of these interactions for a lattice to the parameter D_u. The location of each cell for purposes of interacting with the MF is defined by the center of mass of its Voronoi polygon.

Figure 54: Illustration of the steps involved in making a simulated epithelium. A) First we specify a regular hexagonal grid of the correct size, in this case 6 rows by 8 columns (red dots), which we then perturb in the *x* and *y* directions with normally distributed random numbers (blue dots). B) We repeat the lattice in the periodic (*y*) direction (small red dots), and perform a Voronoi tessellation to define "cells." C) The Voronoi tessellation defines the connectivity of the lattice (magenta lines), and the length of each interface scales the strength of specific diffusive couplings. D) The locations of the newly-characterized cells are taken to be their centers of mass (magenta dots). The bottom row of cells communicates with the top row of cells with coefficients determined by the strength of interactions with the equivalent-but-translated cells from graph 'C.'

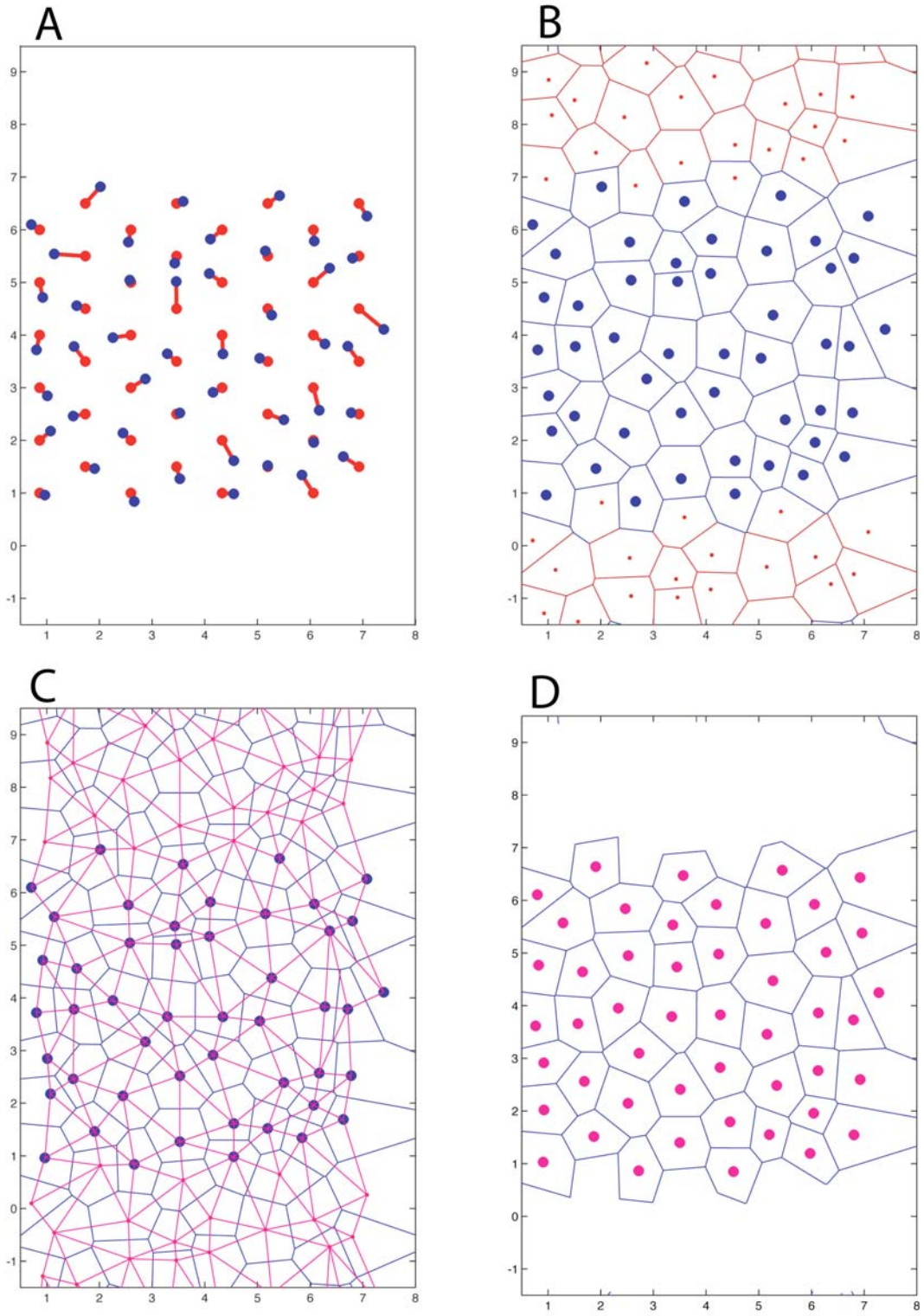
A
B
C
D

Appendix E: Empirically characterizing the one- and two-cell systems

In the course of events, we need to calculate 1) the separatrix in the *a*-*s* plane defining permanent R8 fate, 2) T_1 as a function of u_{ns_α}, 3) T_u as a function of u_{ns_α} and u_{ns_β}, and 4) the empirical transitional Δt that satisfies the equality conditions for the one-cell-selected inequalities shown below without idealizing the dependence of T_1 and T_u.

$$T_{u\alpha} < \Delta t + T_{1\beta} \quad \textbf{(1)}$$

For cell α, alone, to be selected, and

$$T_{u\beta} + \Delta t < T_{1\alpha} \quad \textbf{(2)}$$

For cell β, alone to win. Here, as elsewhere, Δt is positive when cell β is activated after cell α.

Calculating the separatrix for a particular parameter set is simple. We find the unstable fixed point of the *a*-*s* system, reverse the dynamics of that system, give it initial conditions slightly perturbed from the fixed point in opposite directions, and integrate until limiting values (*0* or *1* for *s*, 0 or *1*+*G*+*B* for *a*). We then connect the two branches of the solution across the saddle, and interpolate with a cubic spline. This function can then be used in other tests to determine whether a particular trajectory has been committed to R8 fate.

Calculating T_1 and T_u requires integrating a single-cell system for many values of u_{ns_α}. Since we are not simulating adjacent cells explicitly, we approximate the rate at

which u is lost to the surroundings by having it diffuse away at a rate proportional to inactive adjacent cells. We use both singly-activated cells and cells activated in tandem as references. In this approximation, there is no facility for u to come back to the original producing cell, and so it is lost to the environment at an artificially high rate. In any case, T_1 is found directly from these simulations by calculating the time at which the separatrix was crossed (if it was) by a trajectory. If several lifetimes of the slowest-evolving factor pass without the separatrix being crossed, we consider a cell experiencing that inhibition to be fully, insurmountably inhibited. Activation in calculations is full and immediate: the profile for h is effectively a step function.

To calculate T_u, which must be known as a function of external inhibition at both cells, we use the trajectory of a determined by the previous study, and use it to integrate an equation with an appropriate source of u using the same approximations as for T_1.

$$\begin{aligned} \partial_t u_\alpha &= f\left(a_\alpha\right) - u_\alpha + D_u\left(n-m\right)\left(u_\beta - u_\alpha\right) \\ \partial_t u_\beta &= -u_\beta + D_u m\left(u_\alpha - u_\beta\right) \end{aligned} \qquad \textbf{(3)}$$

This is a linear inhomogeneous system of differential equations that is trivial to integrate. We have introduced the constants m and n which, represent, respectively, the number of simultaneously activated cells, and the effective cluster size. With time traces, now, for u at neighboring cells for various trajectories subject to different inhibition, we can simply invert these to get T_u as a function of both $u_{ns\alpha}$ and $u_{ns\beta}$.

$$\begin{aligned} & u_\beta\left(T_u, u_{ns\alpha}\right) + u_{ns\beta} = u_{critical} \\ & \Rightarrow \\ & T_u\left(u_{ns\alpha}, u_{ns\beta}\right) = u_\beta^{-1}\left(u_{critical} - u_\beta\right) \end{aligned} \qquad \textbf{(4)}$$

Here, $u_{critical}$ is simply the highest value of external u that still allows a cell to be activated. T_1 and T_u are obviously subject to approximations; these are discussed in the main text.

The approximation addressed in doing two-cell simulations is that these trajectories, perturbed by nearby cells activated at finite delays, are not changed in such a way as to substantially change T_1 or T_u. To test this, and map the outcomes of interacting cells, we conduct simulations of two cells over a range of $u_{ns\alpha}$ and $u_{ns\beta}$. The goal, here, is to determine the Δt for each pair of inhibitor values that satisfies equality for each of equation (1) and equation (2). If there is exactly one transition (as seems likely), this can be accomplished using a simple 1D root finding algorithm at each step, if each outcome is encoded numerically. We proceed thusly, using the method of bisection at each inhibition state. The total space is related by symmetry as:

$$\Delta t_{\alpha}\left(u_{ns\alpha},u_{ns\beta}\right)=-\Delta t_{\beta}\left(u_{ns\beta},u_{ns\alpha}\right) \quad \textbf{(5)}$$

Where Δt_{α} is the time delay required for cell α alone to become activated. This as well as the fact of the typically weak dependence of Δt on either u_{ns} over most of their range (which facilitates the use of predictive algorithms) speed this empirical mapping up, considerably. In deploying the root-finding algorithm, we allow a maximum range about zero delay that is five times the observed zero-inhibition critical delay, which is more than adequate to capture the important behavior.

Appendix F: Range of behavior for a single cell

In this appendix I will discuss the behavior of cells at the transient, proneural cluster level of activation defined in the 4-variable model.

The behavior of a cell near its intermediate steady state can be non-trivial. Much depends, here, on whether the cell is experiencing inhibition, or not. If it is, then the timescale of that inhibition can determine whether the "intermediate steady state," which isn't a steady state at all, but a temporary pause for *s* to build up, is approached as a spiral, or whether it is unstable and there is a limit cycle in the *a*-*u* system. These are, of course, drastically different than the steady approach seen if *u* is effectively zero. This is due to the relaxation-oscillator-like structure of the *a*-*u* system.

If one increases τ_u with *s* fixed significantly below the level where it strongly activates *a*, the steady state (which is the intermediate, proneural level of *a* expression) undergoes a supercritical Hopf bifurcation, becomes unstable, and spawns a limit cycle with a finite period. The relevance of this quasi-periodic behavior is not clear. In general, at when cells are at this intermediate state is when they are susceptible to the influence of external inhibitor in a continuous way, and the amount of time they spend here, as well as dynamic properties of the state are the major sources of non-ideality in generalizing about multiple-cell behavior from one-cell behavior. This effect is not so large in what we consider "physiologic" parameter regimes, however, as the period of the oscillations (whether they be spiraling or cycling) is fairly large. The parameter that most directly regulates the duration of this state, τ_s, must be made quite large in order to see more than one or two oscillations. We feel that this is not realistic, since the response of a local transcription factor can be quite rapid.

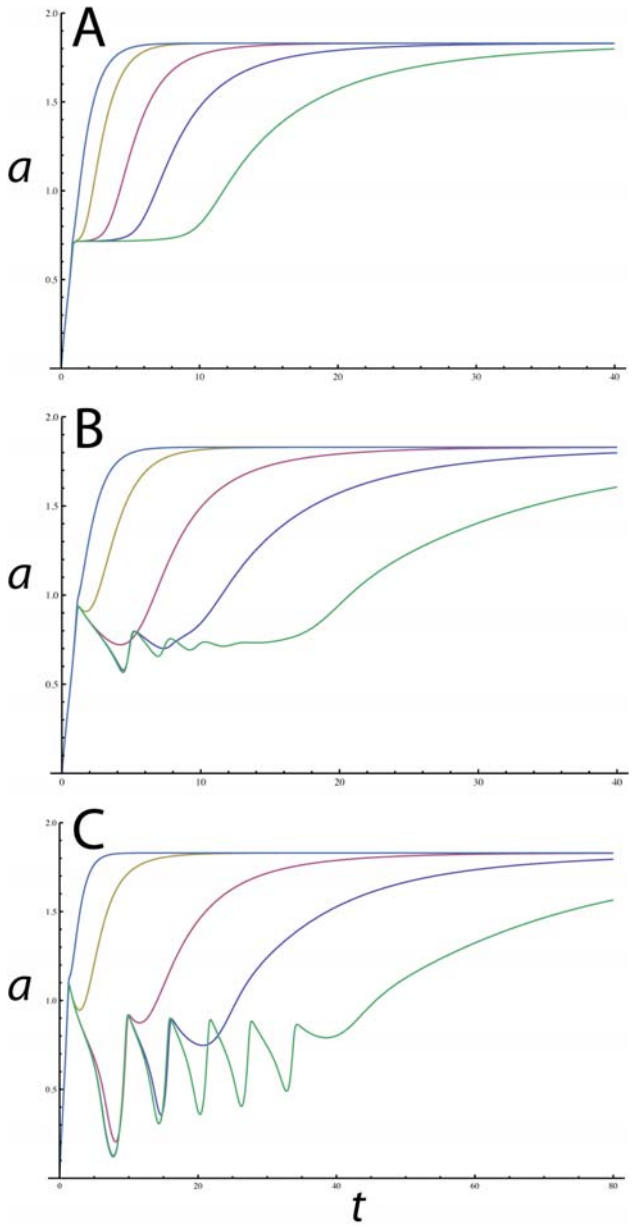

Figure 55: Different behaviors of the intermediate-*a* state. Each graph shows trajectories of a for several increasing values of τ_s, and thus longer pauses at the proneural cluster *a* level. A) shows the results for very fast *u* dynamics, where *a* is very overdamped at the intermediate level. B) shows the same parameters with larger value of τ_u. Now *a* approaches the proneural state as an underdamped oscillator. C) shows even slower *u* dynamics. Now the proneural steady state, as defined with fixed *s*, has become Hopf-unstable, and the trajectory approaches a limit cycle. To get the number of oscillations seen here, *s* dynamics must be made much slower than we feel is appropriate. One to three cycles is commonly observed, though.

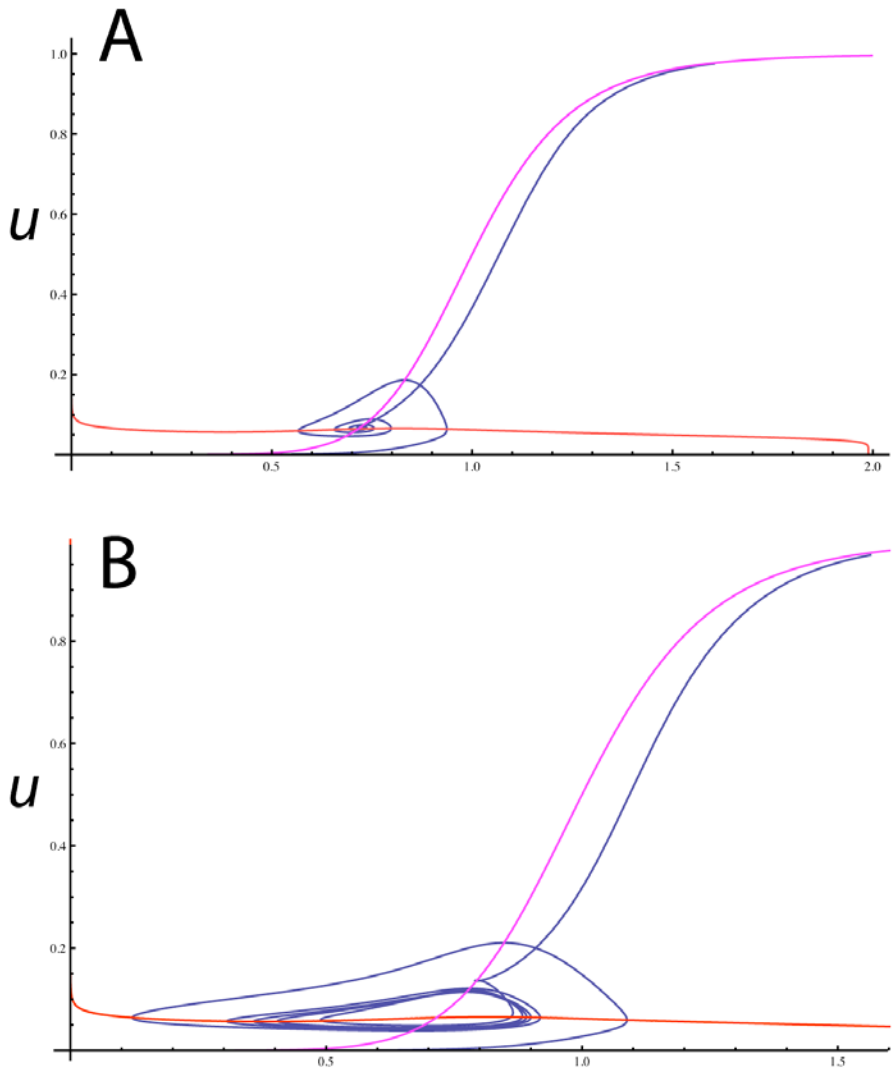

Figure 56: Trajectories of stable-spiral and limit-cycle proneural states in the a-u plane. A) shows the slowest-*s* trajectory from Figure 55(B) projected in the *a*-*u* plane. The trajectory's spiral approach to the quasi-static proneural state is clearly visible. B) shows the slowest-s trajectory from Figure 55(C) projected into the *a*-*u* plane. The approach to a limit cycle, and the subsequent destruction of this cycle is clearly shown.

Appendix G: Representative Data for Finite State Model

The results of running 1000 simulations on a single parameter set for each of 9 different template conditions representing a hexagonal patterning system, as described in Chapter IV, are shown in Table 2. The parameter set used in summarized below. All Hill exponents were 4, except for those involved in producing and sensing inhibitor, which were 12.

A_a=.65

S_a=.65

B=1

G=1

U_a=.00065

A_s=.5

A_u=1.2

D_u=.9

τ_s=.7

τ_u=1

	0→	1→	2→	3→	4→	5→	6→	7→	8→	9→
→0	0.798	0.038	0.074	0.257	0.383	0.684	0.006	0.549	0.036	0
→1	0.052	0.07	0.012	0.153	0.002	0.012	0	0.019	0.001	0
→2	0.059	0.002	0.138	0.009	0.119	0.12	0.074	0.121	0.142	0
→3	0.028	0.825	0	0.478	0.007	0.003	0	0.001	0	0
→4	0.021	0	0.482	0	0.308	0.109	0.634	0.218	0.461	0
→5	0.014	0.005	0	0.036	0.001	0.001	0	0.002	0	0
→6	0.009	0.001	0.004	0.003	0.007	0.019	0	0.013	0.001	0
→7	0	0	0	0.001	0	0	0	0	0	0
→8	0.002	0	0.001	0	0	0.005	0	0.003	0.001	0
→9	0.017	0.059	0.289	0.063	0.173	0.047	0.286	0.074	0.358	1

Table 2: Example transition matrix for finite state approximation. Each column of the transition matrix contains summarizes the transition probabilities of a single origin state. For instance, the number in row 2, column 0, which happens to be .059, is the probability that a perfectly templated pair of R8s will specify a new R8 in error position 2, as illustrated in Figure 45. Multiplying a vector of average state occupancy gives the expected average state occupancy of the next column, in an approximation involving rare errors in an otherwise well-patterned field.

Bibliography

1. Frankfort, B., & Mardon, G. (2002). R8 development in the Drosophila eye: a paradigm for neural selection and differentiation. *Development , 129* (6), 1295-1306.

2. Held, L. (2002). *Imaginal Discs.* Cambridge: Cambridge University Press.

3. Hsiung, F., & Moses, K. (2002). Retinal development in Drosophila: specifying the first neuron. *Human Molecular Genetics* , 11, (10) 1207-1214.

4. Koch, A., & Meinhardt, H. (1994). Biological pattern formation: from basic mechanisms to complex structures. *Reviews of Modern Physics , 66* (4), 1481-1507.

5. Voas, M., & Rebay, I. (2003). Signal integration during development: Insights from the Drosophila eye. *Developmental Dynamics , 229* (1), 162-175.

6. Lubensky, D., *personal communication*

7. Cubas, P., & Modolell, J. (1992) The Extramacrochaete gene provides information for sensory organ patterning. *EMBO Journal , 11* (9), 3385-3393.

8. Cubas, P., Decelis, J., Campuzano, S., & Modolell, J. (1991) Proneural clusters of achaete-scute expression and the generation of sensory organs in the Drosophila imaginal wing disk. *Genes & Development , 5* (6), 996-1008.

9. Culí, J., & Modolell, J. (1998). Proneural gene self-stimulation in neural precursors: an essential mechanism for sense organ development that is regulated by Notch signaling. *Genes & Development , 12* (13), 2036-47.

10. Culi, J., Martin-Blanco, E., & Modolell, J. (2001) The EGF receptor and N signalling pathways act antagonistically in Drosophila mesothorax bristle patterning. *Development , 128* (2), 299-308.

11. Jennings, B., Decelis, J., Delidakis, C., Preiss, A., & Bray, S. (1995) Role of Notch and acaete-scute complex in the expression of enhancer of split bHLH proteins. *Development , 121* (11), 3745-3752.

12. Schweisguth, F. (1995) Suppressor-of-Hairless is required for signal reception during lateral inhibition in the Drosophila pupal notum. *Development , 121* (6), 1875-1884.

13. Simpson, P. (1997). Notch signalling in development: on equivalence groups and asymmetric developmental potential. *Current Opinion in Genetics & Development , 7* (4), 537-542.

14. Zur Lage, P., Powell, L., Prentice, D., McLaughlin, P., & Jarman, A. (2004). EGF Receptor Signaling Triggers Recruitment of Drosophila Sense Organ Precursors by Stimulating Proneural Gene Autoregulation. *Developmental Cell , 7* (5), 687-696.

15. Dietrich, W. (1909). Die Facettenaugen der dipteren. *Zeitschrift Fur Wissenschaftliche Zoologie, 92*, (465).

16. Waddington, C., & Perry, M. (1960). The ultra-structure of the developing eye of Drosophila. *Proceedings of the Royal Society of London. Series B, Biological Sciences , 153* (951), 155-178.

17. Carthew, R. (2007). Pattern formation in the Drosophila eye. *Current Opinion in Genetics & Development , 17* (4), 309-313.

18. D. F. Ready, D., Hanson, T., & Benzer, S. Developmental Biology **53**, 217 (1976).

19. Jarman, A., Grell, E., Ackerman, L., Jan, L., & Jan, Y. (1994). atonal is the proneural gene for Drosophila photoreceptors. *Nature , 369* (6479), 398-400.

20. Jarman, A., Sun, Y., Jan, L., & Jan, Y. (1995). Role of the proneural gene, atonal, in formation of Drosophila chordotonal organs and photoreceptors. *Development , 121* (7), 2019-2030.

21. Tomlinson, A. (1988). Cellular interactions in the developing Drosophila eye. *Development , 104* (2), 183-193.

22. Morante, J., Desplan, C., & Celik, A. (2007). Generating patterned arrays of photoreceptors. *Current Opinion in Genetics & Development , 17* (4), 314-319.

23. Hayashi, T., & Carthew, R. (2004). Surface mechanics mediate pattern formation in the developing retina. *Nature , 431* (7009), 647-652.

24. Baker, N. E.(2007). Patterning signals and proliferation in Drosophila imaginal discs. *Current Opinion in Genetics & Development , 17* (4), 287-293.

25. Dartmouth Electron Microscope Facility, (2000).

26. Fu, W., & Baker, N. (2003). Deciphering synergistic and redundant roles of Hedgehog, Decapentaplegic and Delta that drive the wave of differentiation in Drosophila eye development. *Development , 130* (21), 5229-5239.

27. Kalderon, D. (2008). Hedgehog Signaling: A Smoothened Conformational Switch. *Current Biology , 18* (2), R64-R66.

28. Kumar, J., & Moses, K. (2001). The EGF receptor and notch signaling pathways control the initiation of the morphogenetic furrow during Drosophila eye development. *Development , 128* (14), 2689-2697.

29. Pappu, K., & Mardon, G. (2004). Genetic control of retinal specification and determination in Drosophila. *The International Journal of Developmental Biology , 48* (8-9), 913-924.

30. Rodrigues, A., Werner, E., & Moses, K. (2005). Genetic and biochemical analysis of the role of Egfr in the morphogenetic furrow of the developing Drosophila eye. *Development , 132* (21), 4697-4707.

31. Baker, N. (2006) *personal communication*.

32. Dokucu, M., Zipursky, S., & Cagan, R. (1996). Atonal, rough and the resolution of proneural clusters in the developing Drosophila retina. *Development , 122* (12), 4139-47.

33. Brown, N., Paddock, S., Sattler, C., Cronmiller, C., Thomas, B., & Carroll, S. (1996). Daughterless is Required for Drosophila Photoreceptor Cell Determination, Eye Morphogenesis, and Cell Cycle Progression. *Developmental Biology , 179* (1), 65-78.

34. Chen, K., & Chien, C. (1999). Negative regulation of atonal in proneural cluster formation of Drosophila R8 photoreceptors. *PNAS , 96* (9), 5055-5060.

35. Baonza, A., Casci, T., & Freeman, M. (2001). A primary role for the epidermal growth factor receptor in ommatidial spacing in the Drosophila eye. *Current Biology , 11* (6), 396-404.

36. Nelson, B., Hartman, B., Georgi, S., Lan, M., & Reh, T. Transient inactivation of Notch signaling synchronizes differentiation of neural progenitor cells. *Developmental Biology , 304* (2), 479-498.

37. Nakao, K., & CamposOrtega, J. (1996). Persistent expression of genes of the Enhancer of split complex suppresses neural development in Drosophila. *Neuron , 16* (2), 275-286.

38. Ilagan, M., & Kopan, R. (2007). SnapShot: Notch Signaling Pathway. *Cell , 128* (6), 1246.e1-1246.e2.

39. Lai, E. (2004). Notch signaling: control of cell communication and cell fate. *Development , 131* (5), 965-973.

40. de Joussineau, C., Soule, J., Martin, M., Anguille, C., Montcourrier, P., & Alexandre, D. (2003). Delta-promoted filopodia mediate long-range lateral inhibition in Drosophila. *Nature , 426* (6966), 555-559.

41. Chitnis, A. (1995). The role of Notch in lateral inhibition and cell fate specification. *Molecular and Cellular Neuroscience , 6*, 557-569.

42. Castro, B., Barolo, S., Bailey, A., & Posakony, J. (2005). Lateral inhibition in proneural clusters: cis-regulatory logic and default repression by Suppressor of Hairless. *Development , 132* (15), 3333-3344.

43. Bailey, A., & Posakony, J. (1995). Suppressor of Hairless directly activates transcription of Enhancer of split complex genes in response to Notch receptor activity. *Genes & Development , 9* (21), 2609-2622.

44. Mok, L., Qin, T., Bardot, B., LeComte, M., Homayouni, A., Ahimou, F., et al. (2005). Delta activity independent of its activity as a ligand of Notch. *BMC Developmental Biology , 5* (1), 6.

45. Baonza, A., & Freeman, M. (2001). Notch signalling and the initiation of neural development in the Drosophila eye. *Development , 128*, 3889-3898.

46. Baker, N., (2002) in *Drosophila Eye Development*, (Springer-Verlag Berlin, Berlin), Vol. 37, p. 35.

47. Baker, N., (1996) Evolution of proneural atonal expression during distinct regulatory phases in the developing Drosophila eye. *Current Biology , 6* (10), 1290-1302.

48. Doroquez, D., & Rebay, I. (2006). Signal integration during development: Mechanisms of EGFR and notch pathway function and cross-talk. *Critical Reviews in Biochemistry and Molecular Biology , 41* (6), 339-385.

49. Baker, N.E., Mlodzik, M., & Rubin, G. (1990). Spacing differentiation in the developing Drosophila eye: a fibrinogen-related lateral inhibitor encoded by scabrous. *Science , 250* (4986), 1370-1377.

50. Ellis, M., Weber, U., Wiersdorff, V., & Mlodzik, M. (1994). Confrontation on scabrous expressing and non-expressing cells is essential for normal ommatidial spacing in the Drosophila eye. *Development , 120* (7), 1959-1969.

51. Hu, X., Lee, E., & Baker, N. (1995). Molecular analysis of scabrous mutant alleles from Drosophila melanogaster indicates a secreted protein with two functional domains. *Genetics , 141* (2), 607-617.

52. Li, Y., Fetchko, M., Lai, Z., & Baker, N. (2003). Scabrous and Gp150 are endosomal proteins that regulate Notch activity. *Development , 130* (13), 2819-2827.

53. Liberman, M., Gao, J., He, D., Wu, X., Jia, S., & Zuo, J. (2002). Prestin is required for electromotility of the outer hair cell and for the cochlear amplifier. *Nature , 419* (6904), 300-304.

54. Powell, P., Wesley, C., Spencer, S., & Cagan, R. (2001). Scabrous complexes with Notch to mediate boundary formation. *Nature , 409* (6820), 626-630.

55. Rawlins, E., Lovegrove, B., & Jarman, A. (2003). Echinoid facilitates Notch pathway signalling during Drosophila neurogenesis through functional interaction with Delta. *Development , 130* (26), 6475-6484.

56. Rawlins, E., White, N., & Jarman, A. (2003). Echinoid limits R8 photoreceptor specification by inhibiting inappropriate EGF receptor signalling within R8 equivalence groups. *Development , 130* (16), 3715-3724.

57. Price, J., Savenye, E., Lum, D., & Breitkreutz, A. Dominant enhancers of Egfr in Drosophila melanogaster: Genetic links between the Notch and Egfr signaling pathways. *Genetics , 147* (3), 1139-1153.

58. Brown, K., Kerr, M., & Freeman, M. (2007). The EGFR ligands Spitz and Keren act cooperatively in the Drosophila eye. *Developmental Biology , 307* (1), 105-113.

59. Bornholdt, S. (2005). Systems biology: less is more in modeling large genetic networks. *Science's STKE , 310* (5747), 449.

60. Alon, U. (2006). *An Introduction to Systems Biology: Design Principles of Biological Circuits*. Chapman & Hall/CRC.

61. Cross, M., & Hohenberg, P. (1993). Pattern formation outside of equilibrium. *Reviews of Modern Physics , 65* (3), 851-1112.

62. Bray, S. (2006). Notch signalling: a simple pathway becomes complex. *Nature Reviews Molecular Cell Biology , 7* (9), 678-689.

63. Le Borgne, R., Remaud, S., Hamel, S., & Schweisguth, F. (2005). Two Distinct E3 Ubiquitin Ligases Have Complementary Functions in the Regulation of Delta and Serrate Signaling in Drosophila. *PLoS Biology , 3* (4), e96.

64. LeCourtois, M., & Schweissguth, F. (1995). The neurogenic Supressor of Hairless DNA-binding protein mediates the transcriptional activation of the Enhancer of split complex genes triggered by Notch signaling. *Genes & Development , 9* (21), 2598-2608.

65. Maier, D. (2006). Hairless: the ignored antagonist of the Notch signalling pathway. *Hereditas , 143* (2006), 212-221.

66. Ehebauer, M., Hayward, P., & Arias, A. (2006). Notch, a Universal Arbiter of Cell Fate Decisions. *Science , 314* (5804), 1414-1415.

67. Driever & Nusslein-Volhard. (1988). A gradient of bicoid protein in Drosophila embryos. *Cell , 54,* 83-93.

68. Driever & Nusslein-Volhard. (1988). The bicoid protein determines position in the Drosophila embryo in a concentration-dependent manner. *Cell , 54,* 95-104.

69. MacDonald & Struhl. (1988). Cis-acting sequences responsible for anterior localization of bicoid mRNA in Drosophila embryos. *Nature , 336*, 595-598.

70. Ephrussi, A., & Johnston, D. (2004). Seeing Is Believing The Bicoid Morphogen Gradient Matures. *Cell , 116* (2), 143-152.

71. Wolpert, L. (1969). Positional information and the spatial pattern of cellular differentiation. *Journal of Theoretical Biology , 25,* 1-47.

72. Aegerterwilmsen, T., Aegerter, C., & Bisseling, T. (2005). Model for the robust establishment of precise proportions in the early embryo. *Journal of Theoretical Biology , 234* (1), 13-19.

73. Bergmann, S., Tamari, Z., Schejter, E., B.Z., S., & Barkai, N. (2008). Re-examining the Stability of the Bicoid Morphogen Gradient. *Cell , 132* (1), 15-17.

74. Bintu, L., Buchler, N., Garcia, H., Gerland, U., Hwa, T., Kondev, J., et al. (2005). Transcriptional regulation by the numbers: applications. *Current Opinion in Genetics & Development , 15* (2), 125-135.

75. Eldar, A., Shilo, B., & Barkai, N. (2004). Elucidating mechanisms underlying robustness of morphogen gradients. *Current Opinion in Genetics & Development , 14* (4), 435-439.

76. He, F., Wen, Y., Deng, J., Lin, X., Lu, L., Jiao, R., et al. (2008). Probing intrinsic properties of a robust morphogen gradient in Drosophila. *Developmental Cell , 15* (4), 558-67.

77. Bollenbach, T., Kruse, K., Pantazis, P., González-Gaitán, M., & Jülicher, F. (2005). Robust Formation of Morphogen Gradients. *Physical Review Letters , 94* (1), 4.

78. Coppey, M., Berezhkovskii, A., Kim, Y., Boettiger, A., & Shvartsman, S. (2007). Modeling the bicoid gradient: Diffusion and reversible nuclear trapping of a stable protein. *Developmental Biology , 312* (2), 623-630.

79. Moussian, B., & Roth, S. (2005). Dorsoventral Axis Formation in the Embryo—Shaping and Transducing a Morphogen Gradient. *Current Biology , 15* (21), R887-R899.

80. Lander, A. (2007). Morpheus Unbound: Reimagining the Morphogen Gradient. *Cell , 128* (2), 245-256.

81. Yucel, G., & Small, S. (2006). Morphogens: Precise Outputs from a Variable Gradient. *Current Biology , 16* (1), R29-R31.

82. Ben-Zvi, D., Shilo, B.Z., Fainsod, A., & Barkai, N. (2008). Scaling of the BMP activation gradient in Xenopus embryos. *Nature , 453 (7199)*, 1205-1211.

83. McHale, P., Rappel, W.J., & Levine, H. (2006). Embryonic pattern scalingachieved by oppositely directed morphogen gradients. *Physical Biology , 3* , 107-120.

84. Mizutani, C., Nie, Q., Wan, F., Zhang, Y., Vilmos, P., Sousaneves, R., Bier, E., Marsh, J., & Lander, A. (2005). Formation of the BMP Gradient in the Embryo. *Developmental Cell , 8 (6)*, 915-924.

85. Turing, A., (1952) The chemical basis of morphogenesis, *Philosophical Transactions of The Royal Society of London, series B , 237,* 37–72.

86. Murray, J. (2002) *Mathematical Biology.* Springer, New York. Third Edition.

87. Harris, M., Williamson, S., Fallon, J., Meinhardt, H., & Prum, R. (2005). Molecular evidence for an activator-inhibitor mechanism in development of embryonic feather branching. *PNAS , 102* (33), 11734-11739.

88. Sick, S., Reinker, S., Timmer, J., & Schlake, T. (2006). WNT and DKK determine hair follicle spacing through a reaction-diffusion mechanism, *Science, 314*, 1447-1450.

89. Levine, H., Kessler, D.H., & Rappel, W.J. (2006). Directional sensing in eukaryotic chemotaxis: A balanced inactivation model. *PNAS , 103 (26)*, 9761-9766.

90. Meinhardt, H. (1999). Orientation of chemotactic cells and growth cones: models and mechanisms. *Journal of Cell Science , 112 (17)*, 2867-2874.

91. Rappel, W.J., & Levine, H. (2008). Receptor Noise and Directional Sensing in Eukaryotic Chemotaxis. *Physical Review Letters , 100 (22)*, 1-4.

92. Meir, E., Von Dassow, G., Munro, E., & Odell, G. (2002). Robustness, flexibility, and the role of lateral inhibition in the neurogenic network. *Current Biology , 12* (10), 778-786.

93. Collier, J., Monk, N., Maini, P., & Lewis, J. (1996). Pattern formation by lateral inhibition with feedback: A mathematical model of Delta-Notch intercellular signalling. *Journal of Theoretical Biology , 183* (4), 429-446.

94. Deblandre, G., Wettstein, D., Koyano-Nakagawa, N., & Kintner, C. (1999). A two-step mechanism generates the spacing pattern of the ciliated cells in the skin of Xenopus embryos. *Development , 126* (21), 4715-4728.

95. Owen, M., & Sherratt, J. (1998). Mathematical modelling of juxtacrine cell signalling. *Mathematical Biosciences , 153* (2), 125-150.

96. Rauch, E., & Millonas, M. (2004). The role of trans-membrane signal transduction in turing-type cellular pattern formation. *Journal of Theoretical Biology , 226* (4), 401-407.

97. Wearing, H., & Sherratt, J. (2001). Nonlinear analysis of juxtacrine patterns. *SIAM Journal on Applied Mathematics , 62* (1), 283-309.

98. Wearing, H., Owen, M., & Sherratt, J. (2000). Mathematical Modelling of Juxtacrine Patterning. *Bulletin of Mathematical Biology , 62* (2), 293-320.

99. Webb, S., & Owen, M. (2004). Intra-membrane ligand diffusion and cell shape modulate juxtacrine patterning. *Journal of Theoretical Biology , 230* (1), 99-117.

100. Webb, S., & Owen, M. (2004). Oscillations and patterns in spatially discrete models for developmental intercellular signalling. *Journal of Mathematical Biology , 48* (4), 444-476.

101. Monk, N.A.M. (1998). Restricted-range gradients and travelling fronts in a model of juxtacrine cell relay. *Bulletin of Mathematical Biology , 60 (5)*, 901-918.

102. Savage, N.S., Walker, T., Wieckowski, Y., Schiefelbein, J., Dolan, L., Monk, N.A.M., & Weigel, D. (2008). A Mutual Support Mechanism through Intercellular Movement of CAPRICE and GLABRA3 Can Pattern the Arabidopsis Root Epidermis. *Plos Biology , 6 (9)*, 1899-1909.

103. Kwak, S.H., & Schiefelbein, J. (2008). A Feedback Mechanism Controlling SCRAMBLED Receptor Accumulation and Cell-Type Pattern in Arabidopsis. *Current Biology , 18 (24)*, 1949-1954.

104. Gómez-Skarmeta, J., Campuzano, S., & Modolell, J. (2003). Half a century of neural prepatterning: the story of a few bristles and many genes. *Nature Reviews Neuroscience , 4* (7), 587-598.

105. Giudicelli, F., Özbudak, E., Wright, G., & Lewis, J. (2007). Setting the Tempo in Development: An Investigation of the Zebrafish Somite Clock Mechanism. *PLoS Biology , 5* (6), e150.

106. Goldbeter, A., & Pourquie, O. (2008). Modeling the segmentation clock as a network of coupled oscillations in the Notch, Wnt and FGF signaling pathways. *Journal of Theoretical Biology , 252* (3), 574-585.

107. Boissonade, J., & De Kepper, P. (1980). Transitions from bistability to limit cycle oscillations. Theoretical analysis and experimental evidence in an open chemical system. *J. Phys. Chem , 84* (5), 501-506.

108. Pourquié, O. (2003). The segmentation clock: converting embryonic time into spatial pattern. *Science , 301* (5631), 328-30.

109. Riedel-Kruse, I., Muller, C., & Oates, A. (2007). Synchrony dynamics during initiation, failure, and rescue of the segmentation clock. *Science , 317* (5846), 1911.

110. Reeves, G., Muratov, C., Schupbach, T., & Shvartsman, S. (2006). Quantitative Models of Developmental Pattern Formation. *Developmental Cell , 11 (3)*, 289-300.

111. Shvartsman, S., Muratov, C.B., & Lauffenburger, D.A. (2002). Modeling and computational analysis of EGF receptor-mediated cell communication in Drosophila oogenesis. *Development, 129 (11)*, 2577-2589.

112. Cherry, J., & Adler, F. (2000). How to make a Biological Switch. *Journal of Theoretical Biology , 203* (2), 117-133.

113. Fáth, G. (1998). Propagation failure of traveling waves in a discrete bistable medium. *Physica D: Nonlinear Phenomena , 116* (1-2), 176-190.

114. Hankerson, D., & Zinner, B. (1993). Wavefronts for a cooperative tridiagonal system of differential equations. *Journal of Dynamics and Differential Equations , 5* (2), 359-373.

115. Pribyl, M., Muratov, C., & Shvartsman, S. (2003). Discrete models of autocrine cell communication in epithelial layers. *Biophysical Journal , 84* (6), 3624-3635.

116. Muratov, C., & Shvartsman, S. (2004). Signal Propagation and Failure in Discrete Autocrine Relays. *Br. J. Cancer Phys Rev Lett , 93*, 118101.

117. Zinner, B. (1992). Existence of traveling wavefront solutions for the discrete Nagumo equation. *Journal of differential equations , 96* (1), 1-27.

118. Owen, M. (2002). Waves and propagation failure in discrete space models with nonlinear coupling and feedback. *Physica D: Nonlinear Phenomena , 173* (1-2), 59-76.

119. Jain, P., & Banerjee, S. (2003). Border collision bifurcations in one-dimensional discontinuous maps. *Int. J. Bifurc. Chaos , 13* (11), 3341–3352.

120. Fath, G., & Domanski, Z. (1999). Avalanche of bifurcations and hysteresis in a model of cellular differentiation. *Physical Review E , 60* (4), 4604-4609.

121. Elmer, C., & Van Vleck, E. (1999). Analysis and computation of travelling wave solutions of bistable differential-difference equations. *Nonlinearity , 12*, 771-798.

122. Plahte, E., & Oyehaug, L. (2007). Pattern-generating travelling waves in a discrete multicellular system with lateral inhibition. *Physica D: Nonlinear Phenomena , 226* (2), 117-128.

123. Acar, M., Jafar-Nejad, H., Giagtzoglou, N., Yallampalli, S., David, G., He, Y., et al. (2006). Senseless physically interacts with proneural proteins and functions as a transcriptional co-activator. *Development , 133* (10), 1979-1989.

124. Jafar-Nejad, H., Acar, M., Nolo, R., Lacin, H., Pan, H., Parkhurst, S., et al. (2003). Senseless acts as a binary switch during sensory organ precursor selection. *Genes & Development , 17* (23), 2966-2978.

125. Jafar-Nejad, H., Tien, A., Acar, M., & Bellen, H. Senseless and Daughterless confer neuronal identity to epithelial cells in the Drosophila wing margin. *Development , 133* (9), 1683-1692.

126. Nolo, R., Abbott, L., & Bellen, H. (2000). Senseless, a Zn finger transcription factor, is necessary and sufficient for sensory organ development in Drosophila. *Cell , 102* (3), 349-62.

127. Pepple, K., Atkins, M., Venken, K., Wellnitz, K., Harding, M., Frankfort, B., et al. (2008). Two-step selection of a single R8 photoreceptor: a bistable loop between senseless and rough locks in R8 fate. *Development , 135* (24), 4071-9.

128. Hsu, C.-P., C.W., L., C.W., C., & Lee, C. (2006). Constructing quantitative models from qualitative mutant phenotypes: preferences in selecting sensory organ precursors. *Bioinformatics , 22* (11), 1375-1382.

129. Ingolia, N. (2004). Topology and Robustness in the Drosophila Segment Polarity Network. *PLoS Biology , 2* (6), e123.

130. Kashtan, N., & Alon, U. (2005). Spontaneous evolution of modularity and network motifs. *PNAS , 102* (39), 13773-13778.

131. Giagtzoglou, N., Alifragis, P., Koumbanakis, K., & Delidakis, C. (2003). Two modes of recruitment of E (spl) repressors onto target genes. *Development , 130* (2), 259-270.

132. Gill, A., (1962). *Introduction to the Theory of Finite-state Machines*. McGraw-Hill.

133. Greenspan, R., (2004). *Fly Pushing*. Cold-Spring Harbor Laboratory Press.

134. Tanase-Nicola, S., (2007). *Personal communication*.